ANALYSIS OF ASTM A416 TENDON STEEL CORROSION IN ALKALINE
SIMULATED PORE SOLUTIONS

By

YU-MIN CHEN

A DISSERTATION PRESENTED TO THE GRADUATE SCHOOL
OF THE UNIVERSITY OF FLORIDA IN PARTIAL FULFILLMENT
OF THE REQUIREMENTS FOR THE DEGREE OF
DOCTOR OF PHILOSOPHY

UNIVERSITY OF FLORIDA

2016

To my dear family members and my group members

ACKNOWLEDGMENTS

TABLE OF CONTENTS

LIST OF TABLES

LIST OF FIGURES

Abstract of Dissertation Presented to the Graduate School
of the University of Florida in Partial Fulfillment of the
Requirements for the Degree of Doctor of Philosophy

ANALYSIS OF ASTM A416 TENDON STEEL CORROSION IN ALKALINE
SIMULATED PORE SOLUTIONS

By

Yu-Min Chen

August 2016

Chair: Mark E. Orazem
Major: Chemical Engineering

The corrosion behavior of ASTM A416 steel in alkaline simulated pore solution under active aeration was studied by cyclic voltammetry, electrochemical impedance spectroscopy, and measurement of open-circuit potential and polarization curves. Scanning electron microscopy (SEM), X-ray photonelectron spectroscopy (XPS), high-resolution cross-sectional transmission electron microscopy (HR-XTEM) and high-angle annular dark-field scanning transmission electron microscopy (HAADS-TEM) were used to study the oxide film's composition and thickness. Preliminary experiments were conducted to investigate the influence of chloride ions and dissolved oxygen on corrosion of steel in simulated pore solution. The impedance measurements at open-circuit potential did not show a significant difference between ASTM A416 steel immersed in a solution of 40g/L NaCl and a chloride-free solution. A significant difference was also not found between ASTM A416 steel immersed in aerated and deaerated solutions, suggesting the cause for the corrosion of ASTM A416 steel in concrete can be attributed to other factors. The open-circuit potential of ASTM A416 required about 300 ks (85 h) to reach steady-state. At other potentials, the steady–state current was generally obtained after 50ks. At +0.22 V(Hg/HgO), an elapsed time of 250 ks was required to reach the steady-state.

Since the impedance data could become corrupted by various errors, the measurement model analysis was applied to determine the portion of the frequency range that could be used for subsequent regression. The fitting strategies employed in this present dissertation

were downhill simplex and Levenberg-Marquardt methods. Before steady-state was reached, the electrochemical impedance spectra were interpreted by use of a model that accounted for porous electrode behavior and for the contributions of both anodic and cathodic reactions. After steady-state was reached, two different electrochemical impedance responses could be observed: one still shows porous electrode behavior and another showed non-porous electrode behavior. The open–circuit corrosion rate for a stationary working electrode immersed in the actively-aerated electrolyte was 64 μm/ year shortly after the cathodic pre-treatment was completed, but it was too small to be detected after steady-state was reached.

The low-magnification SEM images for corroded and passive ASTM A416 steel in Sika Grout 300PT suggested that corroded ASTM A416 steel has a rougher surface than passive steel, and that the size of corrosion products is varied, but generally within 1 to 20μm. The XPS spectra for ASTM A416 steel after 8 cycles of cyclic voltammetry scanning suggested that calcium plays a role in oxide film composition, which may be attributed to the deposition of $Ca(OH)_2$ from the cathodic reaction. The images from HR-XTEM cannot provide clear information about the oxide film thickness; however, HAADF-STEM showed the oxide film thickness for steel in simulated pore solution at open-circuit potential was about 3-7nm. The essential parameter to estimate oxide film thickness, ρ_δ, is about 10000 Ωcm. The oxide film thickness increased over time. The variation of film thickness with applied potential could be attributed to the greater immersion time required to perform steady-state measurements at the applied potential.

The corrosion of ASTM A416 steel in simulated pore solution could only be observed before steady-state was reached and when positive potentials were applied. Chloride ion contamination and the lack of dissolved oxygen in the simulated pore solution were not the main factors contributing towards corrosion. The chemical composition and oxide film thickness, as observed from surface analysis, were not consistent for all ASTM A416 steels.

CHAPTER 1
INTRODUCTION

Within the highly alkaline (pH > 13) environment provided by concrete, carbon steel rebar is protected from corrosion by a passive iron oxide film. The Pourbaix diagram(4) suggests that the iron may remain passive over a wide range of potentials, and even a very limited supply of oxygen is enough to prevent corrosion. Moreover, concrete can also provide a diffusion barrier between steel and the external environment, limiting the access of substances that may cause corrosion.

The presence of corrosion has been attributed to the loss of protection by carbonation and by chloride. The concentration of chloride ions has a large impact on the corrosion of steel in concrete; therefore, the concept of a chloride threshold level (CTL) was proposed. The CTL can be defined as the chloride content at the steel depth that is necessary to sustain local passive film breakdown and hence initiate the corrosion process. It is usually presented as the ratio of chloride to hydroxyl ions. The carbonation process can be attributed to the diffusion of carbon dioxide (CO_2) from the atmosphere into capillary pores, and as it combines with water to form carbonic acid, the local pH value in the concrete decreases.

Other factors that may contribute to the corrosion of steel in concrete are temperature and dissolved oxygen content. The effect of temperature on steel corrosion in concrete can be quite complicated due to the variation of kinetic parameters of corrosion with temperature (e.g. Tafel slopes, exchange current densities and equilibrium potentials) and also due to the changes in the properties of the concrete/pore solution. From the Pourbaix diagram, the passivity of iron in pH 14 solution is provided by oxide films of Fe_3O_4 or Fe_2O_3. Nevertheless, in anaerobic solution the protective oxide film could turn into complex anion, $HFeO_2^-$, resulting in a loss of passivity.

Nevertheless, the corrosion of steel in concrete may still occur, even in the absence of the above factors. In this dissertation, the corrosion behavior of ASTM A416 steel

was analyzed by electrochemical approaches and surface analysis. The electrochemical approaches include open-circuit potential measurement, linear sweep voltammetry, polarization curve, cyclic voltammetry and electrochemical impedance spectroscopy. The surface analyze includes scanning electron microscope (SEM), x-ray photoelectron microscope (XPS), high-resolution cross-section transmission electron microscope (HR-XTEM) and high-angle annular dark field scanning transmission electron microscopy (HAADF-STEM). The corrosion rate and oxide film thickness can be estimated from the fitting parameters of a process model. The oxide film thickness as measured by HAADF-STEM was used to in combination with the power-law model to find a value for the oxide film resistivity at the oxide-electrolyte interface.

A comprehensive literature review for the corrosion of steel in concrete and in simulated pore solution is presented in Chapter 2. The experimental setup to analyze the corrosion behavior of ASTM A416 steel is presented in Chapter 3. In Chapter 4, the corrosion behavior of steel was analyzed by open-circuit potential measurement, polarization curve, linear sweep voltammetry, cyclic voltammetry, and electrochemical impedance spectroscopy. The theory and necessary information for impedance analysis, including the measurement model and constant-phase elements, are presented in Chapter 5. The corrosion behavior of ASTM A416 steel was further analyzed by SEM, XPS, HR-XTEM, and HAADF-STEM and the results are presented in Chapter 7. The discussion in Chapter 8 is based on the results from Chapter 5 and 7 and the conclusion is presented in Chapter 9.

CHAPTER 2
LITERATURE REVIEW

During the past few decades, segmentally constructed bridges incorporating post-tensioned tendons have been widely adopted for bridge construction because, as compared to other building techniques that involve assembly of larger sections, they can withstand heavier loads and allow for longer spans.(5) Post–tensioned tendons are made with high-strength steel strands placed within a high-density polyethylene duct, and the annulus is filled with a cementitious grout intended to maintain an alkaline environment thereby inhibiting corrosion. However, corrosion of the steel tendons has become a significant problem, leading to premature structural failure. The first recorded failure attributed to the corrosion of post–tensioned steel occurred in 1980, when the southern outer roof of the Berlin Congress Hall collapsed only 23 years after it was constructed.(6) in 1999, the failure of a post–tensioned tendon of the Niles Channel Bridge in the Florida Keys (7) did not lead to the collapse of the structure, but it raised concerns over the integrity of the remaining tendons. Similar issues were reported at Mid Bay Bridge in the Western Florida Panhandle in 2001.(8) Successful implementation of post–tensioned segmental bridge construction requires both a better understanding of related corrosion mechanisms and a non-destructive means for the detection of conditions that may lead to failure.

Corrosion of steel strands within the tendons has been attributed to defective grout, including formation of voids by bleed water accumulation and re-absorption as well as areas of un-hydrated grout which has been termed deficient.(9) Recent examinations of failed tendons suggested that deficient grout has high moisture content, a high pore solution pH, a low chloride concentration, and a high sulfate concentration.(10) Bertolini and Carsana suggested that the corrosion of post-tensioned steel in deficient grout is initiated in high-alkaline environments by the large cathodic polarization that may exist in oxygen-deficient environments.(11) Hope et al. (12) suggested that the penetration of

moisture and chlorides to a localized area may form an aggressive environment resulting in corrosion. The significance of chloride ions in the corrosion of steel in concrete has led to the concept of a chloride threshold level (CTL), which can be expressed as the content of chloride at the steel depth that is necessary to sustain local passive film breakdown and hence initiate the corrosion process. Chloride threshold level is usually presented as the ratio of chloride to hydroxyl ions, the free chloride content or the percentage of the total chloride content relative to the weight of cement. Another factor that causes corrosion is the loss of protection by carbonation, which occurs in concrete because the precipitate $Ca(OH)_2$ are attacked by carbon dioxide from the air and converts to calcium carbonate. In CO_2-rich urban environments, the carbonation of concrete is the main mechanism leading to steel corrosion. The kinetics of carbonation for various kinds of concretes in different environments have been widely investigated. The relationship between carbonation thickness (x) and the exposure time (t) can be described in parabolic form as

$$\frac{\mathrm{d}x}{\mathrm{d}t} = kt^{-1/2} \tag{2–1}$$

where k is the proportionality constant that depends on several variables related to the quality of concrete as well as the environment. Corrosion is initiated in the form of pitting where the local pH falls below 10. The drop in pH releases at least 90% of the total surrounding chloride ions to participate in the corrosion process.([13](); [14]())

The environment of tendon steel in concrete can be mimicked by immersing steel in simulated pore solution. Several different simulated pore solutions have been used by scientists. Moreno et al.([15]()) tested the corrosion behavior of carbon steel rods in 0.9M NaOH, saturated $Ca(OH)_2$, 0.3M $NaHCO_3$+0.1M Na_2CO_3, and 0.015M $NaHCO_3$+0.005M Na_2CO_3 with varied concentrations of NaCl by polarization resistance and open–circuit potential measurement. Their results showed the corrosion current density increased with NaCl concentration and under weak carbonation conditions carbon steel did not passivate while in the presence of high levels of carbonate and the resistance to localized

corrosion was improved. Page and Vennesland[16] used titration, gravimetric analysis, and atomic absorption spectroscopy to analyze the composition of the pore solution in Portland cement. Their work suggested that the major species of pore solution are Na^+, K^+ and OH^-; whereas, Ca^{2+} and SO_4^{2-} are minor specimens. Page and Treadaway[17] also suggested that the solution inside Portland cement, which in contact with the hydrating cement grains contains hydroxides and sulfates of calcium, sodium and potassium, but noted that sulfate ions were rapidly precipitated to form the highly insoluble calcium sulfo-aluminate hydrate. Therefore, the pore solution consists largely of sodium, potassium, and hydroxide ions, and, as pH increases, the concentration of calcium ions conforms to the solubility product of calcium hydroxide.

The corrosion of post–tensioned steel may be related to the corrosion of steel reinforcement in concrete, which has been more extensively studied. Due to the natural chemistry of concrete, the pore solution has a high degree of alkalinity. In this environment, steel reinforcement is chemically protected by a passive film and exhibits high corrosion resistance.

Other research has focused on the properties of the passive film itself. Gouda performed galvanostatic polarization experiments for reinforcing steel in alkaline electrolytes.[18] This work suggested that, in aerated solutions, Fe_3O_4 was the intermediate oxidation product deposited on the steel surface; whereas, in deaerated solutions, ferrous hydroxide was the intermediate product. Zakroczymski et al. [19] simultaneously conducted electrochemical and ellipsometric studies of the anodic film growth on iron in 0.05M NaOH. Their work suggested that passivation occurs in two stages: in the first stage, which lasts for about 2s, the anodic current is consumed only for film growth, whereas in the second stage (t > 2s) the release of iron cations into the electrolyte also occurs. Moreover, the oxide film thickness is about 2 to 5 nm for the applied potential from -0.35 V(NHE) to 0.55 V(NHE). In recent studies[20; 21], it was shown that the passive films' oxidation state of iron on carbon steel in alkaline environments varied across

its film thickness: the inner oxide film that was adjacent to the steel substrate was a protective Fe^{2+} rich layer, while the outer layer was mainly composed of unprotective Fe^{3+} rich oxides and hydroxides. Sánchez-Moreno et al. [22] also suggested that a two-layered passive film forms on reinforced steel, consisting of an inner layer of a mixed iron oxide such as Fe_3O_4 and a Fe^{3+} outer layer. Geana et al. used cyclic voltammetry for iron in alkaline sulphate solutions to identify potential oxide film products. [23]; however, The results were influenced by the initial potential used in the cyclic voltammetry and by electrode pretreatment. Joriet et al. [24] used impedance spectroscopy, ring-disk electrode, electrochemical quartz crystal microbalance, and *in situ* Raman spectroscopy measurements on iron in NaOH solutions to associate specific peaks of cyclic voltammetry curves to formation of surface films. They reported that the passive film can be oxidized and reduced depending on the electrode potential. The results from Montemor et al. based on Auger electron spectroscopy suggested that the film thickness on steel was about 100 nm.[25] However, Ghods et al. [26; 20] used XPS to show that the thickness of passive films formed on carbon steel in simulated concrete pore solutions was about 5 nm. Their work also suggested that the concentration of $Fe_2O_3/FeOOH$ decreased toward the film-substrate interface, whereas, the concentration of Fe_3O_4/FeO increased; This difference between oxide film thickness estimation could be attributed to different element peaks. Ghods et al. [26; 20] used intensities of the total iron oxide for film thickness estimation while Montemor et al. [25] used Auger electron spectroscopy of oxygen. This discrepancy suggested that XPS might not be the optimal method for oxide film thickness estimation. Gunay et al. [27] used ADF-STEM and electron energy loss spectroscopy (EELS) to investigate the oxide film formed on carbon steel in saturated $Ca(OH)_2$ solution and in the simulated pore solution containing $Ca(OH)_2$, NaOH, KOH, and $CaSO_4$. Their ADF-STEM results suggested that the oxide film thickness was about 10 nm and the outer layer of the oxide film resembled Fe_3O_4 in the saturated $Ca(OH)_2$ solution and α-Fe_2O_3/Fe_3O_4 in the simulated pore solution. The composition of intermediate layer

consisted of Fe_3O_4, and the inner layer composition was FeO, which was unstable when exposed to chloride ions.

Electrochemical impedance spectroscopy (EIS) provides another approach to estimate oxide film thickness. Hirschorn et al. (28; 29) proposed a power-law model to estimate oxide film thickness from CPE parameters. Electrochemical impedance spectroscopy is also widely used to model and estimate corrosion rates from the anodic reaction resistance, $R_{t,a}$, extracted from a fitting procedure. Sánchez et al.(30) suggested that an equivalent circuit with two RC loops connected in parallel could be used to model the spontaneous growth of a passive layer. However, a Warburg element must be added in series with charge transfer resistance in the circuit when the passive layer was formed under anodic polarization.(30) Flis et al.(31) reported that, in Nyquist format, the low–frequency impedance presented an angle between 25 and 70 degrees with respect to the real axis, depending on immersion time and the charge transfer resistance. They suggested that the higher slope corresponded to better protective properties of the surface film. Dhouibi et al.(32) conducted impedance measurements to determine the long-term effectiveness of two corrosion inhibitors, calcium nitrate and alkanolamine, for carbon steel in concrete. Their impedance results showed that the steel–concrete interface response contained two or three loops. The resistance corresponding to the polarization resistance of the steel decreased with time in chloride solution, suggesting that the inhibitors did not prevent the corrosion process in the presence of chloride is present. Pech-Canul and Castro(33) conducted impedance measurements for carbon steel in concrete with a different water-cement ratio exposed to a tropical marine atmosphere. Their work suggested that a Randles circuit modified with a constant-phase element could be used to fit impedance data.

Temperature and dissolved oxygen content are other factors that may cause the corrosion of steel in concrete. Pour-Ghaz et al. (34; 35) tested the effect of temperature on the corrosion rate of steel corrosion in concrete by embedding steel rebar in mortar, and by simulated polarization resistance experiments. This method is based on the

numerical solution of the Laplaces equation, with pre-defined boundary conditions of the problem, and has been designed to establish independent correlations among corrosion rate, temperature, kinetic parameters, concrete resistivity and limiting current density for a wide range of possible anode/cathode (A/C) distributions on the reinforcement. Both results suggested that the corrosion rate of steel increased with temperature. The Pourbaix diagram can explain the influence of dissolved oxygen content; the passivity of iron in pH 14 solution is provided by oxide films of Fe_3O_4 or Fe_2O_3. Nevertheless, in anaerobic solution the protective oxide film could turn into complex anion, $HFeO_2^-$, lossing its passivity. Moreover, the main composition of oxide film in anaerobic conditions is $Fe(OH)_2$ and may undergo the Schikorr reaction to produce Fe_3O_4 at temperatures greater than 50°C.(36)

The purpose of this dissertation is to propose versatile physical models for the estimation of corrosion rate and oxide film thickness. In order to validate the accuracy and reliability of physical models, several different surface analysis techniques, SEM, XPS, HR-XTEM and HAADF-STEM were applied to analyze the oxide film composition and thickness in simulated pore solutions.

CHAPTER 3
EXPERIMENTAL SETUP

The chemical composition of simulated pore solution and the nominal composition of the ASTM A416 steel are presented in this chapter. The electrochemical behavior of ASTM A416 steel was studied by a traditional three-electrode-cell setup.

3.1 Materials

In order to simulate the environmental conditions for steel strands within cement grout, synthetic pore solutions were used following the recipe presented by Li and Sagüès(1) and shown in Table 3-1. The electrolyte was prepared with regent grade chemicals and deionized (14 MΩ) water. The mixture was stirred for a period of one hour and suspended $Ca(OH)_2$ solids were removed from the electrolyte by filtration (Whatman Grade 1 Filter Paper).

The counterelectrode consisted of a platinum sheet (5 mm × 50 mm). The reference electrodes employed were mercury/mercuric oxide (1 M KOH) and saturated calomel electrode (SCE). The working electrode was a 5 mm diameter, ASTM A416 steel rod embedded in epoxy resin to expose the circular face of the rod. The nominal composition of the ASTM A416 steel is presented in Table 3-2. Although based on Table 3-2 the quality of ASTM A416 steel may be assumed to be uniformed, a variation of steel quality was found by several different approaches. The cyclic voltammetry shown in Figure 4-5 suggests that different peaks, corresponding to different chemical composition of oxide film, can be observed. The XPS spectra, shown in Figure 7-5(A) and (B), suggests that Si can be detected from one steel but cannot be detected from another one. For the present work, the ASTM A416 steel for which Si was detected is named as No.1 ASTM A416 steel; whereas, the steel for which Si was not detected is named as No.2 ASTM A416 steel in

Table 3-1. Recipe for the simulated pore solution taken from Li and Sagüès,(1) and the resulting pH value.

$Ca(OH)_2$	NaOH	KOH	pH
2 (g/L)	8.33 (g/L)	23.3 (g/L)	13.8

Table 3-2. Chemical composition of ASTM A416 Steel.(2)

Element	C	Si	Mn	P	Cu	S	Fe
weight %	0.75-0.81	0.26-0.28	0.62-0.84	0.012-0.021	0.01-0.02	0.018-0.028	Remainder

this dissertation. No.1 and No.2 ASTM A416 steel are labeled as (1) and (2) in all the figures, respectively.

3.2   Instrumentation

All electrochemical measurements were performed with a Gamry Reference 600 potentiostat. The electrolyte temperature was controlled at 298±1 K by a VWR Scientific Model 1160 temperature controller. The rotating disk electrode experiments employed an Autolab RDE 80566 rotator and a MCUR70525 rotator motor controller from Metrohm USA.

3.3   Protocol

The working electrode was polished sequentially with #120, #320 and #600 grit silicon carbide papers to yield a smooth working electrode surface. As preliminary work showed that use of a high polish yielded irreproducible results, the polishing procedure followed that recommended by Asma et al.(37), who suggested that too fine or rough a polish should be avoided as it may induce high inaccuracy in predicting corrosion behavior. In the present work, reproducible results were not obtained for electrodes polished to a mirror finish (1 μm alumina powder). The working electrode was subsequently degreased with ethanol and washed with water before each experiment. Experiments were performed with a stationary electrode. After a sufficiently steady condition was achieved, impedance measurements were taken with frequencies ranging from 500 Hz to 0.05 Hz and with a perturbation amplitude of 5 mV. Prior to each measurement, the electrode was conditioned for one hour at -1.1 V(Hg/HgO) to remove any oxide film that may have formed on the specimen surface. After the conditioning step, the working electrode was kept at the corrosion potential for two hours before next measurement. Experiments were performed under passive aeration and under active

aeration by sparging ultra-zero grade air (combined total of CO and CO_2 less than 0.1 ppm) purchased from Airgas. A calibration experiment was performed by measured dissolved oxygen content as function of time with a Hach Orbisphere 3650 micrologger to ensure it was maintained at 8 ± 0.5 ppm.

CHAPTER 4
ELECTROCHEMICAL APPROACH

The electrochemical approaches used in this chapter to investigate the corrosion behavior of ASTM A416 steel includes open-circuit potential measurement, polarization curve, linear sweep voltammetry, cyclic voltammetry, pitting potential measurement, and electrochemical impedance spectroscopy.

4.1 Preliminary Experiments

Aggressive Cl^- ions were added to simulated pore solution to test their influence on the corrosion behavior of an ASTM A416 steel. The chloride threshold level, defined by the ratio of $[Cl^-]$:$[OH^-]$, as the content of chloride at the steel depth that is necessary to sustain local passive film breakdown and hence initiate the corrosion process. The pitting and repassivation behaviors can be observed from cyclic voltammetry, which is shown in Figure 4-6. The simulated pore solution contained 40g/L NaCl with a pH of 13.8; in a solution with these values, the chloride threshold level for ASTM A416 steel is about 1. However, the impedance measurements at open-circuit potential did not show significant difference between ASTM A416 steel immersed in a 40g/L NaCl added solution, and a chloride free solution. Corrosion initiated as pitting can happen when both chloride threshold level and pitting potential are reached.(1)

The effect of dissolved oxygen content has also been studied by sparging BIP grade nitrogen gas (Airgas) to deaerate the system. The impedance results from ASTM A416 steel in aerobic and anaerobic simulated pore solution still did not show a significant difference. The reasons causing corrosion of ASTM A416 steel in concrete shall be attributed to other factors. The impedance measurements to study how chloride and dissolved oxygen content effected thecorrosion of ASTM A416 steel are presented in 4.5.2.1.

4.2   Open-Circuit Potential

Open-circuit potential is also called corrosion potential. At open-circuit potential, the anodic reaction current is balanced by a cathodic reaction current. Therefore, the net current of system is zero. The anodic reaction for steel can be represented as

$$\text{Fe} \rightarrow \text{Fe}^{2+} + 2\text{e}^- \qquad (4\text{--}1)$$

and the cathodic reaction is the reduction of O_2 according to

$$\text{O}_2 + 2\text{H}_2\text{O} + 4\text{e}^- \rightarrow 4\text{OH}^- \qquad (4\text{--}2)$$

The change of open-circuit potential can be attributed to several different factors, including oxygen concentration, solution velocity, and temperature. These effects can be explained by the limiting diffusion current in the equation

$$i_\text{L} = \frac{n\text{FDc}}{\delta} \qquad (4\text{--}3)$$

where n is number of electrons transferred, F is the Faraday constant, D is the diffusivity, c is the concentration of the diffusing species, and δ is the thickness of the diffusion layer. Change in the concentration of dissolved oxygen and the thickness of the diffusion layer will cause a change of limiting diffusion current, resulting in the change of open-circuit potential.

The open-circuit potential of ASTM A416 steel in simulated pore solution as a function of time is shown in Figure 4-1.   The potential in these experiments was referred to a mercury/mercuric oxide electrode, which is reversible to hydroxide ions and therefore, does not offer the potential for contamination by chloride ions. After cathodic pre-treatment at -1.1 V(Hg/HgO), the open-circuit potential gradually reached a steady value of -80 mV(Hg/HgO) after 300 ks (85 h).

The increase in open-circuit potential can be attributed to the decrease of anodic reaction current, under the assumption that the oxygen reduction rate remained the same.
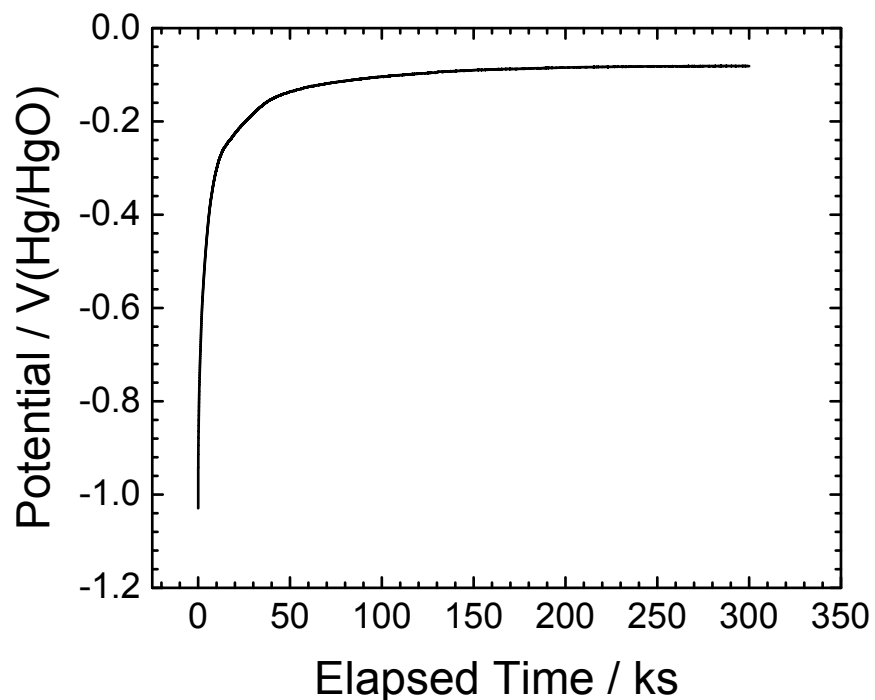
Figure 4-1. Open-circuit potential for the ASTM A416 electrode as a function of time.

The decrease in anodic reaction current can also be inferred as the increased passivity of the steel.

4.3 Polarization Curve and Linear Sweep Voltammetry

The polarization curve was found to be a strong function of sweep rate as well as different steel strands, as shown in Figure 4-2. The definition of No.1 and No.2 steel is described in Chapter 3. For No.1 steel, the current measured with a sweep rate of 1 mV/s was about 3 times larger than the current measured with a sweep rate of 0.1 mV/s and more than 10 times larger than the steady-state results. The steady-state current of No.1 steel was found to be about 100 times larger than the steady-state current of No.2 steel, suggesting that the corrosion resistivity of ASTM A416 steel is varied. The steady-state polarization curve was found by setting the desired potential and measuring the resulting current until a steady value was achieved. The anodic steady-state current suggested that ASTM A416 steel has passive behavior, while the cathodic steady-state current

27
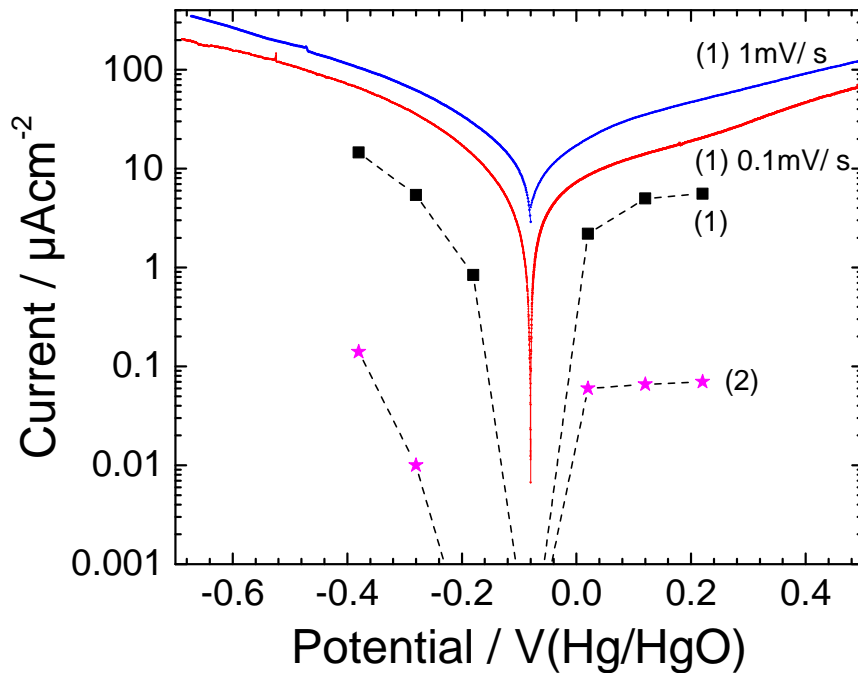
Figure 4-2. Steady-state polarization curve and results of linear sweep voltammetry with scan rates of 0.1 mV/s and 1 mV/s for ASTM A416 steel.

increased as the potential was decreased. Examples for measured values of current density are presented in Figure 4-3 as functions of elapsed time for applied potentials ranging from -0.38 V(Hg/HgO) to +0.22 V(Hg/HgO). The reason current for No.2 steel at -0.18 V(Hg/HgO) is not shown in Figure 4-2 is that it was too small to be measured correctly. The time required to reach steady-state was found to depend on potential. For an applied potential of -0.18 V(Hg/HgO), 50ks were required to reach steady-state; whereas, for +0.22 V(Hg/HgO), 250ks was required. The results of these measurements are presented as symbols in Figure 4-2.

4.4   Cyclic Voltammogram

The polarization behavior of the steel was explored using cyclic voltammetry. To maintain consistency with the experimental work of Joiret et al.(24) for a similar steel and environment, potentials were referred to a saturated calomel electrode (SCE).The 3rd
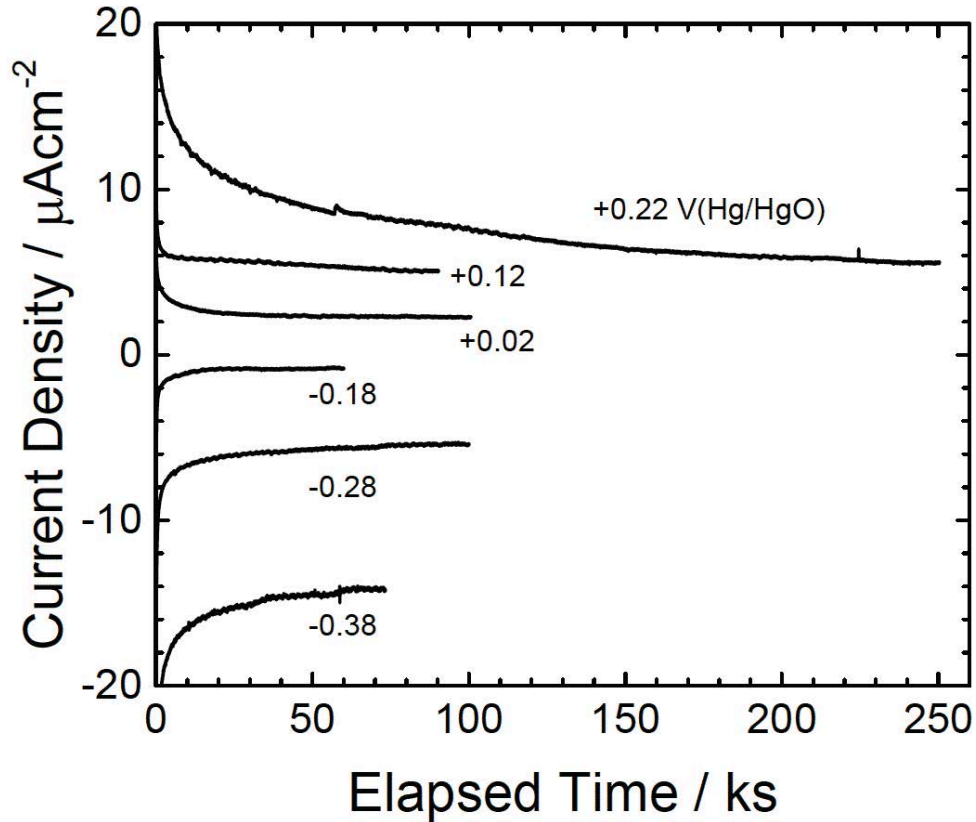
Figure 4-3. Current density for No.1 ASTM A416 as a function of time with applied potential as a parameter.

and 8th cycles obtained for a stationary No.1 ASTM A416 steel at a sweep rate of 10mV/s (dE/dt) are presented in Figure 4-4. The electrolyte was the simulated pore solution presented in Table 3-1 and taken from Li and Sagüès.(1).

The region of Fe electrochemical activity ranged from -1.3 to -0.2 V(SCE). The passivity domain varied from -0.2 to 0.5 V(SCE), where oxygen evolution was observed. Cyclic voltammograms were also obtained at a sweep rate of 50 mV/s. The location of the peaks was not influenced by sweep rate.

The results obtained in the present work are in good agreement with those presented by Joiret et al.(24) The cyclic voltammetry results reported by Geana et al,(23) and by Foulkes and McGrath(38) also showed similar peaks. Based on the comparison to their work, the peak A from the scan in the anodic direction, shown in Figure 4-4 may be
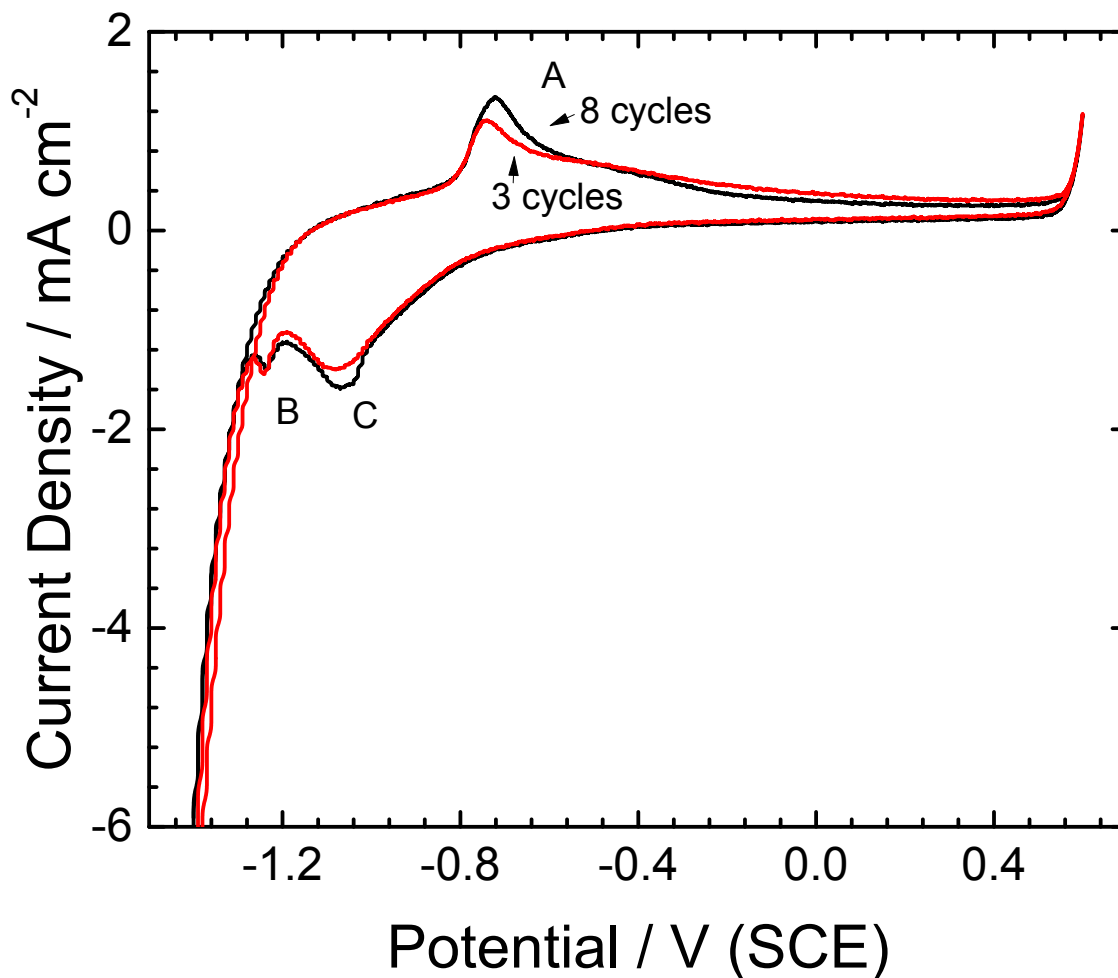
Figure 4-4. Results of the 3rd and 8th cyclic voltammograms for ASTM A416 steel in the simulated pore solution with a scan rate of 10 mV/s.

assigned to the formation of Fe_3O_4 according to the equation

$$3Fe(OH)_2 + 2OH^- \leftrightarrows Fe_3O_4 + 4H_2O + 2e^- \tag{4–4}$$

and

$$3FeO + 2OH^- \leftrightarrows Fe_3O_4 + H_2O + 2e^- \tag{4–5}$$
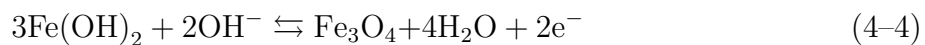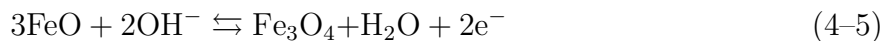
Peaks B and C from the scan in the cathodic direction may be assigned to the formation of $Fe(OH)_2$ and FeO, respectively, i.e.,

$$Fe + 3H_2O \leftrightarrows FeO + 2H_3O^+ + 2e^- \tag{4–6}$$
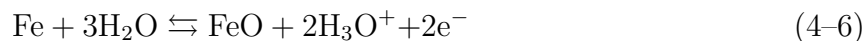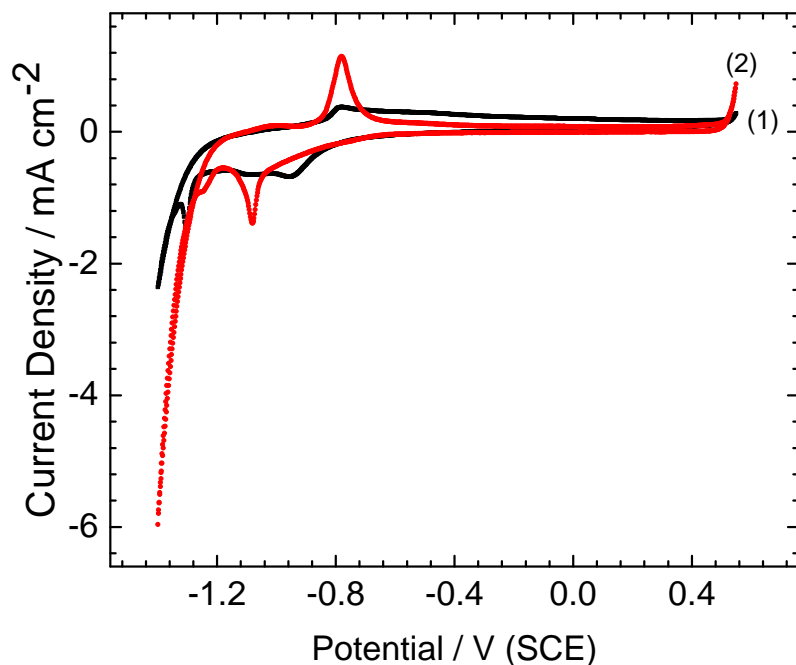
Figure 4-5. Results of the 8th cyclic voltammograms for different batch of ASTM A416 steel in the simulated pore solution with a scan rate of 10 mV/s.

and

$$Fe + 4H_2O \leftrightarrows Fe(OH)_2 + 2H_3O^+ + 2e^-$$ (4–7)
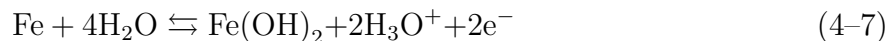
While the ASTM A416 steel in the present study contained a small amount of Mn, no redox peaks could be directly attributed to Mn activity. Freire et al.(39) suggested that the absence of Mn peaks can be explained by the high solubility of Mn oxo-hydroxides in highly alkaline solutions, resulting in low concentrations of soluble Mn species at the electrode surface.

However, different peaks can be observed from different batch of ASTM A416 steel. The results of 8th cycles of No.1 and No.2 ASTM A416 steels in simulated pore solution are presented in Figure 4-5. The possible oxide film compositions for No.1 steel (labeled (1) in Figure 4-5) are Fe_3O_4, γ-Fe_2O_3, α-FeOOH, FeO, $Fe(OH)_2$. The reactions to form
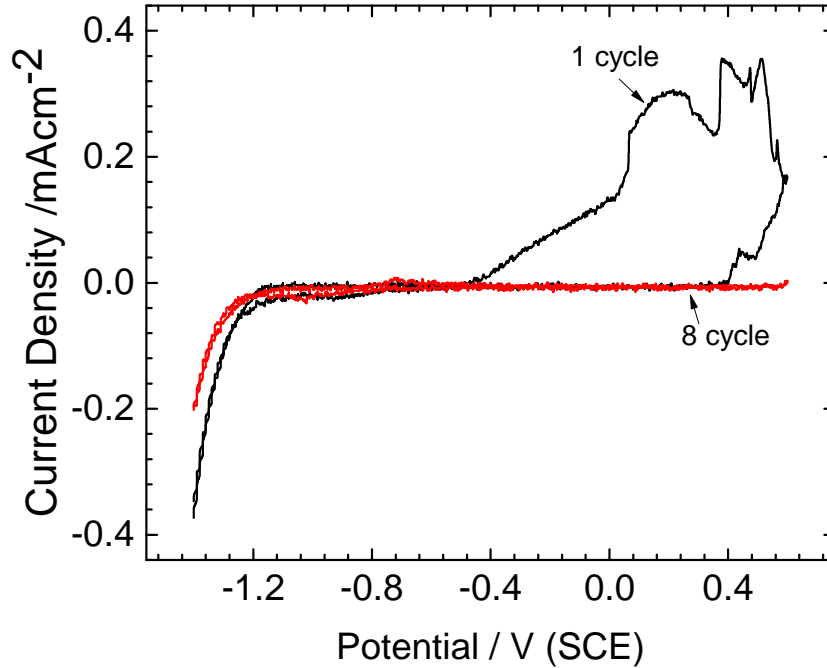
Figure 4-6. Results of the 1st and 8th cyclic voltammograms for ASTM A416 steel in the simulated pore solution with 40g/L NaCl and with a scan rate of 10 mV/s.

γ-Fe_2O_3 and α-FeOOH are

$$Fe_3O_4+2OH^- \rightarrow 3\gamma - Fe_2O_3+H_2O + 2e^- \qquad (4\text{--}8)$$

and

$$Fe_3O_4+OH^-+H_2O \rightarrow 3\alpha-FeOOH+e^- \qquad (4\text{--}9)$$
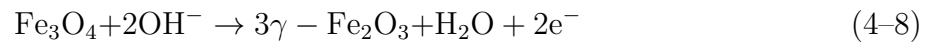
whereas, the possible oxide film compositions for No.2 steel (labeled (2) in Figure 4-5) are FeO, $Fe(OH)_2$ and Fe_3O_4. The corresponding impedance responses for steel (1) and (2) are presented in Figure 4-14, labeled as (1) and (2), respectively. The quality of different batches of steel was further examined by X-ray photonelectron spectroscopy, and the results are presented in Chapter 7.

The pitting potential and repassivation potential can also be found by cyclic voltammetry, shown in Figure 4-6. Pitting clearly occurred during anodic processes

of the first loop, but after the formation of iron compounds during the first cathodic scan, pitting cannot be seen in the 8th loop. From Figure 4-6, the pitting potential is about 0.4 V(SCE) and the repassivation potential is about -0.6 V(SCE). These results support the conclusion that Fe_3O_4, FeO and $Fe(OH)_2$ can form a protective film on the surface of steel. As the concentration of OH^- is about 0.6M, the chloride threshold is about 1.

4.5   Electrochemical Impedance Spectroscopy

Electrochemical impedance spectroscopy is a useful method for analyzing and characterizing the metal-solution interface and oxide films. This method consists of applying a small (5-10mV) alternating potential signal on the electrochemical system and measuring the current response of the system to this perturbation. The impedance can be expressed as the complex ratio of oscillating potential and current

$$Z = \frac{\tilde{V}}{\tilde{i}} = \frac{\Delta V}{\Delta i} e^{j\varphi} = Z_r + jZ_j \tag{4–10}$$

where Z is impedance, j is a complex number equals to $\sqrt{-1}$, φ is the phase difference between the potential and current, and Z_r and Z_j are the real and imaginary components of the impedance, respectively. In order to maintain linearity,[3] the electrochemical system should be perturbed by oscillating potential or current with a significantly small value, which is indicated in Figure 4-7.

Generally, an electrochemical system can be regarded as shown in Figure 4-8.   Here, C_{dl} is double-layer capacitance, R_e is resistance of solution, and Z_f is Faradaic impedance. Faradaic impedance can be referred to charge-transfer resistance, mass transfer resistance, reactions involving adsorbed species, and reactions on non-uniform surfaces.

However, due to the non-uniformity of the metal-solution interface, the constant-phase element (CPE) sometimes needs to be introduced into the equivalent circuits. The origin of non-uniformity can be attributed to the variation of reactivity of current or potential along or normal to the surface of electrode. The mathematical expression of the
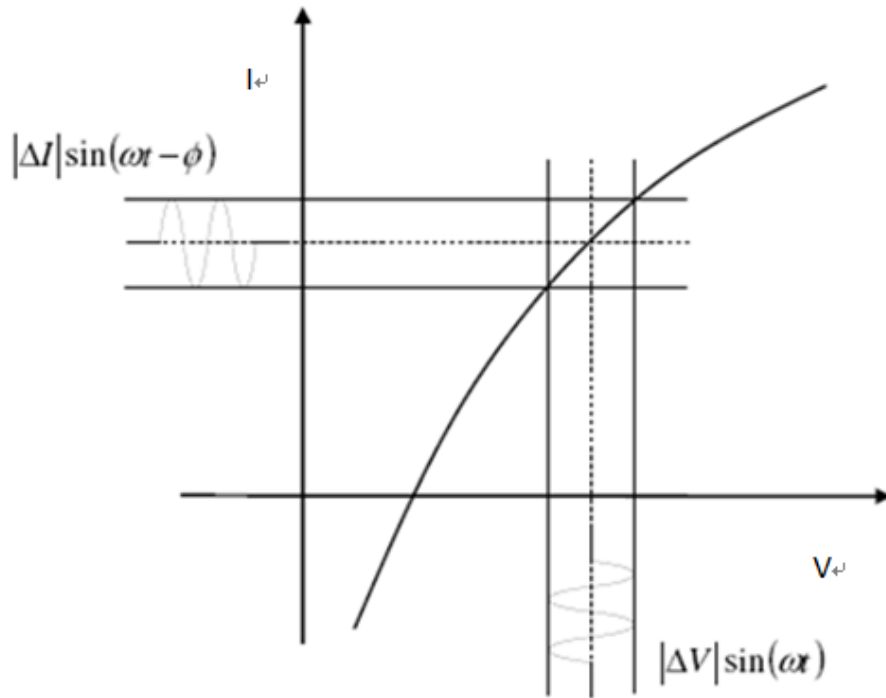
Figure 4-7. Perturbation of an electrochemical system with a small sinusoidal signal at steady-state, where Z_r and Z_j represent the potential and current oscillating at the same frequency ω, and the phase difference between potential and current is ϕ.
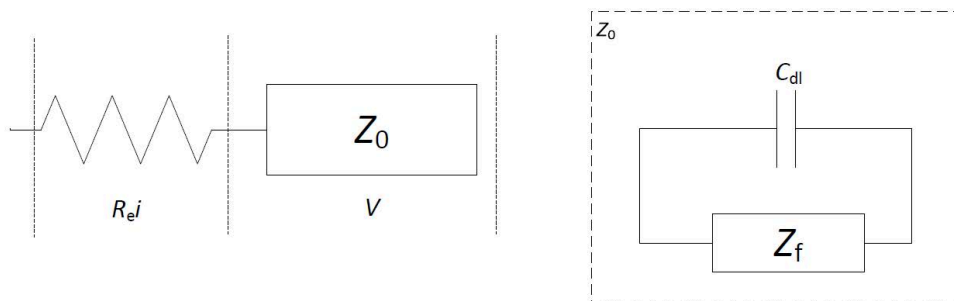
Figure 4-8. An equivalent circuit of representation of an electrode-electrolyte interface. Taken from Orazem and Tribollet.(3)

constant-phase element can be given as

$$Z_{\mathrm{CPE}} = \frac{1}{(j\omega)^\alpha Q} \tag{4–11}$$

When $\alpha = 1$, Q has units of a capacitance, i.e., $\mathrm{F/cm^2}$, and represents the capacity of the interface. When $\alpha < 1$, Q has units of $\mathrm{s^\alpha/\Omega cm^2}$ and the system shows constant-phase behavior. The detailed discussion of constant-phase element is presented in Chapter 5.

The faradaic current density of can be expressed as a function of an interfacial potential V, the surface concentration of bulk species $C_i(0)$, and the surface coverage of the absorbed species γ_k as

$$i_f = f(V, c_i(0), \gamma_k) \tag{4–12}$$

where the interfacial potential V is defined as

$$V = V_m - V_0 \tag{4–13}$$

V_m is the potential of the working electrode, and V_0 is the potential in the electrolyte adjacent to the electrode. The current density can also be expressed in terms of a steady, time-independent term, and an oscillating term as

$$i_F = \bar{i}_F + \mathrm{Re}\left\{\tilde{i}_F e^{jwt}\right\} \tag{4–14}$$

and the Taylor series expansion about $\tilde{i}_F$ can be written as

$$\tilde{i}_F = \left(\frac{\partial f}{\partial V}\right)_{c_i(0),\gamma_k} \tilde{V} + \sum_i \left(\frac{\partial f}{\partial c_i(0)}\right)_{V,c_{l,l\neq i}} \tilde{c}_i(0) + \sum_k \left(\frac{\partial f}{\partial \gamma_k}\right)_{V,c_i(0),\gamma_{l,l\neq k}} \tilde{\gamma}_k \tag{4–15}$$

where $\tilde{V}$, $\tilde{c}_i(0)$, and $\tilde{\gamma}_k$ are assumed to have a small magnitude such that the high-order terms can be neglected. Equation (4–15) represents a general result that can be applied to any electrochemical reaction.

4.5.1 Impedance Model Development

The impedance model developed in this section is based on the electrochemical reactions that may be driven by potential or by both potential and mass-transfer

considerations. The current density of a single reversible reaction can be expressed in terms of Butler-Volmer equation

$$i = i_0 \left\{ \exp(\frac{(1-\alpha)\,n\mathrm{F}}{\mathrm{R}T}\eta_\mathrm{s}) - \exp(-\frac{\alpha n\mathrm{F}}{\mathrm{R}T}\eta_\mathrm{s}) \right\} \tag{4–16}$$

where i_0 is the exchange current density, n is number of electrons involved within the reaction, F is Faraday's constant. The surface overpotential η_s represents the departure from an equilibrium potential such that, at $\eta_\mathrm{s} = 0$, the total current $i=i_\mathrm{a}+i_\mathrm{c}$ is equal to zero. α is apparent transfer coefficient with a value close to 0.5 and must have a value between 0 and 1.

To streamline the discussion of electrochemical kinetics, a more compact notation is used in which

$$b_a = \frac{(1-\alpha)\,n\mathrm{F}}{\mathrm{R}T} \tag{4–17}$$

for anodic reactions and for cathodic reactions

$$b_c = \frac{\alpha n\mathrm{F}}{\mathrm{R}T} \tag{4–18}$$

At very positive potentials, the cathodic term is negligible, and the current density can be expressed as

$$i = i_0 \exp(b_a \eta_\mathrm{s}) \tag{4–19}$$

Similarly, at very negative potentials, the anodic term is negligible, and the current density can be expressed as

$$i = -i_0 \exp(-b_c \eta_\mathrm{s}) \tag{4–20}$$

The anodic reaction for steel corrosion is iron dissolution

$$\mathrm{Fe} \rightarrow \mathrm{Fe}^{2+} + 2\mathrm{e}^- \tag{4–21}$$
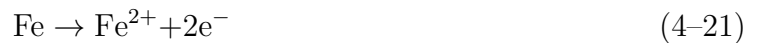
and its corresponding current density is

$$i_\mathrm{Fe} = K_\mathrm{Fe}^* \exp\{b_\mathrm{Fe}(\bar{V} - V_\mathrm{Fe,0})\} \tag{4–22}$$

where $K_{\text{Fe}}^* = n\text{F}k_{\text{Fe}}$. From equation (4–15), the oscillating anodic current density can be expressed as

$$\tilde{i}_{\text{Fe}} = K_{\text{Fe}} \exp\{b_{\text{Fe}}(\bar{V})\} b_{\text{Fe}} \tilde{V} \tag{4–23}$$

$K_{\text{Fe}} = K_{\text{Fe}}^* \exp(-b_{\text{Fe}} V_{0,\text{Fe}})$ and the Faradaic impedance of iron dissolution can be expressed as

$$Z_{\text{Fe}} = \frac{\tilde{V}}{\tilde{i}_{\text{Fe}}} = \frac{1}{K_{\text{Fe}} \exp\left(b_{\text{Fe}} \bar{V}\right) b_{\text{Fe}}} \tag{4–24}$$

The cathodic reaction for steel corrosion is oxygen reduction

$$\text{O}_2 + 4\text{H}^+ + 4\text{e}^- \rightarrow 2\text{H}_2\text{O} \tag{4–25}$$

The corresponding steady-state current density is given by

$$\bar{i}_{\text{O}_2} = -K_{\text{O}_2} \bar{C}_{\text{O}_2}(0) \exp(-b_{\text{O}_2} \bar{V}) \tag{4–26}$$

where K_{O_2} is equals to $n\text{F}k_{\text{o}_2} \exp\left(-b_{\text{o}_2} V_{0,\text{o}_2}\right)$. From equation (4–15), the oscillating cathodic current density can be expressed as

$$\tilde{i}_{\text{O}_2} = K_{\text{O}_2} b_{\text{O}_2} \tilde{c}_{\text{O}_2}(0) \exp\left(b_{\text{O}_2} \overline{V}\right) \tilde{V} + K_{\text{O}_2} \exp\left(b_{\text{O}_2} \overline{V}\right) \tilde{c}_{\text{O}_2}(0) \tag{4–27}$$

Since the reaction above depends on variation of concentration, to solve the relationships between the oscillating component of the current density and the oscillating component of the interfacial potential, a second equation is needed.

To derive the second equation, the current density on the electrode surface can be used. The current density may be related to the flux of reactant to the surface, according to

$$i_{\text{O}_2} = -n_{\text{O}_2} \text{F} D_{\text{O}_2} \left.\frac{dC_{\text{O}_2}}{dy}\right|_{y=0} \tag{4–28}$$

Equation (4–28) may be written in terms of dimensionless position $\xi = y/\delta_{O_2}$ and dimensionless concentration $\theta_{\text{O}_2} = \tilde{C}_{\text{O}_2}/\tilde{C}_{\text{O}_2}(0)$ as

$$\tilde{i}_{\text{O}_2} = n_{\text{O}_2} \text{F} D_{\text{O}_2} \frac{\tilde{C}_{\text{O}_2,0}}{\delta_{\text{O}_2}} \theta'_{\text{O}_2}(0) \tag{4–29}$$

from equations (4–27) and (4–29), $\tilde{C}_{O_2,0}$ can be eliminated to obtain

$$\widetilde{i}_{O_2} = \frac{\tilde{V}}{Z_{O_2}} = \frac{\tilde{V}}{R_{t,O_2} + Z_{D,O_2}} \tag{4–30}$$

where

$$Z_{D,O_2} = \frac{\delta_{O_2}}{n_{O_2} b_{O_2} F D_{O_2}} \left(\frac{-1}{\theta'_{O_2}(0)} \right) \tag{4–31}$$

and

$$R_{t,O_2} = \frac{1}{K_{O_2} b_{O_2} \exp\left(b_{O_2} \bar{V}\right)} \tag{4–32}$$

4.5.2   Impedance Data

The influence of chloride ions, dissolved oxygen content, and elapsed time on the corrosion behavior of ASTM A416 steel in simulated pore solution was investigated by electrochemical impedance spectroscopy.

4.5.2.1   Influence of chloride ions and dissolved oxygen content

Based on the cyclic voltammetry results, the chloride threshold level for ASTM A416 steel is about 1. In this section, 40g/L of NaCl was added to simulated pore solution to test the corrosion behavior of ASTM A416 steel in a chloride contaminated environment. The anaerobic corrosion behavior of ASTM A416 steel was also tested by sparging BIP grade nitrogen gas (Airgas), with guaranteed 99.9999% purity, to deaerate the system through a microporous glass frit for at least 1.5 h.

All electrochemical impedance diagrams were recorded at the corrosion potential E_{corr} after the electrode was conditioned for one hour at -1 V(Hg/HgO) and then held at the open circuit condition for one hour. The impedance scans can be represented by two capacitive loops: a high-frequency (HF) loop with low capacitance, and a low-frequency (LF) loop which may include the diffusion impedance.

The impedance response of steel in chloride-free aerated electrolytes (SPS-A in Table 4-1) is presented in Figure 4-9 with elapsed time as a parameter. After an elapsed time of one hour, the low-frequency feature was a straight line with an angle of approximately

Table 4-1. Recipe for the simulated pore solution taken from Li and Sagüès,[1] and the resulting pH value.

SPS	Ca(OH)$_2$	NaOH	KOH	pH	NaCl	Deaerated
A	2 (g/L)	8.33 (g/L)	23.3 (g/L)	13.8	0	no
B	2 (g/L)	8.33 (g/L)	23.3 (g/L)	13.8	40	no
C	2 (g/L)	8.33 (g/L)	23.3 (g/L)	13.8	0	yes
D	2 (g/L)	8.33 (g/L)	23.3 (g/L)	13.8	40	yes

Figure 4-9. Impedance response of the ASTM A416 steel at the open-circuit potential, immersed in chloride-free aerated solution (SPS-A) with elapsed time as a parameter.

22.5 degrees with respect to the real axis. After an elapsed time of 18 hours, the size of the high-frequency capacitive loop increased, and the angle of the low-frequency line approached 45 degrees. After 36 hours, the size of the high-frequency capacitive loop decreased, and the angle of the low-frequency line was 43 degrees.

The impedance response of steel in aerated electrolytes with 40g/L NaCl (SPS-B in Table 4-1) is presented in Figure 4-10 with elapsed time as a parameter. After an immersion time of one hour, the low-frequency feature was a straight line with an angle of 25 degrees with respect to the real axis. After an elapsed time of 18 hours, the size of the high-frequency capacitive loop increased, and the angle of the low-frequency line
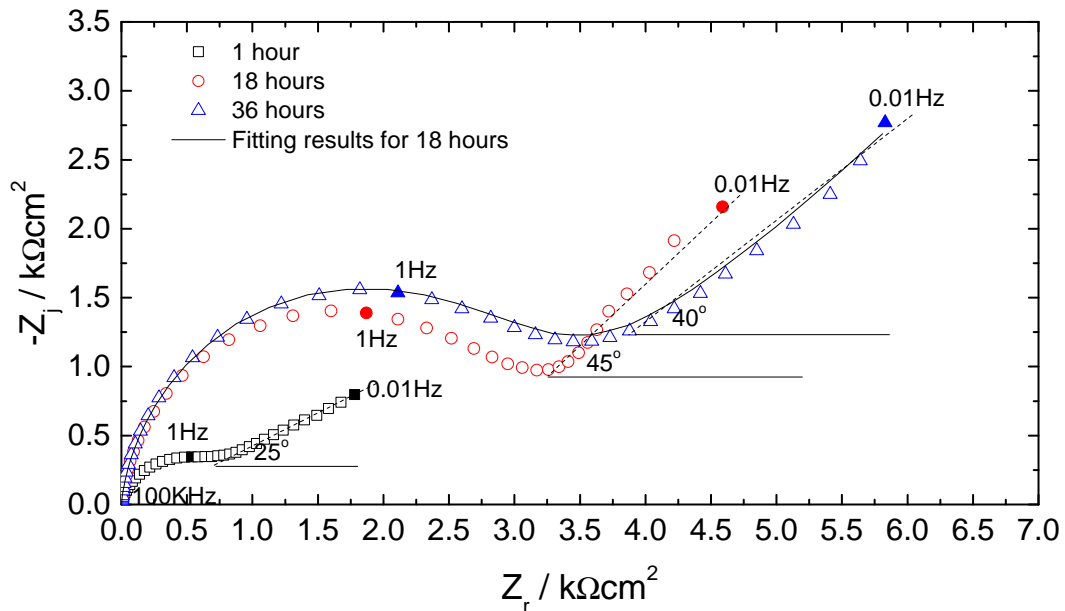
Figure 4-10. Impedance response of the ASTM A416 steel at the open-circuit potential steel immersed in 40g/L chloride aerated solution (SPS-B), with elapsed time as a parameter.

approached 45 degrees. After 36 hours, the size of the high-frequency capacitive loop was further increased, and the angle of the low-frequency line was 40 degrees. The impedance data showed similar behavior as compared to that seen in chloride-free electrolytes (Figure 4-9). This result suggests that, even when the chloride concentration is higher than the chloride threshold level, no corrosion damage can occur if the surface potential remains lower than the pitting potential.

The impedance response of steel in chloride-free deaerated electrolytes (SPS-C in Table 4-1) is presented in Figure 4-11 with elapsed time as a parameter. After one hour, the low-frequency feature was a straight line with an angle of 26 degrees with respect to the real axis. In contrast to the results obtained in aerated electrolytes (Figures 4-11 and 4-12), the low-frequency line remained at 26 or 27 degrees, even after 36 hours. The high-frequency capacitive loop increased for scans from 1 to 18 hours of elapsed time, but did not change between 18 and 36 hours of elapsed time. The impedance response of steel

in deaerated electrolytes with 40g/L NaCl (SPS-D in Table 4-1) is presented in Figure 6 with elapsed time as a parameter. After one hour, the low-frequency feature was a straight line with an angle of 22.5 degrees with respect to the real axis. After 18 hours, the low-frequency feature had a slight curvature. The curvature of the low-frequency feature was more pronounced at 36 hours, and its high-frequency slope with respect to the real axis was 37 degrees. In spite of the curvature of the low-frequency loop, steel immersed in this electrolyte showed no visible corrosion damage. This result is in agreement with observations in other aerated and deaerated electrolytes. For all cases with immersion times of one hour, the low-frequency loop shows an angle of approximately 22.5 degrees with respect to the real axis. This suggests that the ASTM A416 electrode behaves as a semi-infinite porous medium, in agreement with the theory of de Levie.(40) After 18 hours, the high-frequency part of the low-frequency feature in the aerated electrolytes approached 45 degrees, as would be consistent with semi-infinite Warburg diffusion impedance for a planar electrode. In contrast, a low-frequency slope of 45 degrees was not observed in deaerated electrolytes, even after 36 hours of immersion. The behavior of the ASTM 416 electrode in the deaerated electrolyte corresponded to mass-transfer to a porous electrode with pores of finite depth.

The porous electrode behavior can be observed for all impedance data presented in this section. These results suggested that corrosion behavior of ASTM A416 steel is not significantly influenced by chloride ions or by dissolved oxygen content.

4.5.2.2   Influence of elapsed time

Impedance diagrams are presented in Figures 4-13 and 4-14   for the No.1 ASTM A416 steel disk electrode at the open-circuit potential after an elapsed time of 7.2 ks (2 h) and after steady-state was reached. An angle of 33 degrees with respect to the real axis was observed after 7.2 ks (2 h) in the frequency range from 10 to 1 Hz. The angle less than 45 degress suggests porous electrode behavior. The slight curvature in the impedance data after 1 Hz suggests that a finite value for corrosion rate may be
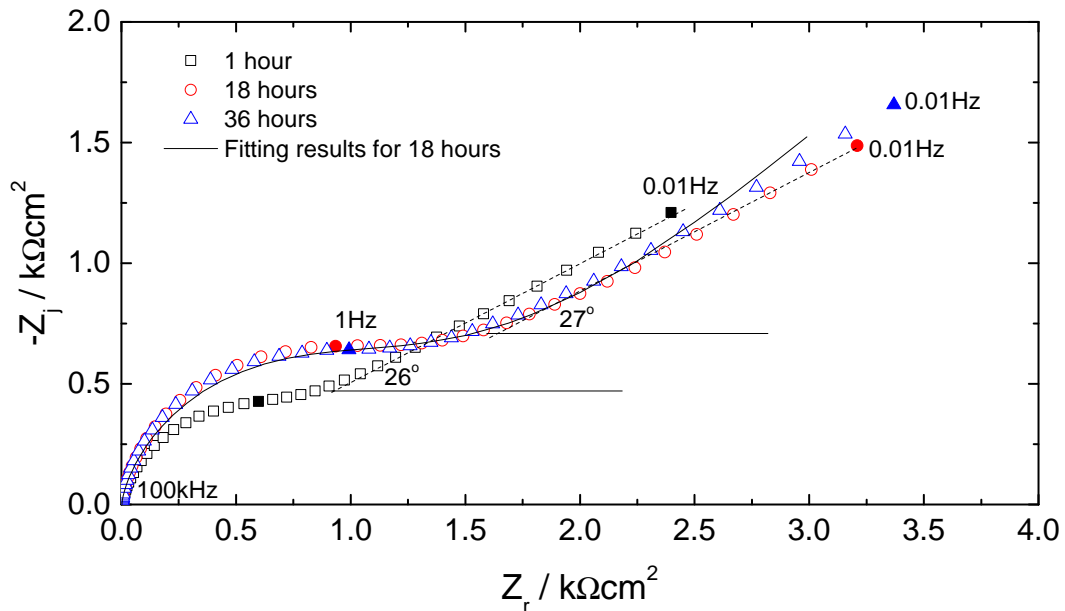
Figure 4-11. Impedance response of the ASTM A416 steel at the open-circuit potential immersed in chloride-free deaerated solution (SPS-C) with elapsed time as a parameter.

estimated. The low–frequency impedance data collected after steady–state was reached reveals an angle of 44 degress (label (1) in Figure 4-14) or 65 degress (label (2) in Figure 4-14) with respect to the real axis. An angle of low–frequency impedance data less than 45° suggests that porous electrode behavior is evident to a lesser degree. Whereas, the angle of low–frequency impedance data more than 45° degree suggests that porous electrode behavior is completely diminished. For both cases, the low–frequency data show a straight-line, suggesting that, after 300 ks, the corrosion rates were too small to be measured. Thus, the results presented in Figure 4-14 indicate that the level of passivity of ASTM A416 steel at the open–circuit potential in alkaline simulated pore solution increased with time.

To show more clearly the high–frequency results in Figures 4-13 and 4-14, the phase angle and magnitude of impedance are presented in Figures 4-15 and 4-16.   The phase
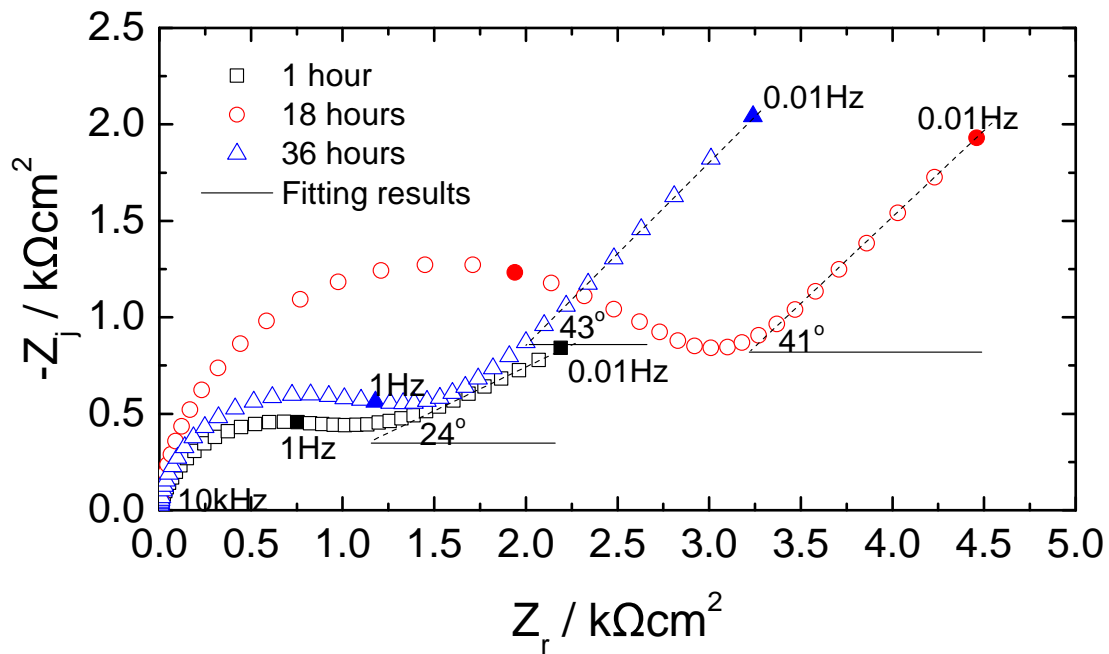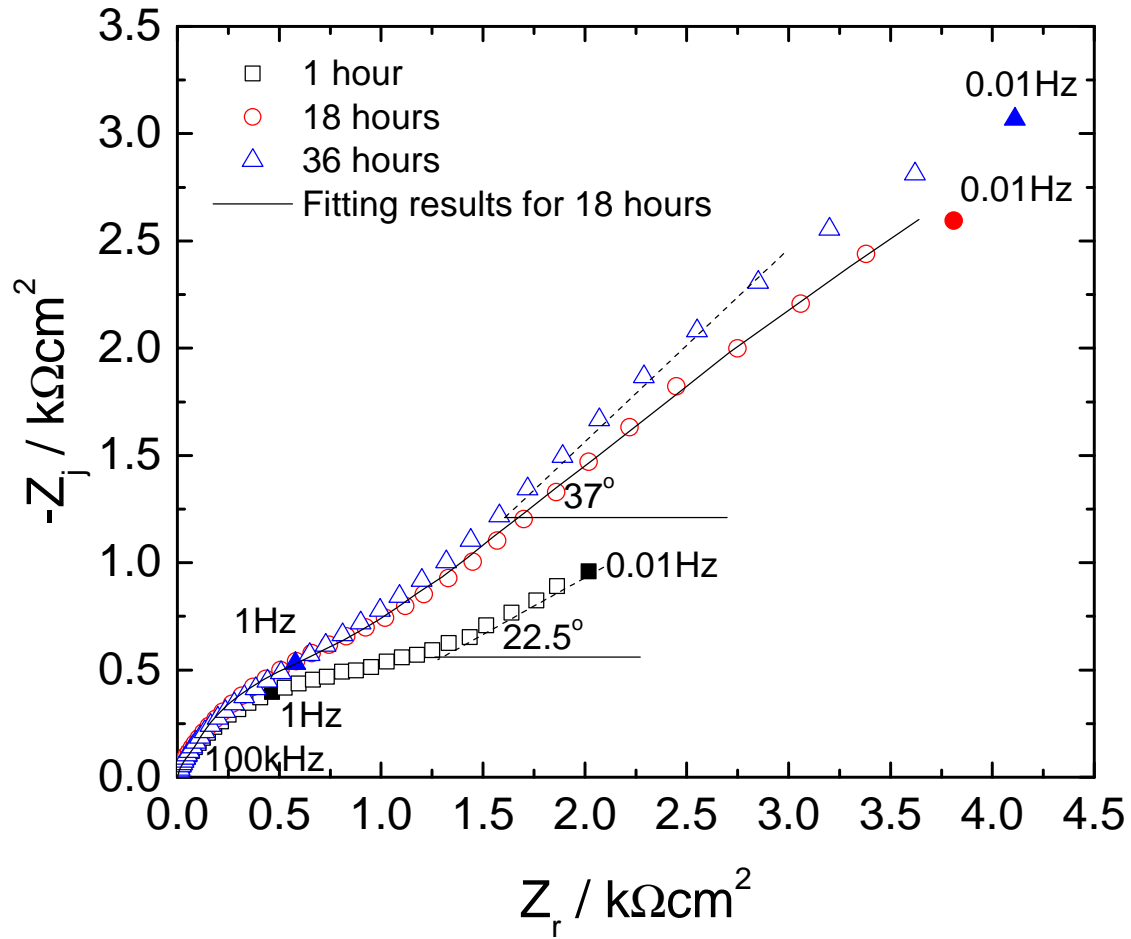
Figure 4-12. Impedance response of the ASTM A416 steel at the open-circuit potential steel immersed in 40g/L chloride deaerated solution (SPS-B) with elapsed time as a parameter.

angle was defined following Alexander et al. (41) as

$$\varphi_{\mathrm{dZj}} = 90 \frac{\mathrm{d}\log|Z_{\mathrm{j}}|}{\mathrm{d}\log f} \tag{4–33}$$

The phase-angle information at low frequency is consistent with the information obtained from the Nyquist plots in Figure 4-13 and 4-14. After a short exposure, the phase angle defined by equation (4–33) reaches a plateau value of 33 degrees. After a steady–state condition was obtained, the phase angle had a value of 44 degrees or 65 degrees at low frequency. To emphasize the comparison between model and data at high frequency, the
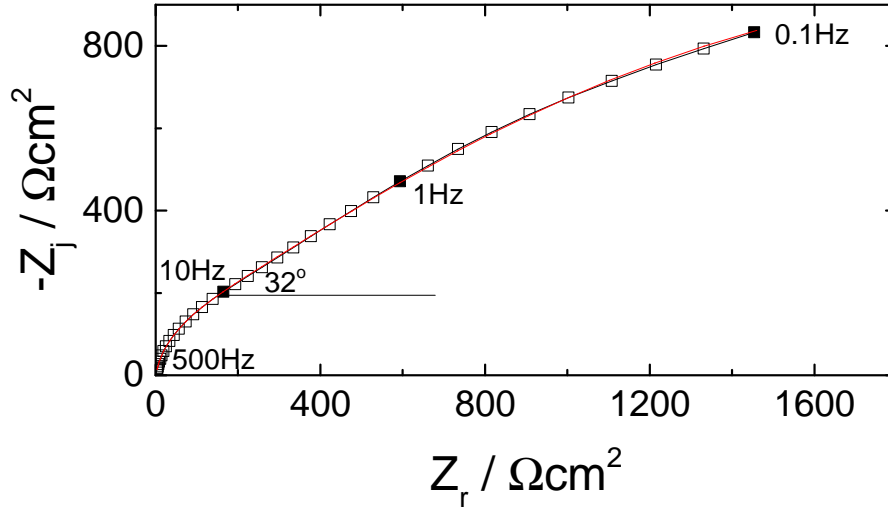
Figure 4-13. Impedance response of the stationary No.1 ASTM A416 steel disk electrode at the open-circuit potential after an elapsed time of 7.2 ks (2 h). The line represent the regression of equation (5–38) to the data.

magnitude presented in Figure 4-16 was adjusted by subtracting the ohmic resistance, following Orazem et al. (42), i.e.,

$$|Z| = \sqrt{(Z_\mathrm{r} - R_\mathrm{e})^2 + Z_\mathrm{j}^2} \qquad (4\text{--}34)$$

The match between the model values and data shown in Figures 4-15 and 4-16 suggest that the process model discussed in next section provides an excellent fit to the data.

Impedance measurements were performed at specified potentials. The protocol followed allowed the system to reach a steady state at the open–circuit condition. This step required up to 300 ks. The potential was then adjusted to a value referenced to the open–circuit potential. The system was allowed to remain at the applied potential until the current density reached a steady value. As shown in Figure 4-3, this step required as much as 250 ks.

The resulting impedance values of No.1 and No.2 ASTM A416 steel for potentials negative of the corrosion potential are presented in Figures 4-17 and 4-18, respectively,
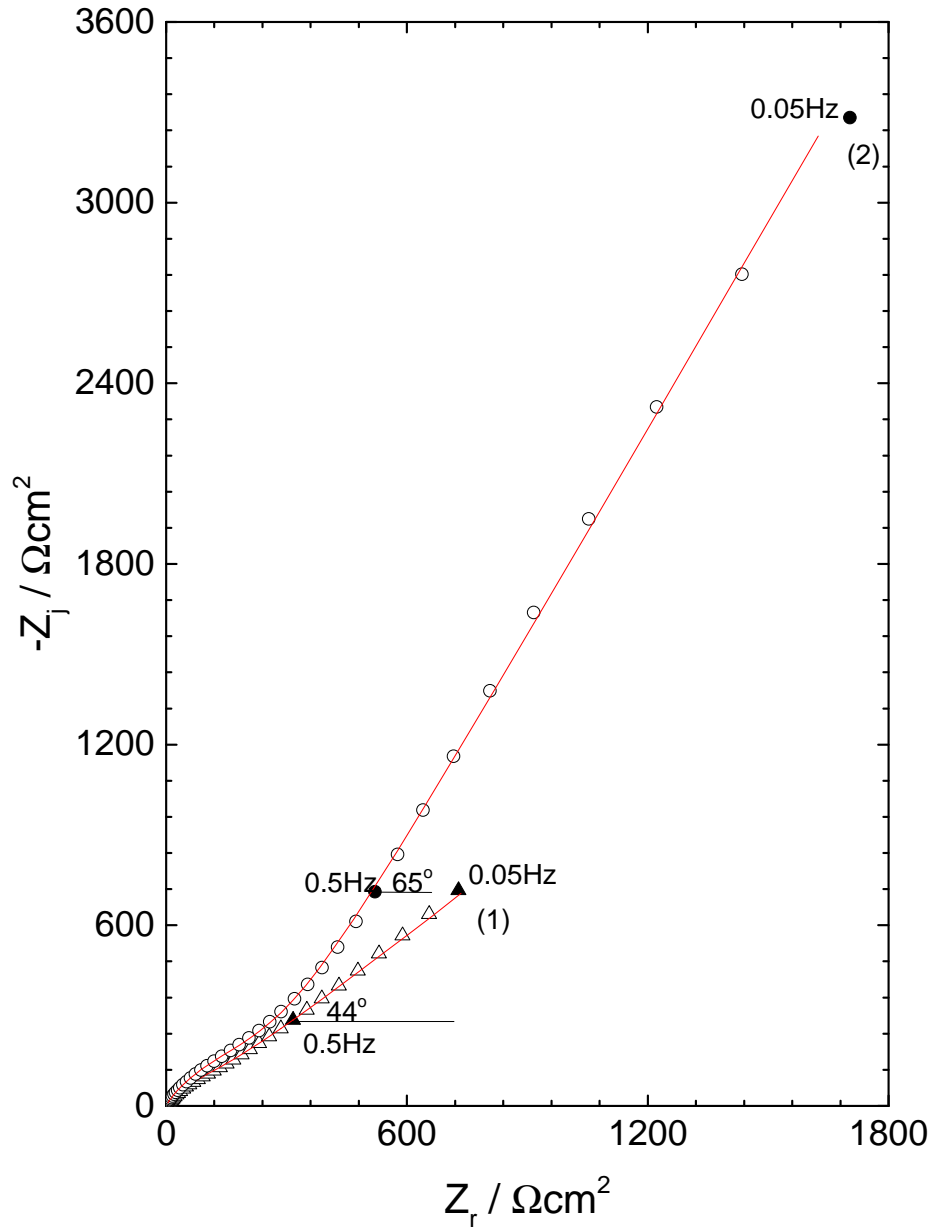
Figure 4-14. Impedance response of the stationary ASTM A416 steel disk electrode at the open-circuit potential after steady-state was reached. The line represent the regression of equation (5–38) to the data.
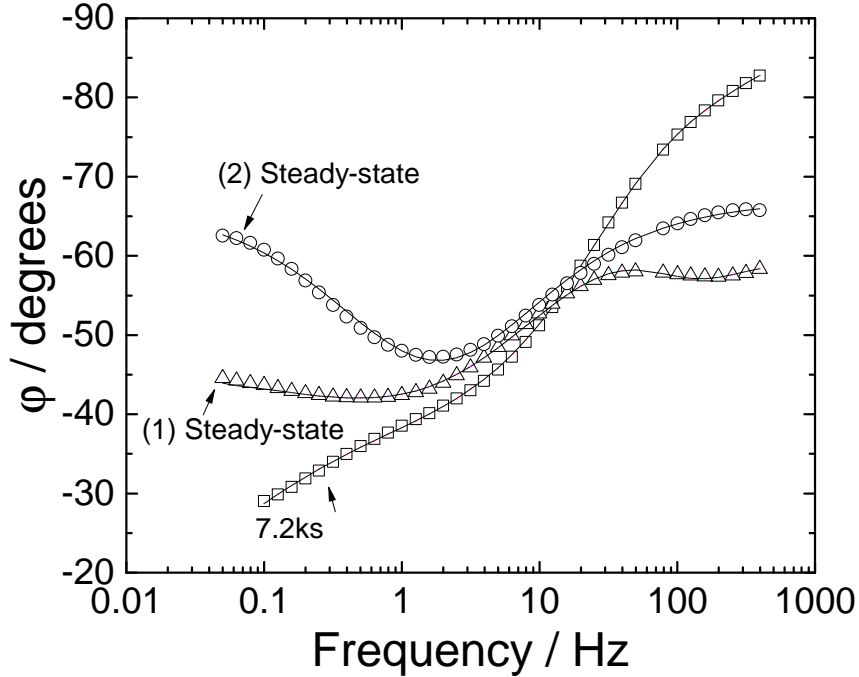
Figure 4-15. Impedance phase angle, obtained from equation (4–33), for the stationary ASTM A416 steel disk electrode at the corrosion potential after an elapsed time of 7.2 ks (2 h) and after steady-state was reached. The lines represent the regression of equation (5–38) to the data.

 with applied potential as a parameter. The magnitude of the impedance decreased as the applied potential changed to more cathodic values, reflecting the increased current density at more negative applied potentials. The low–frequency impedance data showed a straight line, suggesting that the corrosion rate cannot be estimated for these cases. The slope of the low–frequency part decreased with decreasing potential for both No.1 and No.2 ASTM A416 steels.

The impedance values of No.1 ASTM A416 for potentials positive of the corrosion potential are presented in Figure 4-19, with applied potential as a parameter. The impedance data obtained at potentials of +0.02 V(Hg/HgO) and +0.12 V(Hg/HgO) are similar to the impedance data obtained at the open-circuit potential. The lack of variability of the impedance is in agreement with the fixed value of anodic current
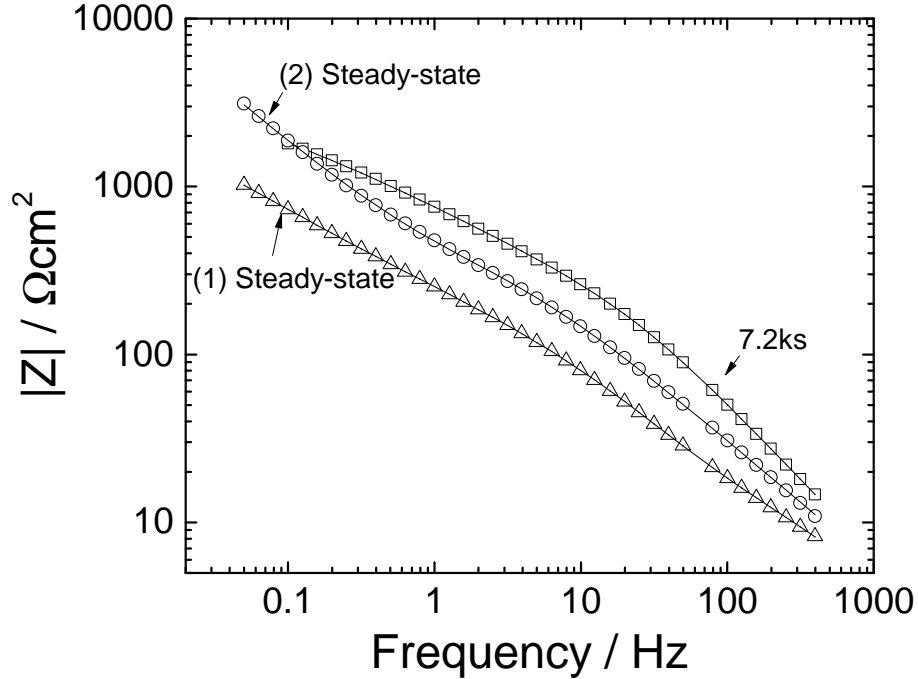
Figure 4-16. Ohmic–resistance–corrected magnitude of the impedance, obtained from equation (4–34), for the stationary ASTM A416 steel disk electrode at the corrosion potential after an elapsed time of 7.2 ks (2 h) and after steady-state was reached. The lines represent the regression of equation (5–38) to the data.

reported in Figure 4-1 for +0.02 V(Hg/HgO) and +0.12 V(Hg/HgO). The impedance shows markedly different behavior at the more anodic potential of +0.22 V(Hg/HgO). The low–frequency part of the impedance data obtained at +0.22 V(Hg/HgO) shows a slight curvature, suggesting a measurable corrosion rate.

The impedance values of No.1 ASTM A416 for potentials positive of the corrosion potential are presented in Figure 4-20. The magnitude of impedance data from No.2 ASTM A416 steel obtained at potentials of +0.02 V(Hg/HgO) to +0.22 V(Hg/HgO) increased with applied potential. This behavior is very different from the impedance data obtained from No.1 ASTM A416 steel. For all the impedance data presented in Figure 4-20, a slight curvature for low–frequency part of the impedance data cannot be observed,
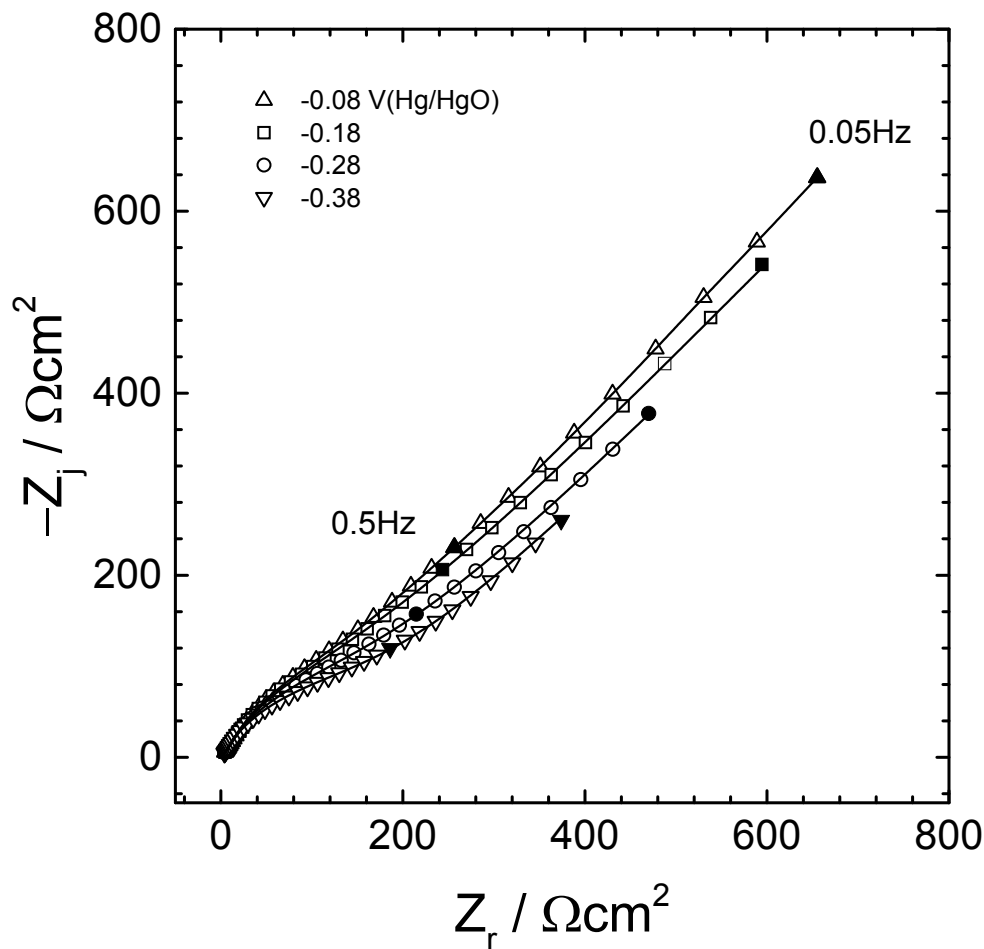
Figure 4-17. Impedance response of the stationary No.1 ASTM A416 steel electrode with positive applied potential as a parameter. The lines represent the regression of equation (5–38) to the data.

suggesting that the corrosion rate cannot be measured for No.2 ASTM A416 steel, even with applied potential.

For the data from No.1 ASTM A416 steel presented in Figures 4-13, 4-14, 4-17, and 4-19, the low–frequency data points show an angle between 22.5° to 45° with respect to the real axis. An angle less than 45° with respect to the real axis angle suggests that the ASTM A416 steel behaves as porous electrode, in agreement with the theory of de Levie.(40) Bouzek and Rousar suggested that porous electrode behavior can result when an air–formed oxide film is removed from the surface of the steel electrode by cathodic pretreatment, resulting in an ion-permeable porous iron.(43) Büchler and Schöneich(44)
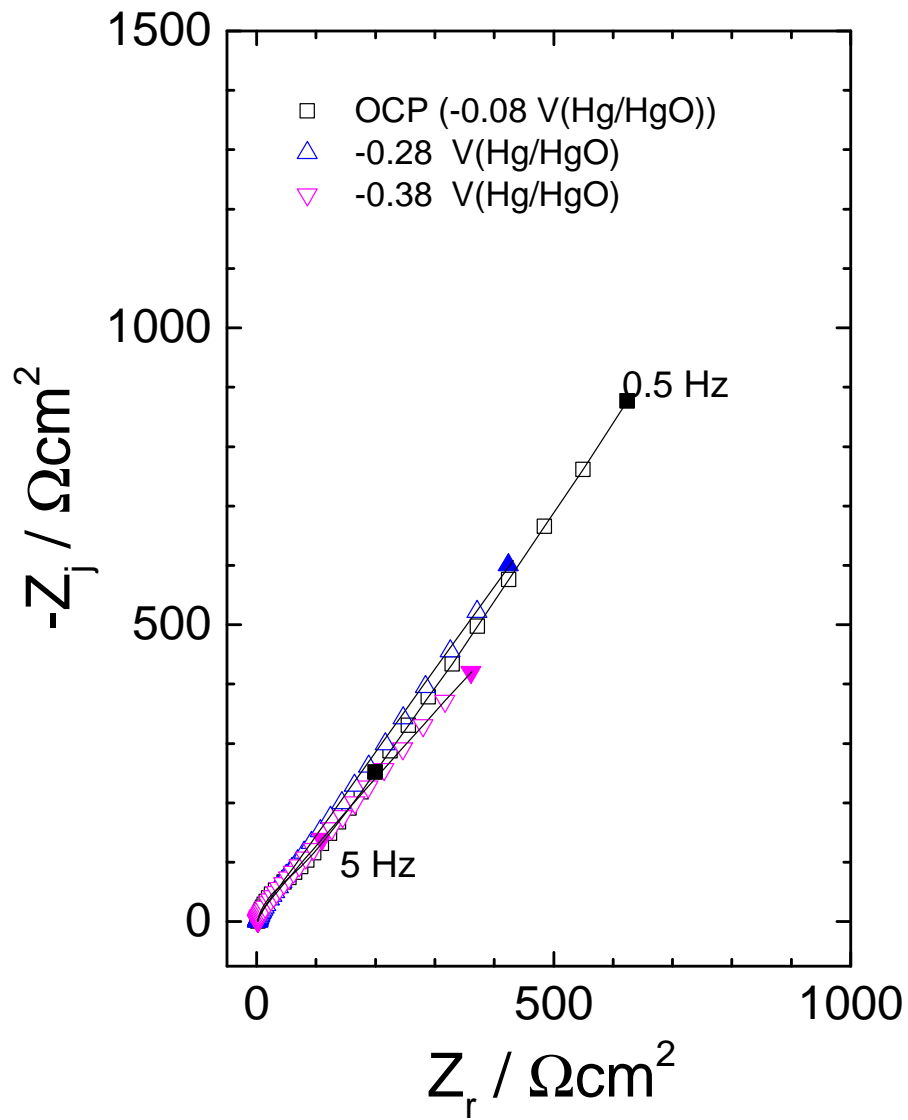
Figure 4-18. Impedance response of the stationary No.2 ASTM A416 steel electrode with negative applied potential as a parameter. The lines represent the regression of equation (5–40) to the data.
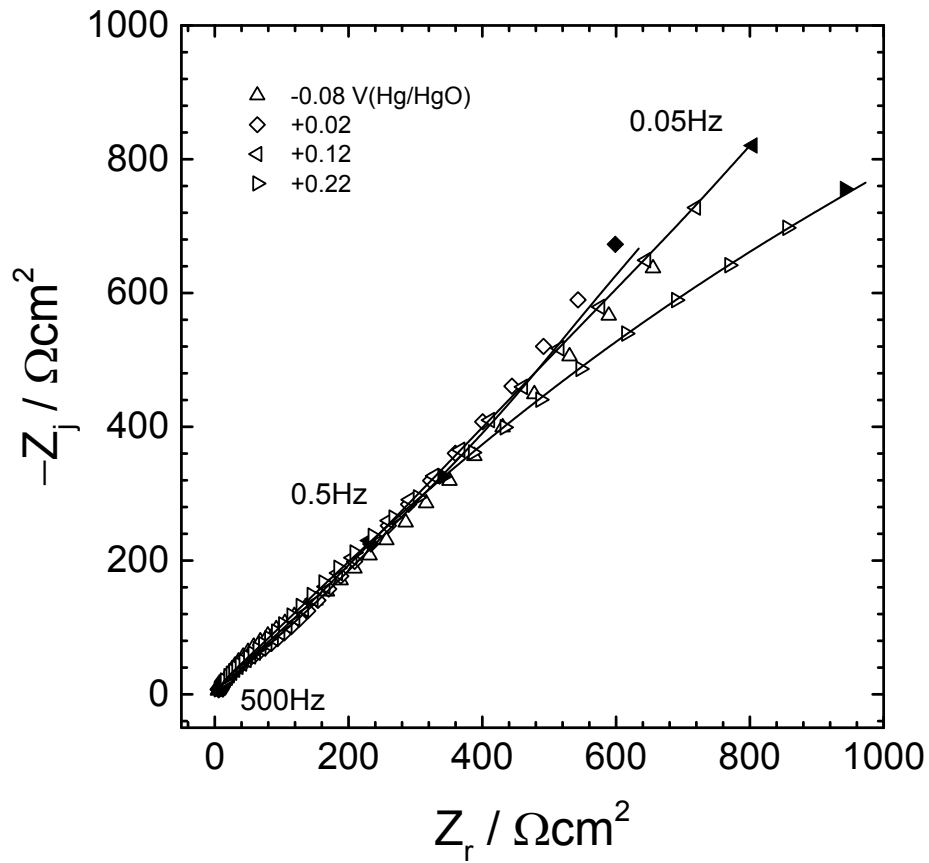
Figure 4-19. Impedance response of the stationary No.1 ASTM A416 steel electrode with positive applied potential as a parameter. The lines represent the regression of equation (5–38) to the data.

suggested that the cathodic polarization results in the reduction of the passive film, thereby accumulating a porous rust layer on the metal surface. If low–frequency data points show an angle larger than 45 degrees, porous electrode behavior is diminished. Therefore, different process models are required to analyze data from No.1 and No.2 ASTM A416 steel.
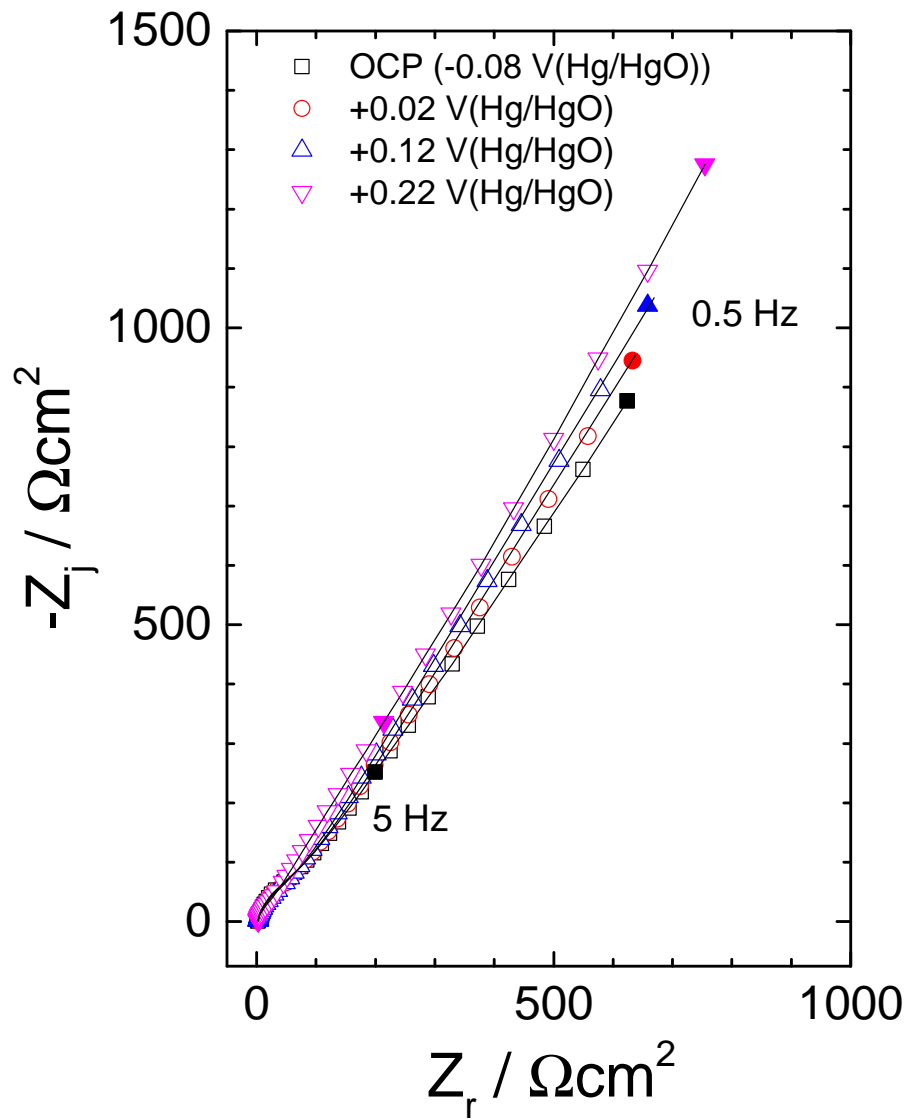
Figure 4-20. Impedance response of the stationary No.2 ASTM A416 steel electrode with applied potential as a parameter. The lines represent the regression of equation (5–40) to the data.

CHAPTER 5
ELECTROCHEMICAL IMPEDANCE SPECTROSCOPY ANALYSIS

The impedance data were analyzed by use of both measurement and process models. The measurement model was used to provide a statistical analysis of the data; whereas, the process model was used to provide an interpretation based on physical and chemical phenomena. The oxide film thickness and corrosion rate was also estimated by use of the power-law model and anodic charge transfer resistance, $R_{t,a}$, respectively.

5.1 Measurement Model Analysis

The impedance data may be corrupted by different errors. Generally, these errors can be classified into three different sources: the contribution of these errors can be expressed by the difference between the observed value $Z_{ob}(\omega)$, and a model value $Z_{mod}(\omega)$ as

$$Z_{ob}(\omega) - Z_{mod}(\omega) = \varepsilon_{fit}(\omega) + \varepsilon_{stoch}(\omega) + \varepsilon_{bias}(\omega) \tag{5-1}$$

where $\varepsilon_{fit}(\omega)$ is the systematic error caused by the inadequacies of the model, $\varepsilon_{stoch}(\omega)$ is the stochastic error, and $\varepsilon_{bias}(\omega)$ represents the systematic experimental bias error that is not considered in the model's inadequacies. The error $\varepsilon_{stoch}(\omega)$ comes from the integration of time-domain signals that contain noise from thermal fluctuations of resistivity, thermal fluctuations of concentration and rates of electrochemical reactions, instrument sources, and stochastic events such as bubble formation in the electrolyte and pitting on the electrode surface. Bias errors are systematic errors, for which the mean value is non-zero, which cannot be attributed to an inadequate descriptive model of the system. Generally, bias errors come from instrument artifacts and non-stationary behavior of the system. For example, the impedance response of the high-frequency part may include the finite impedance behavior of wires and connectors. The reference electrode can also contribute to high-frequency artifacts. Non-stationary behavior of the system may caused by from the growth of surface films and changes in concentrations of reactants or products in the electrolyte.(3)

The measurement model analysis developed by Agarwal et al.(45; 46; 47) was used to identify the error structure of the impedance data. A model for the error structure can be expressed as

$$\sigma_{Z_r}(\omega) = \sigma_{Z_j}(\omega) = \kappa |Z_j| + \beta |Z_r - R_e| + \gamma \frac{|Z|^2}{R_m} + \delta \tag{5–2}$$

where σ_{Z_r} and σ_{Z_j} represent the standard deviation of the real and imaginary parts of the impedance, respectively, R_e is the ohmic resistance of the solution, R_m corresponds to the current measuring resistor, and $|Z_r|$ and $|Z_j|$ are experimental values that are functions of frequency.

A model for the stochastic error for this present dissertation was identified from a measurement model analysis of replicated spectra to be

$$\sigma_{Z_r}(\omega) = \sigma_{Z_j}(\omega) = 9.39 \times 10^{-4} |Z_r - R_e| + 4.03 \times 10^{-7} \frac{|Z|}{R_m} \tag{5–3}$$

for both impedance data from No.1 and No.2 steels. Tests for consistency with the Kramers–Kronig relations were applied, as described in reference (47), to determine the portion of the frequency range that could be used for subsequent regression analysis.

5.2   Characteristic Frequency Analysis

The frequency $K = \pi/4$ at which the current and potential distributions begin to influence the impedance response can be expressed as

$$f_{c,disk} = \frac{1}{2\pi} \frac{4\kappa}{\pi C_0 r_0} \tag{5–4}$$

The influence of high-frequency geometry-induced time-constant dispersion can be avoided for reactions that do not involve adsorbed intermediates by conducting experiments below the characteristic frequency given in equation (5–4).(48) For example, from the values of the regressed parameters of impedance data after 300ks in Table 8-2, the characteristic frequency is 2200 Hz. Therefore, the impedance data measured higher than 2200Hz should be removed before further analysis.

5.3   Fitting Procedure

The regression of models to impedance data generally applies a complex nonlinear application of the method of least squares. (49; 50; 51) Complex nonlinear least-squares regression techniques are an extension of non-linear least squares regression techniques. The use of complex nonlinear least square is consistent with the expectation that the real and imaginary components of impedance data satisfy the constraints of the Kramers-Kronig relations.(52; 53)

5.3.1   Linear Regression

Consider a general model of the form(54; 55)

$$y(x) = \sum_{k=1}^{N_p} P_k X_k(x) \tag{5--5}$$

where $X_k(x)$ are basis functions defined by arbitrary fixed functions of x and N_P represents the number of adjustable parameters P_k in the model.

A least-squares regression involves minimization of the objective function

$$\chi^2 = S(P) = \sum_{i=1}^{N_{dat}} \frac{\left(y_i - \sum_{k=1}^{N_P} P_k X_k(x_i)\right)^2}{\sigma_i^2} \tag{5--6}$$

where y_i represents the measured values, and σ_i represents the standard deviation of measurement i. The derivative with respect to the parameters P_k vanishes at minimum value. Therefore,

$$\sum_{i=1}^{N_{dat}} \frac{\left(y_i - \sum_{k=1}^{N_P} P_k X_j(x_i)\right)}{\sigma_i^2} X_k(x_i) = 0 \tag{5--7}$$

Equation (5–7) represents a set of N_p equations of the form

$$\sum_{j}^{N_p} \alpha_{k,j} P_j = \beta_k \tag{5--8}$$

where

$$\beta_k = \sum_{i=1}^{N_{dat}} \frac{(y_i X_k(x_i))}{\sigma_i^2} \tag{5--9}$$

and

$$\alpha_{k,j} = \sum_{i=1}^{N_{dat}} \frac{(X_k(x_i) X_j(x_i))}{\sigma_i^2} \tag{5-10}$$

Equation (5–8) can be written in vector form as

$$\alpha \cdot P = \beta \tag{5-11}$$

or

$$P = \alpha^{-1} \cdot \beta = C \cdot \beta \tag{5-12}$$

The inverse matrix $C = \alpha^{-1}$ provides an estimate for the confidence intervals for the estimated parameters. The diagonal elements of [C] are the variances of the fitted parameters.

5.3.2 Nonlinear Regression

To achieve the least-squares regression,(55) consider a general nonlinear function that has nonlinear behavior with respect to parameters P_k. Under the assumption that $f(P)$ is twice continuously differentiable, a Taylor series expansion about a parameter set P_0 yields

$$f(P) = f(P_0) + \sum_i^{N_k} \left.\frac{\partial f}{\partial P_i}\right|_{P_0} \Delta P_i + \frac{1}{2} \sum_i^{N_k} \sum_j^{N_k} \left.\frac{\partial^2 f}{\partial P_i \partial P_j}\right|_{P_0} \Delta P_i \Delta P_j + ... \tag{5-13}$$

The optimum for P is found when $f(P)$ has a minimum value. At the minimum, derivatives with respect to the parameter increments ΔP_i should be equal to zero; thus,

$$\frac{\partial f}{\partial \Delta P_i} = \left.\frac{\partial f}{\partial P_i}\right|_{P_0} + \sum_j^{N_k} \left.\frac{\partial^2 f}{\partial P_i \partial P_j}\right|_{P_0} = 0 \tag{5-14}$$

Equation (5–14) represents a set of N_p equations of the form

$$\beta_j = \sum_k^{N_p} \alpha_{j,k} \Delta P_k \tag{5-15}$$

where

$$\beta_j = -\frac{1}{2} \left.\frac{\partial f}{\partial P_j}\right|_{P_0} \tag{5-16}$$

and

$$\alpha_{j,k} = \frac{1}{2} \frac{\partial^2 f}{\partial P_j \partial P_k}\bigg|_{P_0} \tag{5–17}$$

Equation (5–15) can be written as vector form by

$$\beta = \alpha \cdot \Delta P \tag{5–18}$$

or

$$\Delta P = \alpha^{-1} \cdot \beta = C \cdot \beta \tag{5–19}$$

The general formulation described above can now be applied to the nonlinear least-squares problem. In this dissertation, the Levenberg-Marquardt and Downhill Simplex methods are applied to fit impedance data.

5.3.3 Regression Strategies for Non-linear Problems

Downhill Simplex method is more forgiving of initial guesses than the Levenberg-Marquardt method. The Levenberg-Marquardt method usually requires an initial guess within an order of magnitude of the target number. In order to get precise numbers, the Downhill Simplex method was applied first then Levenberg-Marquardt method was used.

5.3.3.1 Downhill Simplex Method

The Downhill Simplex method is a commonly applied numerical method used to find the minimum or maximum of an objective function in a multidimensional space.(56) It dose not require evaluation of the derivatives and dose not require the inversion of a matrix that may have zero determinant. This algorithm is based on a simplex; the simplest volume in the N-dimensional parameter area, which is stretched from N+1 points.

For a continuous function $y = f(x_1, \ldots, x_N)$ of N variables $x = \{x_1, \ldots, x_N\}$, the goal is to find a local minimum y_m of this function with corresponding variables x_m. Therefore, a simplex of N+1 points with vectors $x^1, \ldots, x^N, x^{N+1}$, with $x^1 = x^0 + t \cdot e^i$, is constructed.

After having generated the starting simplex, the smallest point $(y_{\min}, x_{\min})$, the biggest point $(y_{\max}, x_{\max})$, and the second-biggest point (y_v, x_v) are determined. The mirror center

$$x^{\mathrm{s}} = \frac{1}{N} \sum_{x^{\mathrm{i}} \neq x^{\max}} x^{\mathrm{i}} \tag{5-20}$$

is determined from all points except the worst point. The next step is to generate a new simplex with lower volume as the reflection of the worst point at the mirror center

$$x^{\mathrm{r}} = x^{\mathrm{s}} - k\left(x^{\max} - x^{\mathrm{s}}\right) \tag{5-21}$$

There are three other methods to construct a new simplex, the expansion to accelerate the reduction of the simplex to one of smaller volume, the contraction to keep the simplex small, and the compression around the actual best point. All four methods are used repeatedly until the best point is obtained.

5.3.3.2 Levenberg-Marquardt Method

The Levenberg-Marquardt method is a compromise between the Gauss-Newton and the Steepest Descent methods.(57) Its critical concepts are the selection of a scaling factor for the method of Steepest Descent and an approach for making a smooth transition from one method to the other. The α from equation (5–18) is replaced by α' such that

$$\alpha'_{\mathrm{jk}} = \alpha_{\mathrm{jk}}(1 + \lambda) \quad \text{for} \quad \mathrm{j} = \mathrm{k} \tag{5-22}$$

$$\alpha'_{\mathrm{jk}} = \alpha_{\mathrm{jk}} \quad \text{for} \quad \mathrm{j} \neq \mathrm{k} \tag{5-23}$$

The equation solved is

$$P_{\mathrm{j,l}+1} = P'_{\mathrm{j,l}} + (\alpha)^{-1} \cdot \beta \tag{5-24}$$

When λ is large, the Levenberg-Marquardt method is close to the method of Steepest Descent. When λ is small, the Levenberg-Marquardt method is close to Gauss-Newton method.
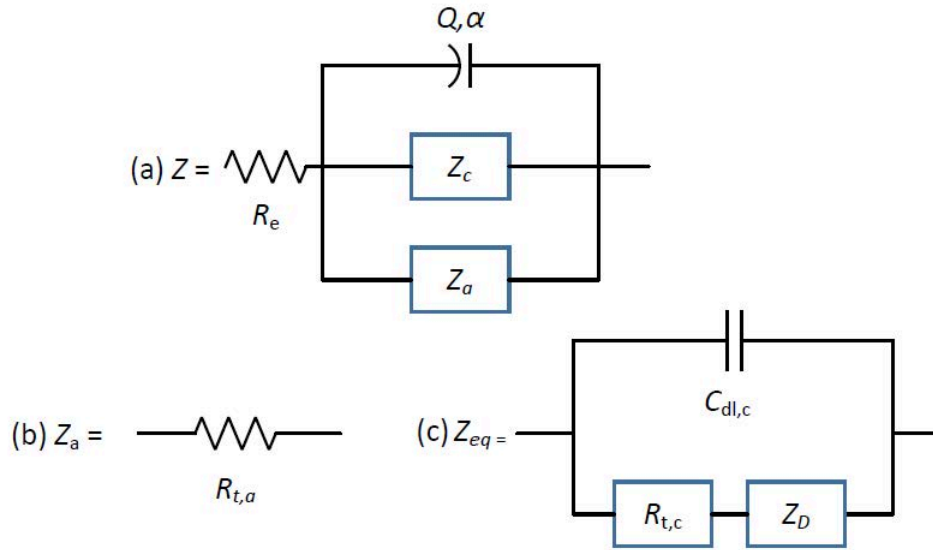
Figure 5-1. Representation of the impedance model for impedance data showing porous electrode behavior: a) the total impedance of the steel/simulated pore solution interface; b) the anodic contribution to the impedance; and c) the interfacial impedance of the microporous layer.

5.4 Process Model Development

Before the steady–state open–circuit potential was reached, the impedance data always showed porous electrode behavior for both No.1 And No.2 ASTM A416 steel. After steady–state open–circuit potential was reached, two different kinds of impedance responses can be observed. For one, the impedance response still showed porous electrode behavior. For another, the porous electrode behavior disappeared. Two different impedance models are required for the two different cases.

5.4.1 Porous Electrode Behavior

At the open–circuit potential, the current from an anodic process (e.g., iron dissolution) must balance the current from the cathodic reaction (e.g., oxygen reduction). Therefore, near the corrosion potential, the total impedance of the system, as shown in Figure 5-1(a), can be regarded to comprise a solution resistance, R_e, in series with a parallel combination of an anodic impedance, Z_a, a cathodic impedance, Z_c, and a capacitance or a constant–phase element, Q, α.(58) The constant–phase element may

account for the variation of time constants in directions normal to or on the surface of an electrode.[59; 60; 61]

For impedances in parallel, such as shown in Figure 5-1(a), cases may be envisioned in which both Z_a and Z_c play a role in the impedance response, in which $Z_a \gg Z_c$ and only Z_c plays a role in the impedance response, and in which $Z_a \ll Z_c$ and only Z_a plays a role in the impedance response. These cases may be differentiated by measuring the impedance at open circuit and at potentials shifted slightly from the open–circuit value. Again, care is needed to assure a steady–state value. The resulting impedance values, presented in Figure 5-2 with applied potential as a parameter, show that the impedance decreased slightly from the open–circuit values at both -0.13 V(Hg/HgO) and -0.03 V(Hg/HgO). These results suggest that both anodic and cathodic impedances must be included in the model.

Under the assumption that the anodic reaction follows Tafel kinetics, the anodic impedance, Z_a, may be expressed as a charge-transfer resistance, $R_{t,a}$, as shown in Figure 5-1(b). The cathodic branch is based on a porous electrode model, which has an impedance distributed in space as a transmission line in a conducting macropore, as shown in Figure 5-3. This transmission line is composed of the elementary elements $R_0 \Delta x$ and $Z_0/\Delta x$, where R_0 is the ohmic drop resistance for a unit length macropore (with units of Ωcm^{-1}), Δx is the thickness of an infinitesimal slice of the macropore and Z_0 is the interfacial impedance for a unit length macropore (with units of Ωcm).

As shown in Figure 5-1(c), the interfacial impedance per unit area Z_{eq} is composed of a parallel arrangement of the cathodic double layer capacitance, $C_{dl,c}$ and the Faradaic branch consisting of a cathodic charge transfer resistance, $R_{t,c}$ in series with a diffusion impedance Z_D. The term, Z_D, which describes the radial diffusion in the macropores, is given by Drossbach and Schulz[62] to be

$$Z_D = R_D \frac{\tanh(\sqrt{j\omega \frac{\delta_r^2}{D_r}})}{\sqrt{j\omega \frac{\delta_r^2}{D_r}}} \tag{5–25}$$
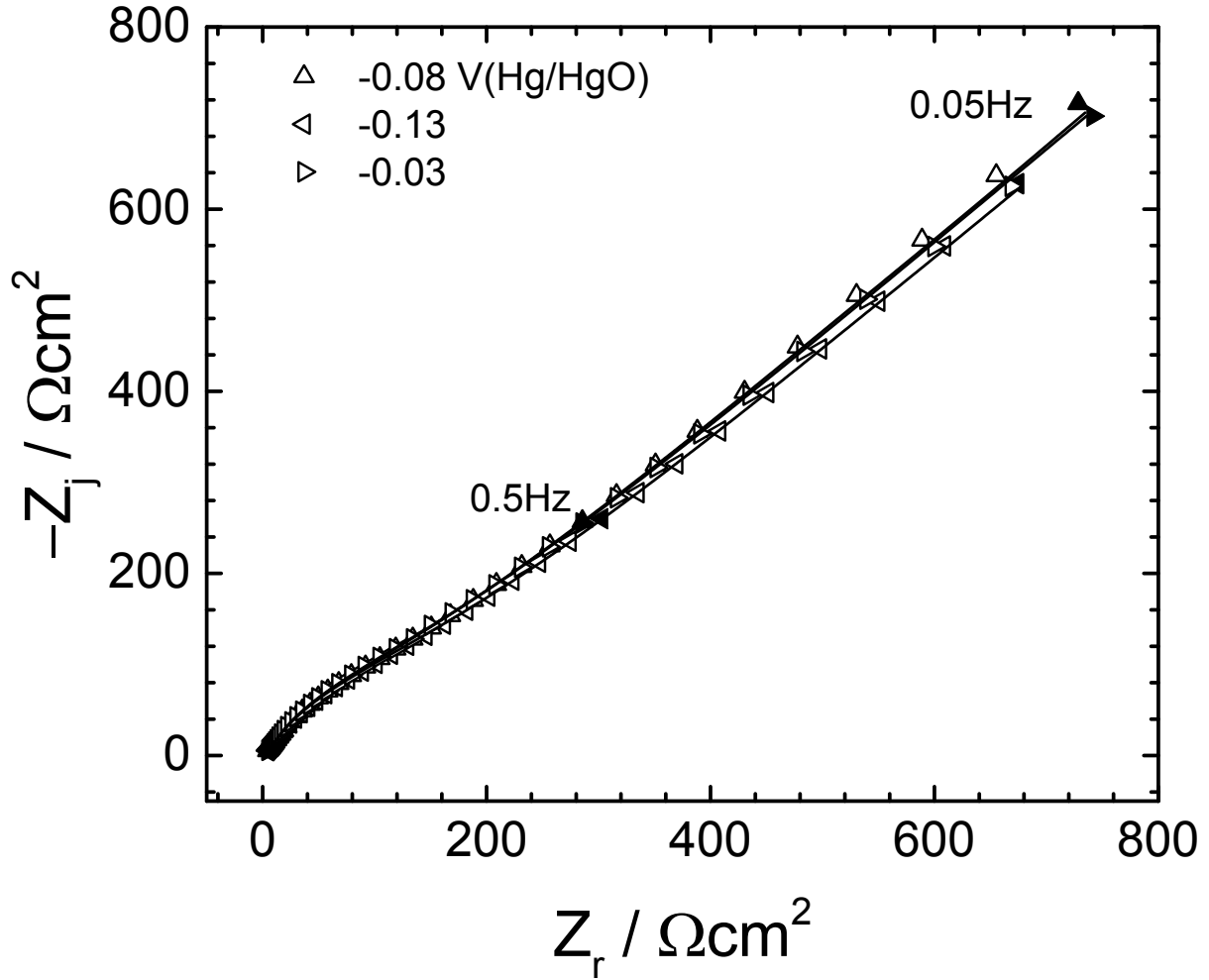
Figure 5-2. Impedance measurement at the corrosion potential (-0.08 V(Hg/HgO)),
-50 mV (-0.13 V(Hg/HgO) and +50mV (-0.03 V(Hg/HgO) from corrosion
potential. The lines represent the regression of equation (5–38) to the data.

where R_D is the diffusion resistance (Ω), δ_r is the thickness of the diffusion layer (cm) and D_r is the diffusivity of dissolved oxygen in the pore (cm^{2}s^{-1}).

The cathodic impedance has the general form

$$Z_c = \sqrt{R_0 Z_0} \coth\left(\frac{L}{\lambda}\right) \tag{5–26}$$

where L is the mean length of the macropores and

$$\lambda = \sqrt{\frac{Z_0}{R_0}} \tag{5–27}$$
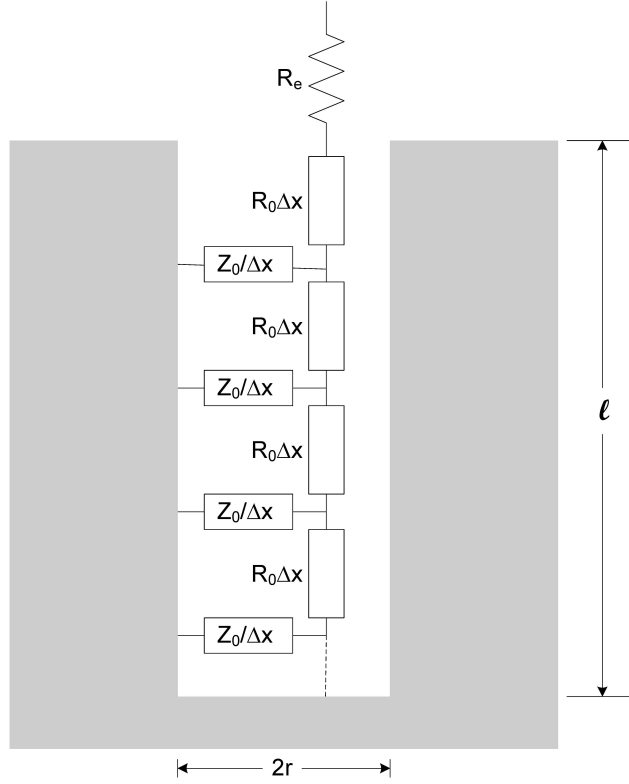
Figure 5-3. Schematic representation of a porous electrode including a transmission line inside a cylindrical pore. Taken from Orazem and Tribollet.[54]

is the penetration depth of the electrical signal. The specific impedances R_0 and Z_0 can be expressed as functions of the pore radius as

$$R_0 = \frac{\rho}{\pi r^2} \tag{5–28}$$

and

$$Z_0 = \frac{Z_{\mathrm{eq}}}{2\pi r} \tag{5–29}$$

respectively, where ρ is the electrolyte resistance, with units of Ωcm, and r is the pore radius in units of cm. Equation (5–26) can therefore be expressed as

$$Z_c = \frac{\rho Z_{eq}}{\sqrt{2}\pi n r^{3/2}} \coth\left(L\sqrt{\frac{2\rho}{rZ_{eq}}}\right) \tag{5–30}$$

Equation (5–30) may be expressed in terms of lumped parameters as

$$Z_c = A_1\sqrt{Z_1}\coth\left(\frac{A_2}{\sqrt{Z_1}}\right) \tag{5–31}$$

where

$$Z_1 = \frac{(1+A_3\left(\dfrac{\tanh\sqrt{j\omega A_4}}{\sqrt{j\omega A_4}}\right)}{1+j\omega A_5\left(1+A_3\left(\dfrac{\tanh\sqrt{j\omega A_4}}{\sqrt{j\omega A_4}}\right)\right)} \tag{5–32}$$

represents the interfacial impedance on the wall of porous electrode. Other lumped parameters can be defined as

$$A_1 = \left(\frac{R_0 R_{t,c}}{2\pi n^2 r}\right)^{0.5} \tag{5–33}$$

$$A_2 = L\sqrt{\frac{2\pi r R_0}{R_{t,c}}} \tag{5–34}$$

$$A_3 = \frac{R_D}{R_{t,c}} \tag{5–35}$$

$$A_4 = \frac{\delta_r^2}{D_r} \tag{5–36}$$

and

$$A_5 = C_{c,dl}R_{t,c} \tag{5–37}$$

where A_4 represents the time constant for diffusion in the porous electrode, and A_5 represents the time constant for the cathodic reaction on the porous electrode wall.

The total impedance Z may be regarded to be

$$Z = R_e + \left(\frac{R_{t,a} + Z_c}{R_{t,a}Z_c} + (j\omega)^\alpha Q\right)^{-1} \tag{5–38}$$
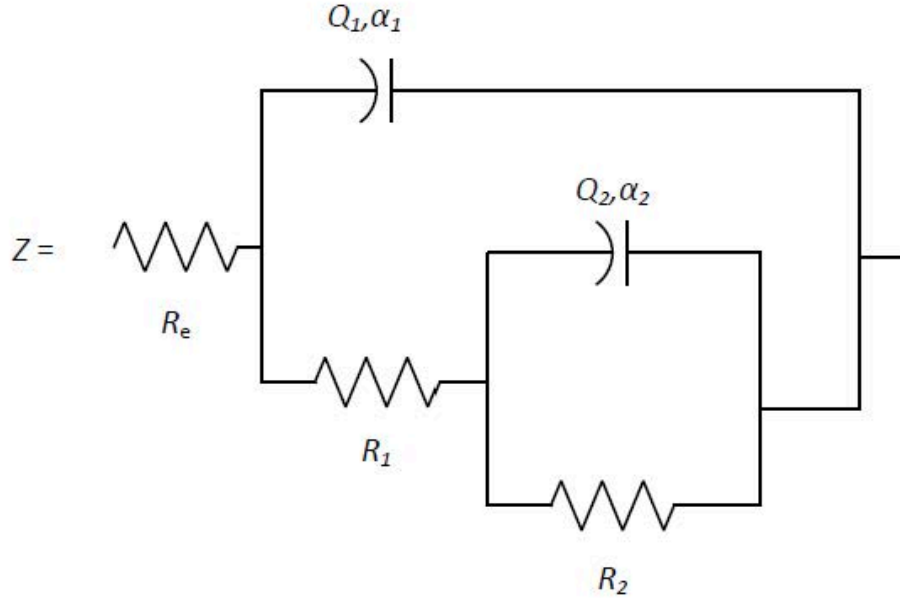
Figure 5-4. Schematic representation of the impedance model for the low–frequency impedance data has a degree larger than 45°.

When $R_{\mathrm{t,a}} \gg Z_{\mathrm{c}}$, the value of $R_{\mathrm{t,a}}$ cannot be extracted by the regression procedure. In this case, equation (5–38) can be written as

$$Z = R_{\mathrm{e}} + (Z_{\mathrm{c}} + (j\omega)^{\alpha}Q)^{-1} \tag{5–39}$$

As the role of the constant–phase element is diminished in the low–frequency limit, the low–frequency impedance for a system in which the corrosion rate is negligible shows a straight line in the Nyquist representation.

5.4.2 Model for Reaction at Bottom of Pores in Dielectric Layer

When the low–frequency impedance data has a degree larger than 45°, the model for reaction at bottom of pores in dielectric layer, shown in Figure 5-4 can be used. The mathematical model for the total impedance in this case can be expressed as

$$Z_{\mathrm{HDE}} = R_{\mathrm{e}} + \left(\left(R_1 + \frac{R_{\mathrm{t}}}{1 + (j\omega)^{\alpha_2}Q_2 R_{\mathrm{t}}} \right)^{-1} + \left(\frac{1}{(j\omega)^{\alpha_1}Q_1} \right)^{-1} \right)^{-1} \tag{5–40}$$

63
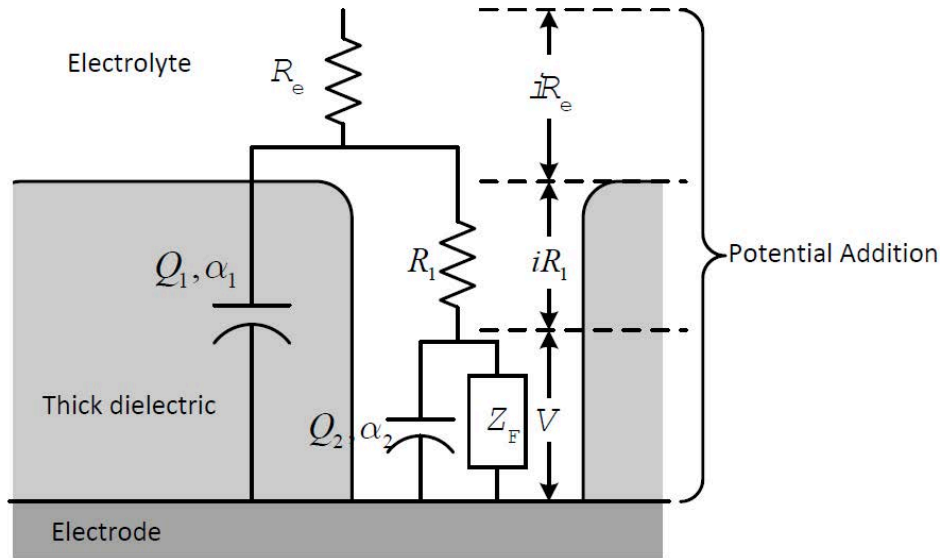
Figure 5-5. Physical interpretation of the impedance for an electrode coated by a thick dielectric layer with pores exposing the electrode to the electrolyte.

This circuit was used by Joiret et al. (24) for a stationary iron electrode in 1M NaOH. Although the corresponding HAADF-STEM images shown in Figure 7-9 A and B suggest the oxide film covers the entire ASTM A416 steel uniformly. There are considerable experiments indicating that water still exists in passive oxide films.(63; 64) The physical interpretation equivalent circuit shown in Figure 5-4 can be expressed as the electrode coated with an inert porous layer, shown in Figure 5-5. Within the pore length, the electrolyte resistance is R_1, and the insulating part of the coating can be considered to be a a constant-phase element, with parameters Q_1 and α_1, under the assumption that the film has a distribution of resistivity normal to the electrode surface, which is in parallel with the impedance in the pore. The parallel combination of Q_2 and Z_F are associated to a redox process in the passive layer between magnetite and iron(III) oxides.(65) Z_F is supposed to consist of a parallel combination of an anodic impedance, Z_a, and a cathodic impedance, Z_c. However, based on the impedance data shown in Figure 4-18 and 4-20, the only visible impedance is cathodic impedance, Z_c. Therefore, Z_F can be regarded as a

resistor, R_2 in Figure 5-4, stands for the cathodic charge transfer resistance of reduction process in the passive layer.

The constant-phase element (CPE) plays an important role for all the process model developed in this dissertation due to the property of iron oxide film in high pH solutions. Recently, a two-layered passive film that consisted with an inner layer formed by mixed iron oxide, Fe_3O_4, and an Fe^{3+} outer layer was considered by Gunay et al. .(27) Since the chemical composition of iron oxide film in high pH solutions is varied normal to the surface of electrode, the impedance response of inner layer can be expected to be different from outer layer. Therefore, a simple capacitor is not sufficient to interpret the impedance response of oxide films formed on ASTM A416 steel in highly alkaline solution. The origin of the CPE and how the varied oxide film composition can attribute to CPE behavior are discussed in Chapter 6.

CHAPTER 6
FILM RESISTIVITY DISTRIBUTION

The physical origins of the constant-phase element (CPE) are controversial. CPE parameters are considered to arise from a distribution of time-constants. The time-constants may be distributed along the surface of an electrode or in the direction normal to the electrode.(59) Distributions of time-constants may result from distributions of physical properties including structure, reactivity, dielectric constants, and resistivity.

6.1   Constant-Phase Element

The CPE impedance is expressed in terms of model parameters α and Q as

$$Z_{\text{CPE}} = \frac{1}{(j\omega)^\alpha Q} \tag{6--1}$$

Equation (6–1) is representative of a blocking system with an infinite low-frequency impedance. When $\alpha = 1$ the system is described by a single time-constant and the parameter Q has units of capacitance; otherwise, Q has units of $F/s^{1-\alpha}cm^2$.

The following analysis is based on the work of Hirschorn et al.(29; 28) The resistivity distribution can be derived from the Voigt element parameters, τ_i and R_i. The corresponding impedance is expressed as

$$Z_{\text{RC}} = \sum_i \frac{R_i}{1 + j\omega\tau_i} \tag{6--2}$$

where each Voigt element represents the time constant and resistivity for a given differential element. Each RC–time constants is assumed to be associated with a differential layer of the film.

The differential capacitance derived as

$$C_i = \tau_i/R_i \tag{6--3}$$

is a function of dielectric constant and the thickness of the element. The corresponding thickness of each element i, d_i, is related to the local dielectric constant ε_i by

$$d_i = \frac{\varepsilon_i \varepsilon_0}{C_i} \tag{6--4}$$

where $\varepsilon_0 = 8.8542 \times 10^{-14}$ F/cm is the permittivity of vacuum. The local resistance can also be related to thickness of element i by

$$R_i = \rho_i d_i \qquad (6\text{--}5)$$

Therefore, the time constant τ_i is independent of element thickness and can be expressed as

$$\tau_i = \rho_i \varepsilon_i \varepsilon_0 \qquad (6\text{--}6)$$

Under the assumption that dielectric constant is uniform, the variability of capacitance could be the consequence of a changing element thickness. Based on equation (6–5) and (6–6), the resistivity, R_i, could also be related to time constant by

$$\rho_i = \frac{R_i}{d_i} = \frac{\tau_i}{\varepsilon \varepsilon_0} \qquad (6\text{--}7)$$

The elements with smallest and largest resistivity values were assumed to be located at the interface of the system, and the resistivity of elements in the system was assumed to increase or decrease monotonically. Thus, if the thickness of the element with the smallest resistivity value is d_1 and the element with the second smallest resistivity value is d_2, the specific position of element with second smallest resistivity value in the system is $d_1 + d_2$. The specific position of other elements in systems can be calculated in the same manner.

Synthetic impedance data were created based on equation (6–1) with addition of random normally distributed stochastic noise with a standard deviation equal to 0.2 percent of the modulus of the impedance. The parameter Q was assigned a value $Q = 1 \times 10^{-6}$ F/s$^{1-\alpha}$cm^2. The real part and imaginary parts of the synthetic impedance were obtained from

$$Z_{r,\text{noise}} = Z_r + 0.002\,|Z|\,p\,(0,1) \qquad (6\text{--}8)$$

and

$$Z_{j,\text{noise}} = Z_j + 0.002\,|Z|\,p\,(0,1) \qquad (6\text{--}9)$$
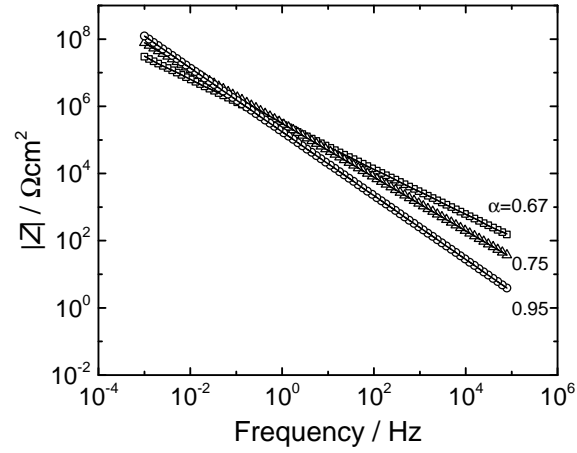
A
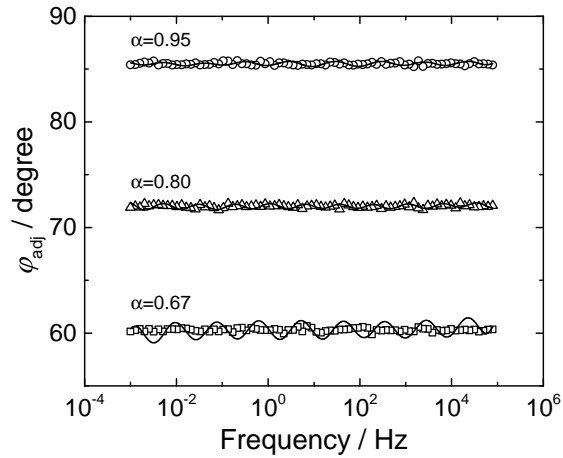
B

Figure 6-1. Synthetic impedance spectra calculated from equations (6–1), (6–8), and (6–9) with $Q = 1 \times 10^{-6}$ F/s$^{1-\alpha}$cm^2 and α as a parameter: A) magnitude of impedance and B) ohmic–resistance–corrected phase angle calculated from equation (6–10). The lines represent the measurement model fit.

respectively, where $|Z|$ is the magnitude of the impedance and $p(0,1)$ is the probability density function with mean equal to zero and with standard deviation equal to unity. The exponent α was treated as a parameter with values of 0.67, 0.8 and 0.95. The magnitude of the impedance and the ohmic-resistance-corrected phase angle are presented in Figures 6-1A and 6-1B, respectively. The lines in these figures represent the fit of the

measurement model given as equation (6–2). The adjusted phase angle shown in Figure 6-1B can be expressed as

$$\varphi = \tan^{-1}\left(\frac{Z_{\mathrm{j}}}{Z_{\mathrm{r}} - R_{\mathrm{e}}}\right) \tag{6–10}$$

where Z_{r} is the real part of the impedance, Z_{j} is the imaginary part of the impedance, and R_{e} is the ohmic resistance. In the present case, the ohmic resistance was assigned a value of zero; thus, the phase angle calculated from equation (6–10) was equivalent to the usual phase angle.

The error structure model employed, in which the standard deviation of the impedance is given as $\sigma = 0.002\,|Z|$, is in agreement with the error structures obtained under potentiometric modulation.(46; 66) The results presented in Figure 6-1A suggest that addition of the random noise does not have visible effects on the impedance data. Figure 6-1B suggests that the ohmic–resistance–corrected phase angle is more sensitive to the added noise, but the effects are small.

Hirschorn et al.(28) observed that the resistivity distribution corresponding to a CPE follows a power law, e.g.,

$$\frac{\rho}{\rho_\delta} = \xi^{-\gamma} \tag{6–11}$$

where γ is related to α such that

$$\alpha = \frac{\gamma - 1}{\gamma} \tag{6–12}$$

$\xi = x/\delta$, and δ is the thickness of the film. The value of film thickness was obtained from the regressed measurement model parameters following

$$\delta = \sum_{i=0}^{n} d_{\mathrm{i}} \tag{6–13}$$

The position variable x corresponding to element k was obtained from

$$x_{\mathrm{k}} = \sum_{i=0}^{k} d_{\mathrm{i}} \tag{6–14}$$

The parameter ρ_δ is the resistivity at $\xi = 1$ or $x = \delta$.
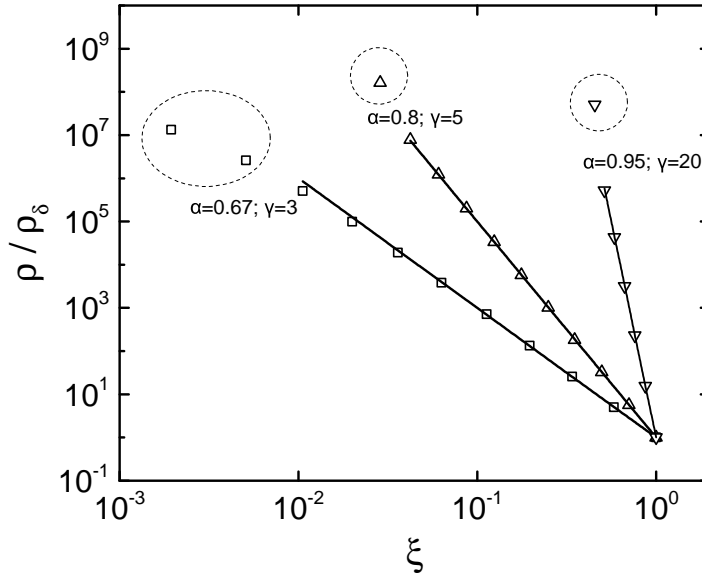
Figure 6-2. Resistivity corresponding to the synthetic data presented in Figure 6-1 scaled by ρ_δ and presented as a function of dimensionless position. Symbols are the discrete resistivity values calculated from equation (6–6) using the regressed values of τ_i and under the assumption that $\varepsilon = 12$. The lines represent the expected resistivity distribution and the circled values were not used in the subsequent analysis.

The resistivity distribution developed from the measurement model analysis is presented in Figure 6-2 for the synthetic CPE data shown in Figure 6-1. A value of ρ_δ cannot be obtained from CPE data; thus, the measurement model analysis provides only the expected value for the exponent in the power–law distribution. Due to bias associated with the beginning and end of the impedance spectrum, the regressed measurement model parameters corresponding to the highest and lowest time constant were not included in the estimate of the resistivity distribution. These results are in agreement with the analysis presented by Hirschorn et al.(28) for the CPE.

The input values of γ corresponding to equation (6–12) and the regressed values are shown in Table 6-1. These results show good agreement between input and output values of γ.

Table 6-1. Results of the measurement model analysis of the synthetic CPE model data.

γ input	3	5	20
γ regressed	2.86	5.02	19.82

6.2 Synthetic Power–Law Model Data

Hirschorn et al.(28) proposed a distribution of resistivity that provided a bounded value for resistivity to be

$$\frac{\rho}{\rho_\delta} = \left(\frac{\rho_\delta}{\rho_0} + \left(1 - \frac{\rho_\delta}{\rho_0}\right)\xi^\gamma\right)^{-1} \tag{6–15}$$

where ρ_0 and ρ_δ are the boundary values of resistivity at the interfaces and $\xi = x/\delta$. Under assumption that the dielectric constant is uniform, the impedance of the film can be written for an arbitrary resistivity distribution $\rho(x)$ as

$$Z_f(\omega) = \int_0^{\delta_f} \frac{\rho(x)}{1 + j\omega\varepsilon\varepsilon_0\rho(x)}\,\mathrm{d}x \tag{6–16}$$

Following equation (6–15), a general expression of impedance function can be expressed as

$$Z_f(\omega) = g\frac{\delta\rho_\delta^{1/\gamma}}{\left(\rho_0^{-1} + j\omega\varepsilon\varepsilon_0\right)^{(\gamma-1)/\gamma}} \tag{6–17}$$

where

$$g = 1 + 2.88\gamma^{-2.375} \tag{6–18}$$

Equation (6–17) is in the form of a CPE if $\omega > (\rho_0\varepsilon\varepsilon_0)^{-1}$, i.e.,

$$Z_f(\omega) = g\frac{\delta\rho_\delta^{1/\gamma}}{\left(j\omega\varepsilon\varepsilon_0\right)^{(\gamma-1)/\gamma}} = \frac{1}{(j\omega)^\alpha Q} \tag{6–19}$$

Therefore, equation (6–17) has CPE behavior for $(\rho_0\varepsilon\varepsilon_0)^{-1} < \omega < (\rho_\delta\varepsilon\varepsilon_0)^{-1}$.

Synthetic data were generated using equation (6–17) for different values of ρ_0 and γ. The dielectric constant was given a value of 10, the film thickness $\delta = 100nm$, and the term ρ_δ was assigned a value of 100 Ωcm. The corresponding characteristic frequency was

$$f_\delta = \frac{1}{2\pi\rho_\delta\epsilon\epsilon_0} = 1.8 \text{ GHz} \tag{6–20}$$
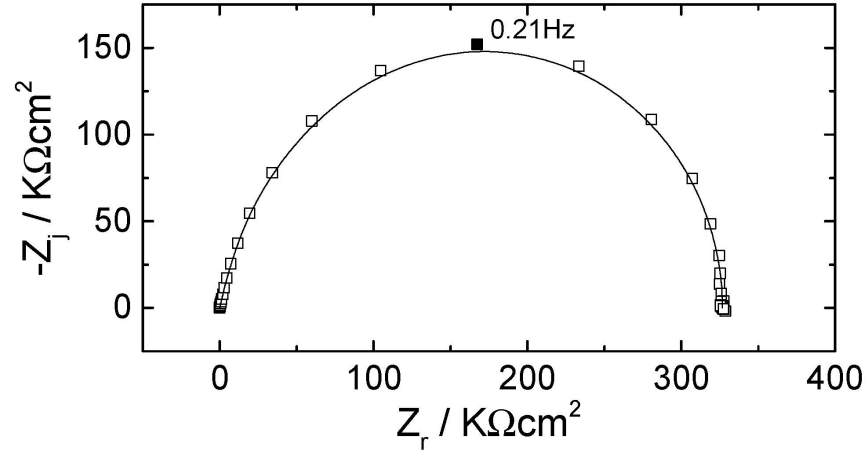
Figure 6-3. Nyquist representation of the impedance by equation (6–17) with $\rho_0 = 10^{12}\Omega cm$, $\rho_\delta = 100\Omega cm$, $\varepsilon = 10$, $\delta = 100nm$ and and $\gamma = 6.67$ as parameters. The line represent the regression of equation (6–2) to the data.

which was outside the frequency range of the synthetic data. Noise was added following the protocol expressed as equations (6–8) and (6–9). Regressed values for measurement model parameters were used to generate resistivity distributions which were in term regressed by equation (6–11) to obtain values of γ.

If the ρ_0 in equation (6–17) has a value close to $(\omega\varepsilon\varepsilon_0)^{-1}$, both terms in denominator of equation (6–17) cannot be neglected. A example of Nyquist representation of the impedance based on 6–17 with 0.2 percent of normal random distribution noise is given in Figure 6-3. The characteristic frequency corresponding to ρ_0 for Figure 6-3 is given as

$$f_0 = \frac{1}{(2\pi\rho_0\varepsilon\varepsilon_0)} = 0.18 \text{ Hz} \tag{6–21}$$

This value is very close to the highlighted data point in Figure 6-3.

The magnitude of the synthetic impedance data and the ohmic-resistance-corrected phase angle obtained from (6–17) are presented in Figure 6-4A and 6-4B, respectively, with ρ_0 as a parameter. The added noise is barely visible in Figures 6-4A and 6-4B.

The resistivity distribution functions for the synthetic impedance presented in Figure 6-4A are shown in Figure 6-5. The resistivity in Figure 6-5 is nondimensionalized by ρ_0, instead of ρ_δ, used in Figure 6-2. The values of points in the red circle of Figure 6-5 all
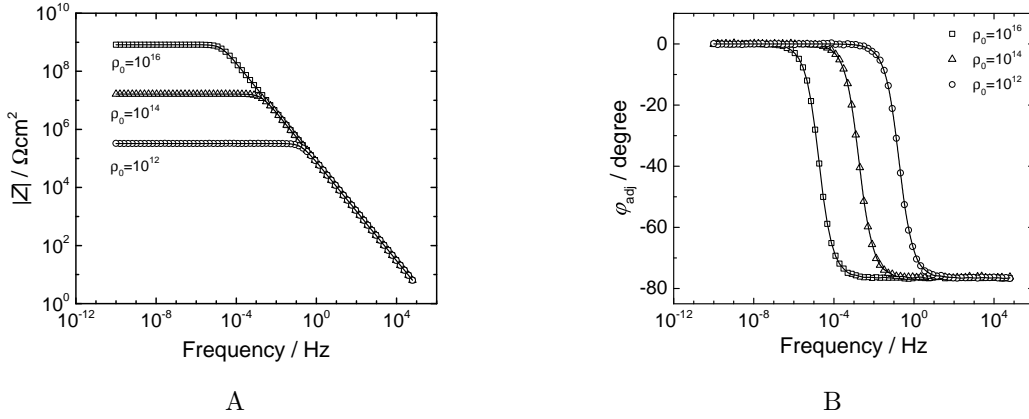
Figure 6-4. Synthetic impedance data obtained from (6–17) with $\rho_\delta = 100\Omega\text{cm}$, $\varepsilon = 10$, $\delta = 100\text{nm}$, $\gamma = 6.67$, and ρ_0 as a parameter: A) magnitude of impedance and B) ohmic–resistance corrected phase angle. The lines represent the regression of equation (6–2) to the data.
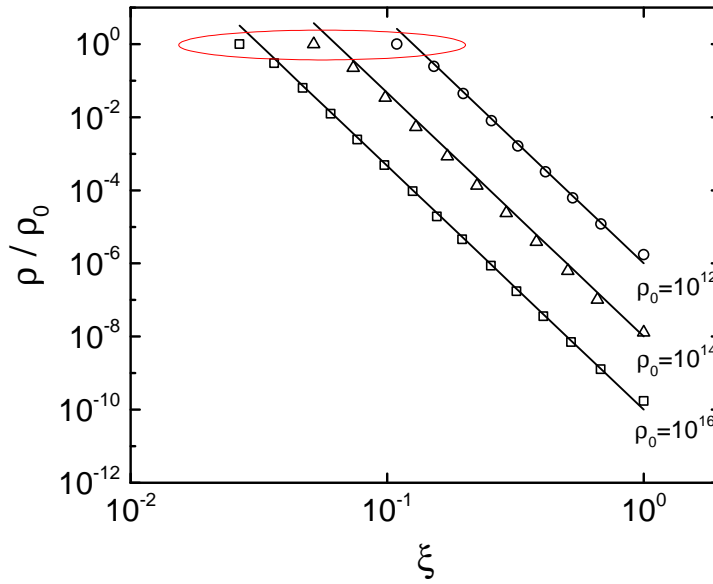
Figure 6-5. Dimensionless resistivity distribution as a function of dimensionless position for synthetic impedance data in Figure (6-4). The symbols are the discrete resistivity values calculated from equation (6–6) using the regressed values of τ_i and $\varepsilon = 10$. The circled values are close to unity, suggesting that the measurement model provide a good estimate for ρ_0.

Table 6-2. Results of the measurement model analysis of the synthetic power–law model data.

γ input	6.67	6.67	6.67
γ regressed	6.11	6.58	6.50
ρ_0 input, Ωcm	1×10^{16}	1×10^{14}	1×10^{12}
ρ_0 regressed, Ωcm	7.8×10^{15}	7.70×10^{13}	7.70×10^{11}

very close to 1, suggesting that the largest resistivity values obtained from (6–17) are very close to ρ_0. The input values and the regressed values of γ and ρ_0 are shown in Table 6-2. These results show good agreement between input and output values of γ. The regressed values of ρ_0 is in rough agreement with input values. Extraction of values for $\rho_0 > 10^{12}$ was possible only for frequencies that are much smaller than generally measured. The results presented here are used solely to demonstrate the utility of the measurement model approach to extract parameters consistent with input values.

6.2.1 Synthetic Young Impedance Data

The impedance proposed by Young(67; 68) can be expressed as

$$Z_{\mathrm{Y}} = -\frac{\lambda}{\mathrm{j}\omega\varepsilon_0\varepsilon} \ln\left(\frac{1 + \mathrm{j}\omega\varepsilon_0\varepsilon\rho_0 e^{-\delta/\lambda}}{1 + \mathrm{j}\omega\varepsilon_0\varepsilon\rho_0}\right) \tag{6–22}$$

based on exponential variation of resistivity that can be expressed as

$$\rho(x) = \rho_0 \exp\left(-\frac{x}{\lambda}\right) \tag{6–23}$$

This type of resistivity distribution has been seen in epoxy-polyaminoamide waterborne paint.(69) Nguyen et al. suggested that a single time constant attributed to the dielectric properties of the coating in dry condition, and is very close to an ideal capacitive behavior. For the longer immersion times ($t \geq 48$ h) in NaCl solutions, the coating showed Young impedance behavior.

The synthetic Young impedance data calculated following equation (6–22) with 0.2 percent of normally random distributed noise and with δ/λ and ρ_0 as independent parameters are presented in Figure 6-6 As shown in Figure 6-6A and 6-6B, the added

74
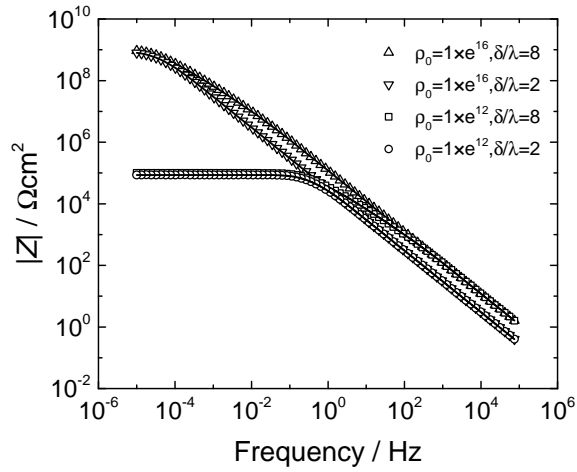
A
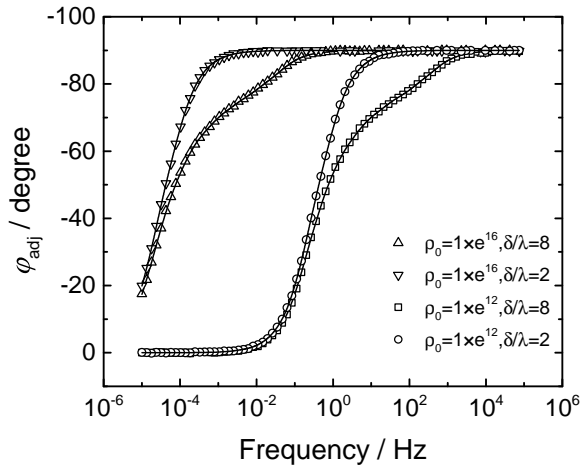
B

Figure 6-6. Synthetic Young impedance data calculated following equation (6–22) with 0.2 percent of normally random distributed noise and with δ/λ and ρ_0 as independent parameters: A) magnitude of impedance and B) ohmic–resistance corrected phase angle. The lines represent the regression of equation (6–2) to the data.
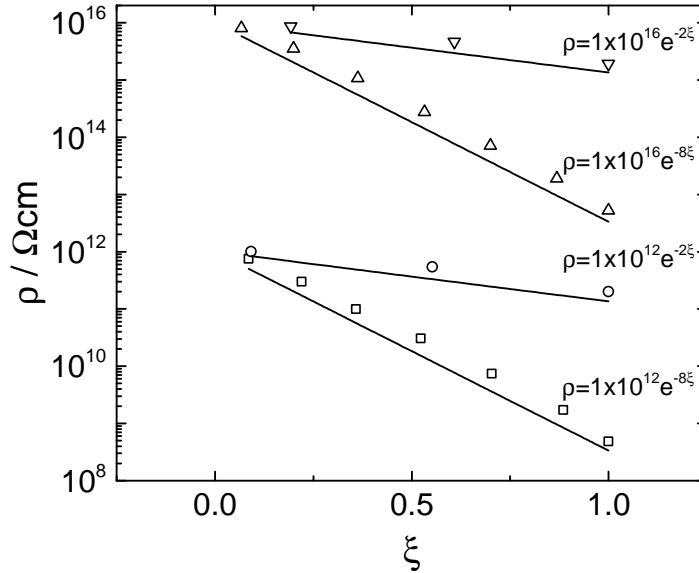
Figure 6-7. Resistivity as a function of dimensionless position. The symbols are the discrete resistivity values calculated from equation (6–6) using the regressed values of τ_i and $\varepsilon = 4.5$.

noise did not have visible effect on both magnitude and phase angle of synthetic Young impedance data.

Similar to the results for a constant-phase element, the resistivity distribution for synthetic Young impedance data is shown in Figure 6-7 as function of dimensionless position, ξ, with ρ_0 and δ/λ as parameters. A smaller number of Voigt elements were needed to fit synthetic Young impedance data with small value of δ/λ. For $\delta/\lambda = 8$, 7 Voigt elements were needed; whereas, for $\delta/\lambda = 2$ only three Voigt elements could be obtained.

The input values and the regressed values of ρ_0 and δ/λ are shown in Table 6-3, these results suggested that values obtained from measurement model analysis are very close to original values.

The major discrepancy between model and data is due to the variation of ρ_0. Therefore, ρ/ρ_0 was plotted as function of dimensionless position, as shown in Figure

Table 6-3. Input values and regressed values for measurement model analysis of synthetic impedance data based on the the Young model.

ρ_0		δ/λ	
input	regressed	input	regressed
1×10^{16}	1.3×10^{16}	8	6.5
1×10^{16}	1.2×10^{16}	2	1.7
1×10^{12}	1.4×10^{12}	8	7.1
1×10^{12}	1.2×10^{12}	2	1.5
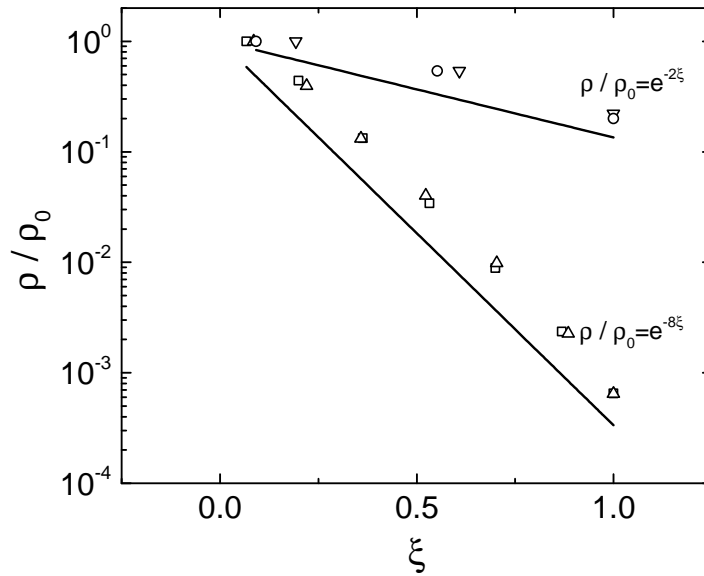
Figure 6-8. Dimensionless resistivity as a function of dimensionless position. The symbols are the discrete resistivity values calculated from equation (6–6) using the regressed values of τ_i and $\varepsilon = 4.5$.

6-8. This work suggests that impedance data with different values of ρ_0 but with the same δ/λ can have very similar dimensionless resistivity distributions.

6.2.2   Experimental Impedance Data for Coated Aluminum

The analysis discussed above was also be applied to impedance data for coating samples, collected by Nguyen et al.(69) The magnitude of impedance and phase angle of impedance responses for aged and as-prepared CC coating on 2024 aluminium alloy are presented in Figure 6-9. The coating was a two-component water-based paint used as an anticorrosive primer. The base was a polyaminoamide (Versamid type) and the
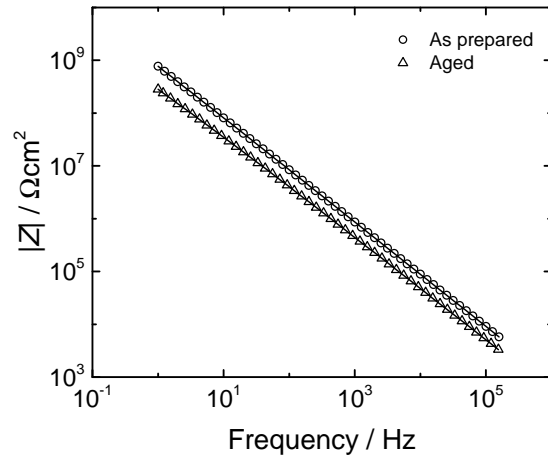
A
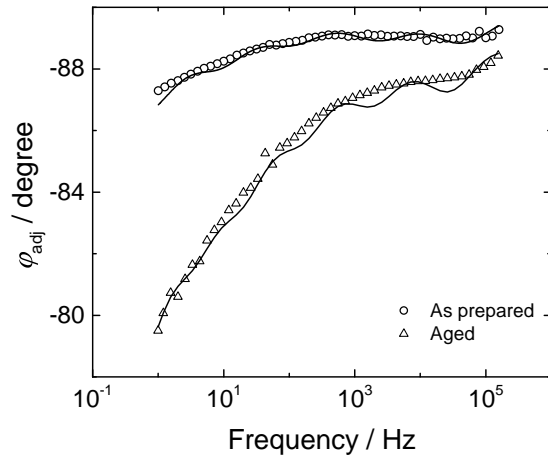
B

Figure 6-9. Measured impedance response for the as prepared and aged CC coating: A) magnitude of the impedance and B) the ohmic–resistance corrected phase angle. The line represent the regression of equation (6–2) to the data.

hardener was a bisphenol A epoxy polymer. The coatings were manufactured by Mapaero SAS. Different pigments were added to the organic matrix: titanium oxide (12 wt.%), talc (11 wt.%), silica (1 wt.%) and strontium chromate (16 wt.%). The ratio of the pigment volume concentration (PVC) to critical pigment volume concentration (CPVC) was equal to 0.61. The CPVC is the pigment concentration at which there is just enough binder in

the dry coating to completely fill all the voids between the pigment particles. The PVC to CPVC ratio is an important parameter which controls the film barrier properties.

In the present work, a comparison is provided for the impedance behavior of two waterborne coatings with different pigments in their formulation. One of them (henceforth denoted CC) contained $SrCrO_4$. The other coating (henceforth denoted NCC) contained a mixture of pigments, replacing $SrCrO_4$. Impedance measurements in the conventional metal/coating/electrolyte configuration were performed in a classical three-electrode cell, realized by fixing a cylindrical Plexiglas tube on top of the coated sample, and filled with a 0.5 M NaCl solution. The working electrode was a 24 cm^2 portion of the sample. An SCE and a Pt sheet were used as reference and counter electrode, respectively.[70]

The impedance response for aged and as-prepared CC and NCC coating on 2024 aluminium alloy are presented in Figures 6-9 and 6-10, respectively. For both as-prepared NCC and CC samples, the impedance was close, but not identical, to that of an ideal capacitor. After ageing, the impedance of the NCC was qualitatively similar to that of the as-prepared sample, though with a decrease in modulus, and still very close to a CPE behavior, suggesting that the physical properties of this coating were little affected by the prolonged immersion in NaCl solution, once the NCC was allowed to dry. Due to the quasi-constancy of the phase angle shows in Figure 6-9B and 6-10B over a five-decade frequency range and with a value close to 88°, both NCC and CC as-prepared coating may be mistakenly assumed to satisfy constant-phase element behavior with α close to 0.95. The impedance of the CC underwent significant alteration upon ageing, proving that its properties were severely and irreversibly affected by immersion in 0.5M NaCl solution, most probably due to extensive dissolution of $SrCrO_4$. Loss of part of this chemical, initially present in a 16 wt.% amount in the coating, probably left voids in the polymer matrix, which were filled by the electrolytic solution during immersion. Although most water was removed during drying, some conductive phase may have remained within the
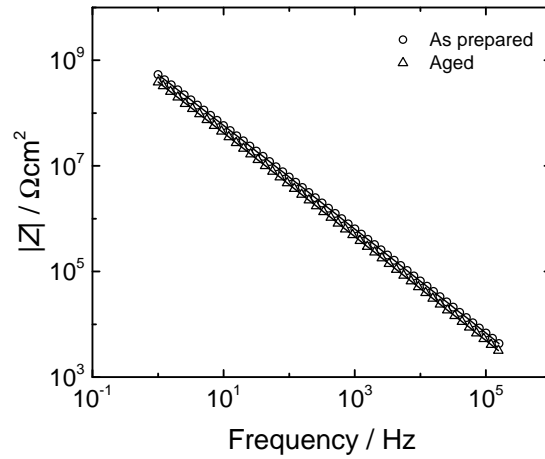
A
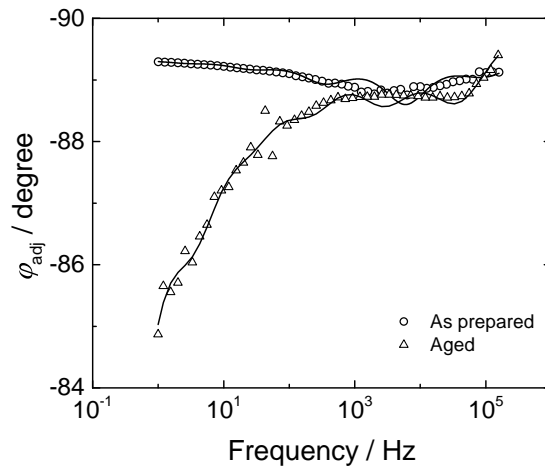
B

Figure 6-10. Measured impedance response for the as prepared and aged NCC coating: A) magnitude of the impedance and B) the ohmic–resistance corrected phase angle. The line represent the regression of equation (6–2) to the data.

aged CC, causing a marked departure from the CPE behavior of the as-prepared CC and an impedance decrease more evident than for NCC.

The measurement model was fit to the data presented in Figures 6-9 and 6-10, and the analysis described in equation (6–4) to (6–7) was used to identify the corresponding resistivity distribution. The dielectric constant was assumed to be uniform with a value of $\varepsilon = 4.9$ for CC coating and $\varepsilon = 6.1$ for NCC coating as suggested by Nguyen et
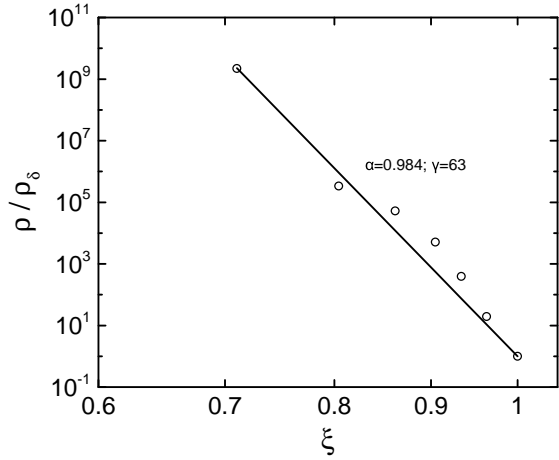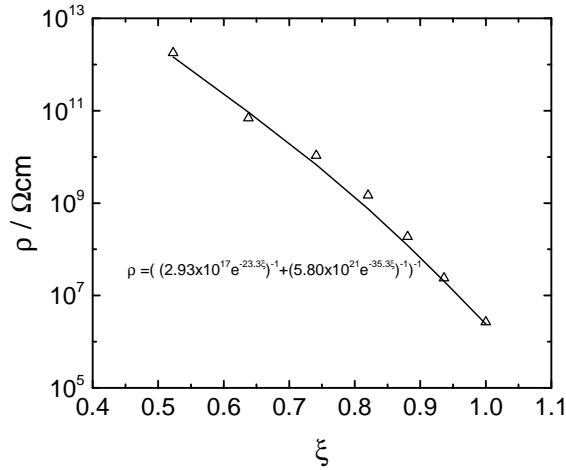
Figure 6-11. Resistivity as a function of dimensionless position: A) as prepared and B) aged CC coating. The symbols are the discrete resistivity values calculated from equation (6–6) using the regressed values of τ_i and $\varepsilon = 4.9$.

al.(69) The resulting resistivity distribution, presented in Figures 6-11 and 6-12 as functions of dimensionless position, ξ. Figure 6-11A suggests that the as-prepared CC coating followed the CPE behavior while the other cases are more consistent with a Young model, characterized by an exponential distribution of resistivity. In the case of aged CC coating, presented in Figure 6-11B, a model is proposed in which the resistivity follows an
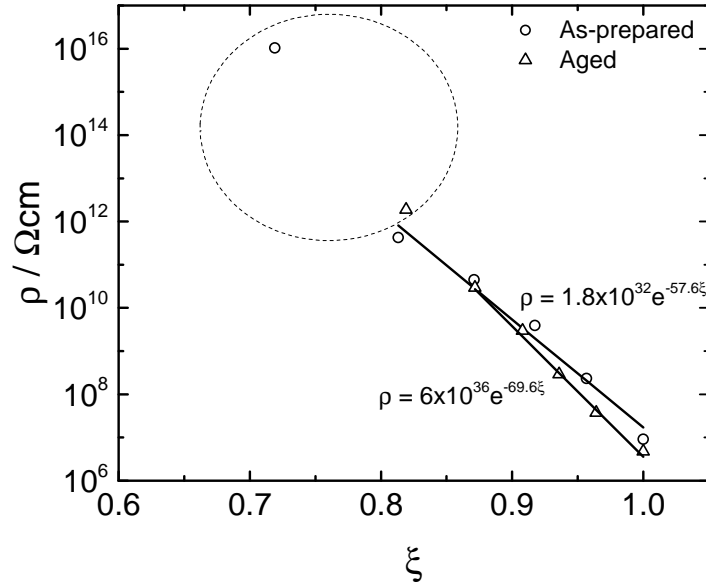
Figure 6-12. Resistivity as a function of dimensionless position for as prepared and aged NCC coating. The symbols are the discrete resistivity values calculated from equation (6–6) using the regressed values of τ_i and $\varepsilon = 6.1$ and the circled values were not used in the subsequent analysis.

interpolation formula given as

$$\rho = \left(\frac{1}{2.93 \times 10^{17} e^{-23.3\xi}} + \frac{1}{5.80 \times 10^{21} e^{-35.3\xi}} \right)^{-1} \tag{6–24}$$

Equation (6–24) may be considered to represent formation of two discrete layers in the CC coating after aging.

The measurement model analysis proposed provides a general explanation for situations in which a distribution of film properties results in frequency dispersion. The method is general and may be used to extract resistivity distribution from impedance data. In the present work, the analysis was validated by application to synthetic data derived from a CPE, a power–law distribution of resistivity, and an exponential distribution corresponding to a Young model. The application to experimental data obtained from coated aluminum demonstrates its utility for interpretation of impedance measurements.

CHAPTER 7
SURFACE ANALYSIS APPROACHES

The surface analysis methods are techniques for discovering the chemical structure of an extremely shallow and thin area called the surface number atomic layer of the solid matter. The elemental composition and chemical state of the materials that exist in the very outer surface layer can be investigated by using current surface analyzers. Many industrial and scientific research fields have used surface analysis methods as an essential techniques for research and quality management of materials with new characteristics and features.

7.1 Scanning Electron Microscope

A scanning electron microscope (SEM) is a microscope that uses electrons rather than light to form an image and to examine objects on a very fine scale. The electrons interact with atoms in the sample, producing various signals that can be detected and that contain information about the sample's surface topography, morphology, composition and crystallographic information. A stream of electrons is formed and accelerated toward the specimen using a positive electrical potential, and focused using metal apertures and magnetic lenses into a thin, focused, monochromatic beam. The highest resolution that research SEM can achieve is better than 1 nanometer. The most common SEM mode is the detection of secondary electrons emitted by atoms excited by the electron beam. Imaging with secondary electrons provides information about morphology and surface topography. The contrast is dominated by edge effect, more secondary electron can leave the sample at edges leading to increased brightness.(71)

Low magnification SEM images for corroded and passive ASTM A416 steel in Sika Grout 300PT are shown in Figures 7-1 and 7-2. The SEM images were captured at an accelerating voltage of 10 kV and a working distance of 13.5 mm. The SEM samples was coated by carbon to prevent a charging effect, which is produced by the build-up of electrons in the sample and their uncontrolled discharge that can produce unwanted
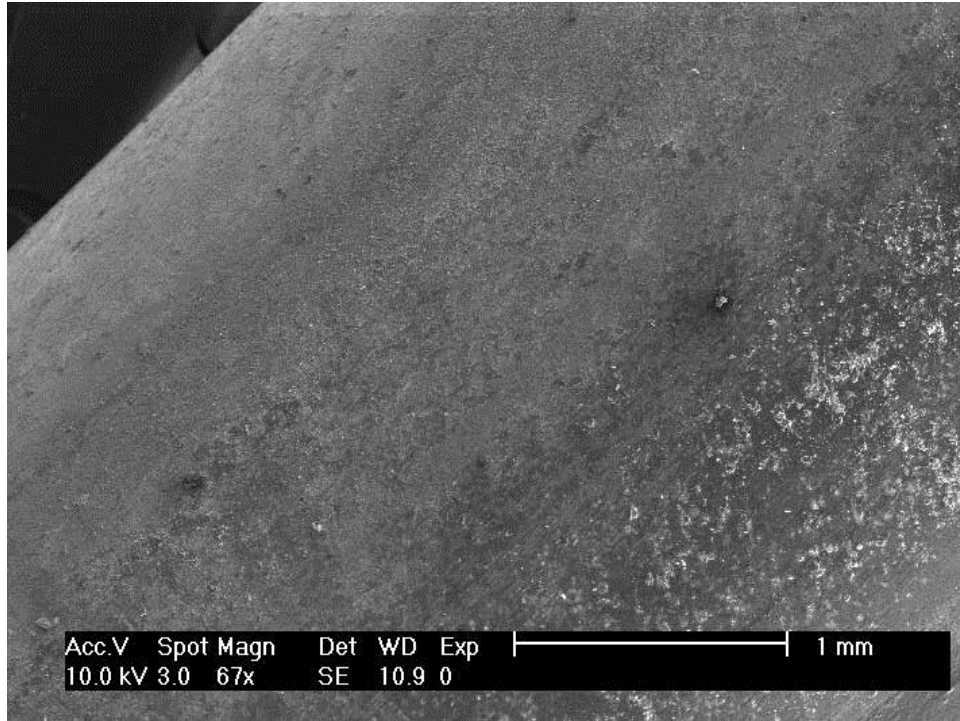
Figure 7-1. Low magnification SEM image from the passive ASTM A416 steel surface in Sika Grout 300PT.
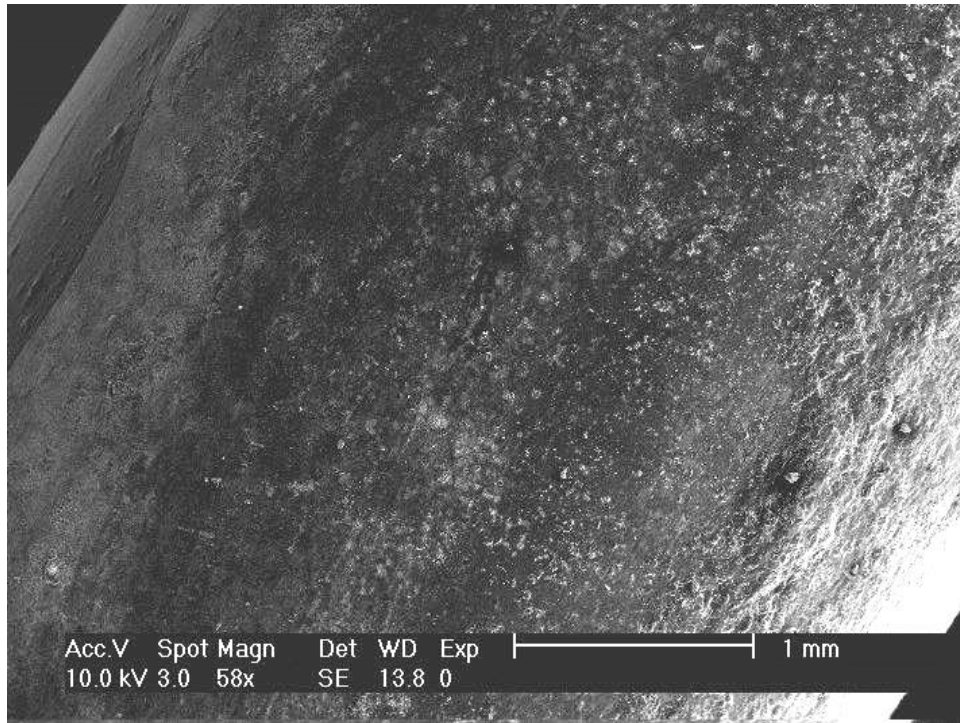
Figure 7-2. Low magnification SEM images from the corroding ASTM A416 steel surface in Sika Grout 300PT.
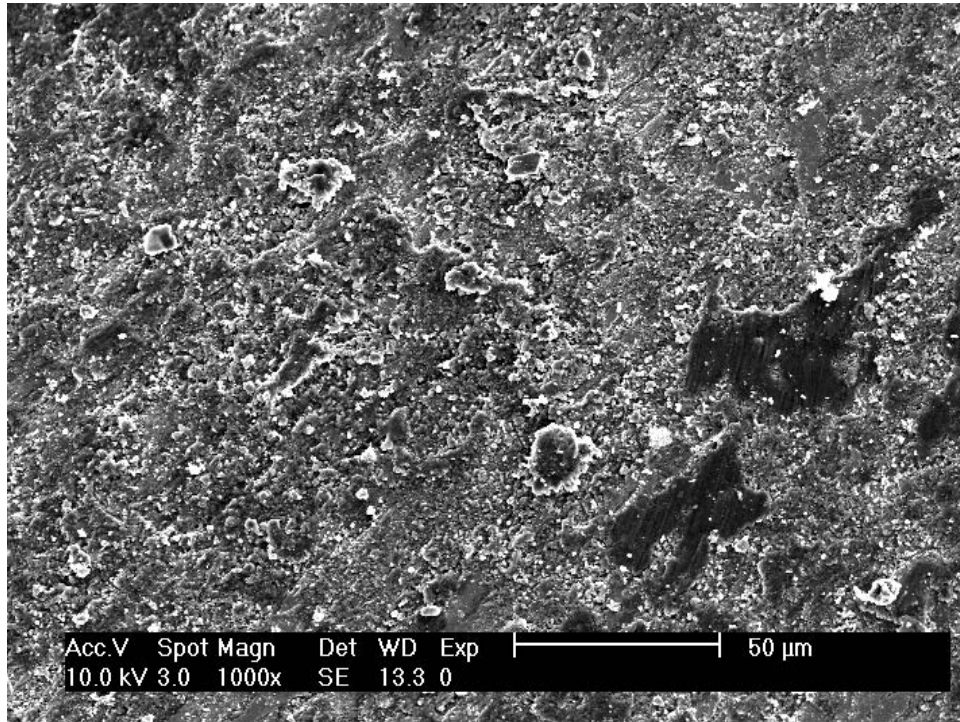
Figure 7-3. High magnification SEM image from the passive ASTM A416 steel surface in Sika Grout 300PT.

artifacts, particularly in secondary electron images. From the SEM images, the corroded ASTM A416 steel has a rougher surface than passive steel. High magnification SEM images for corroded and passive ASTM A416 steel in Sika Grout 300PT are shown in Figures 7-3 and 7-4. These high magnification images also suggested that fewer corrosion products are presented on passive steel than on corroded steel. The size of corrosion products is varied, but generally within 1 to 20μm.

7.2   X-ray Photoelectron Spectroscopy

X-ray photoelectron spectroscopy (XPS), can be applied to a broad range of materials, is the most widely used surface analysis technique. Chemical state of element, relative composition of the constituents in the surface region and valence band structure can be measured. XPS spectra are obtained by irradiating a material with a beam of X-rays whilst simultaneously measuring the kinetic energy and number of electrons that escape from the top 0 to 10 nm of the material being analyzed. The energy of an X-ray
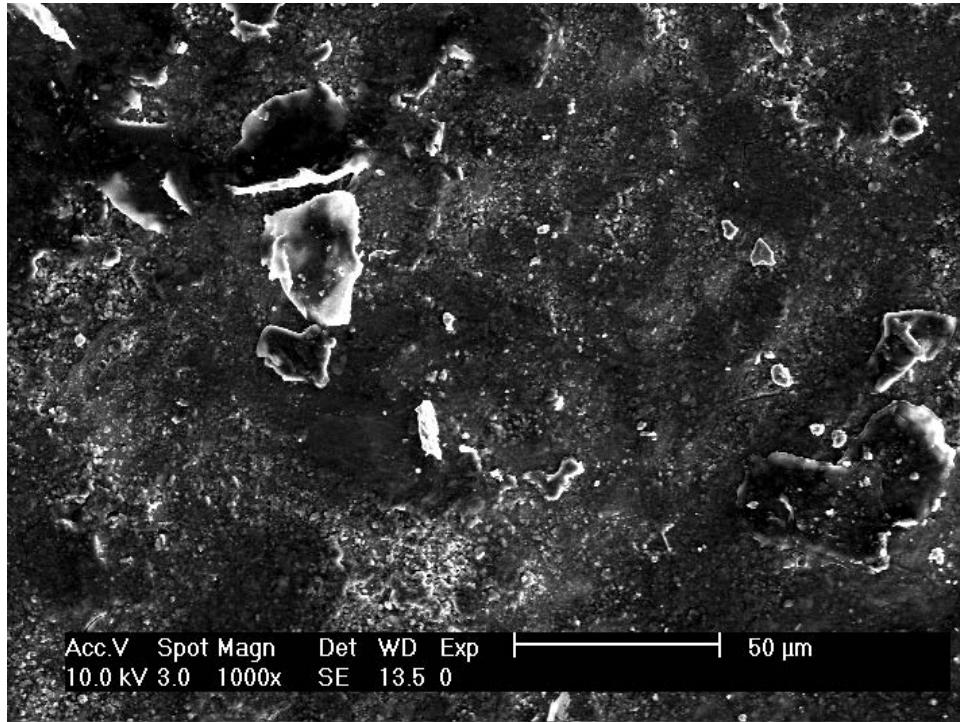
Figure 7-4. High magnification SEM image from the passive ASTM A416 steel surface in
Sika Grout 300PT.

with particular wavelength is known; for example, the energy of Al K X-rays is 1486.7 eV.
Also, since the emitted electrons' kinetic energies can be measured, the electron binding
energy of each of the emitted electrons can be determined by

$$E_{\text{binding}} = E_{\text{photon}} - (E_{\text{kinetic}} + \phi) \tag{7–1}$$

where E_{binding} is the binding energy (BE) of the electron, E_{photon} is the energy of the
X-ray photons being used, E_{kinetic} is the kinetic energy of the electron as measured by the
instrument and ϕ is the work function of the specimens.(72)

   The XPS diagrams for as-received steel in 2012 and 2015 are presented in Figure 7-5.
The major detected species from Figure 7-5(A) and (B) were carbon and oxygen, with iron
as a minor species, suggesting the presence of air-formed oxide. The XPS spectra for No.1
ASTM A416 steel shows peaks corresponding to Si, but the spectra for No.2 steel did not.
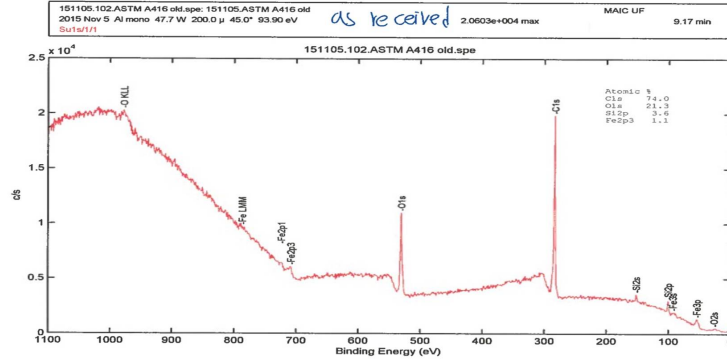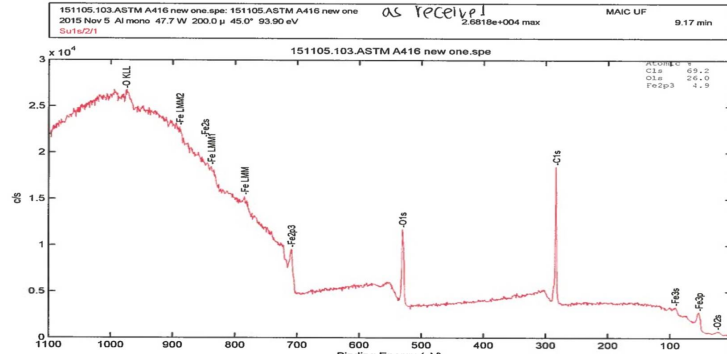
Figure 7-5. XPS spectra of as-received No.1 ASTM A416 steel (A) and No.2 ASTM A416 steel (B).

The XPS spectra for two different sections of the No.2 ASTM A416 steel immersed in simulated pore solution after 8 cycles of cyclic voltammetry scan are presented in Figure 7-6. Calcium peaks in Figure 7-6 suggest that it plays a role in the oxide film composition. It may be attributed to the deposition of $Ca(OH)_2$ from the reaction with hydroxide ions produced by the cathodic reaction, i.e., the oxygen reduction reaction

$$O_2 + 2H_2O + 4e^- \rightarrow 4OH^- \tag{7-2}$$

As the K_{sp} for $Ca(OH)_2$ is 6.5×10^{-6},[73], slightly increased of the concentration of OH^- would cause $Ca(OH)_2$ to deposit. The presence of $Ca(OH)_2$ in the oxide film suggests that oxide film thickness estimation based on iron peaks of XPS, used by several different scientist[20; 26], may not be applied to the case in this dissertation.
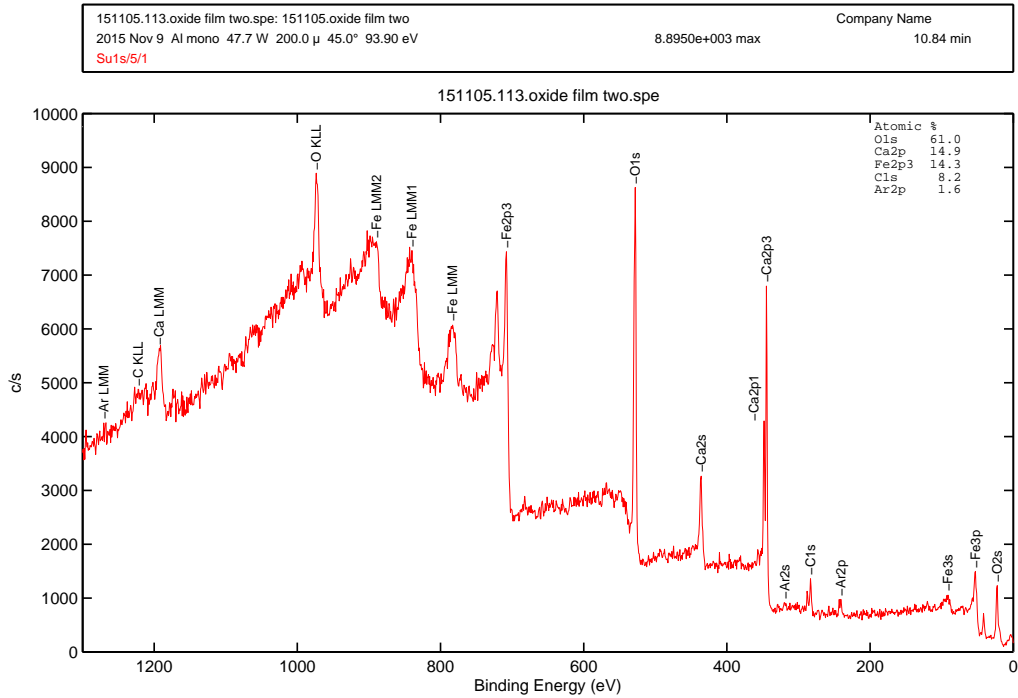
Figure 7-6. XPS spectra of ASTM A416 steel received in 2012 immersed in simulated pore solution after 8 cycles of cyclic voltammetry.

The precipitation of calcium has been addressed by several scientists. Page(74) suggested a dense continuous cement rich layer containing precipitated calcium hydroxide was postulated to be formed at the steelconcrete when concrete was cast against a steel bar. Suryavanshi et al. (75) also found that steel taken from a mortar specimen was covered with a thin, dense white-deposit, approximately 10 to 15 μm in thickness, which showed a strong calcium peak in the EDX spectrum. However, Glass et al. (76) examined the steel-concrete interface by backscattered electron microscopy and observed no continuous $Ca(OH)_2$ layer at the steelconcrete interface.

7.3 High-Resolution Cross-Sectional Transmission Electron Microscope

High-resolution cross-sectional transmission electron microscopy (HR-XTEM) is a technique in which a beam of electrons is transmitted through an ultra-thin specimen, interacting with the specimen as it passes through it. The need to prepare HR-XTEM samples in precise areas or to contain nanometric objects led to the development of the focused ion beam (FIB) tools and the combined focused ion-beam/scanning electron microscope (FIB/SEM) systems, which allow formation of HR-XTEM lamellae from a localized zone with a spatial accuracy of about ten nanometers.(77)

The images for ASTM A416 steel immersed in simulated pore solution after 24 hours of elapsed time from HR-XTEM are shown in Figures 7-7(A) and (B). A clear oxide film cannot be observed from either Figure 7-7(A) or (B), suggesting that HR-XTEM may not be the ideal instrument to investigate the thickness or chemical composition of oxide film. HAADF-STEM imaging is better at revealing the presence of the surface oxide than HR-XTEM because it is more sensitive to compositional variations than HR-XTEM. Therefore, the high annular dark-field scanning transmission electron microscope (HAADF-STEM) was used instead.

7.4 High Annular Dark-Field Scanning Transmission Electron Microscope

Bright field contrast has been utilized by conventional electron tomography, however, due to non-monotonic contrast some bright field images can be unsuitable. Annular dark-field imaging is a method that can be used to map samples in a scanning transmission electron microscope (STEM). The images are formed by collecting scattered electrons with an annular dark-field detector. A scanning transmission electron microscope is one particular type of transmission electron microscope. In contrast to conventional transmission electron microscopes, STEM focuses the electron beam into a narrow spot which is scanned over the sample in a raster.(78)

As the electrons enter the specimen, they interact with columns of atoms and their electrons in several different ways; electrons are scattered weakly or strongly by the
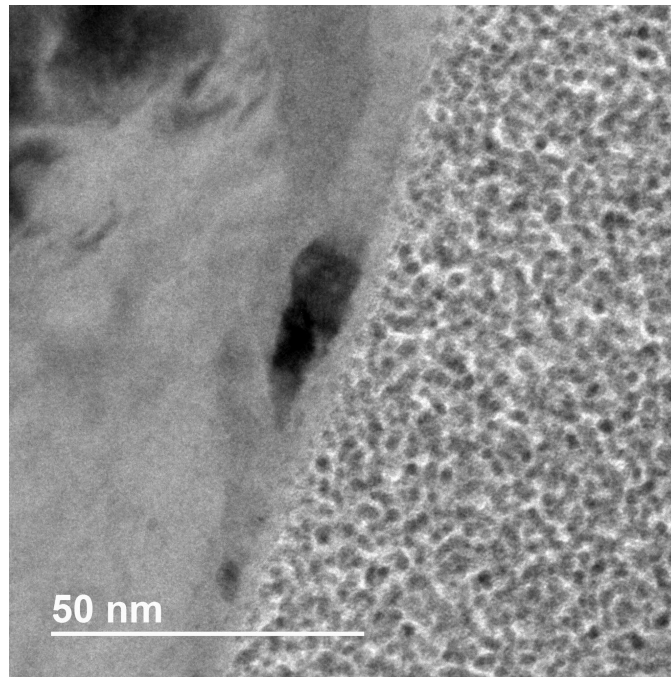
A
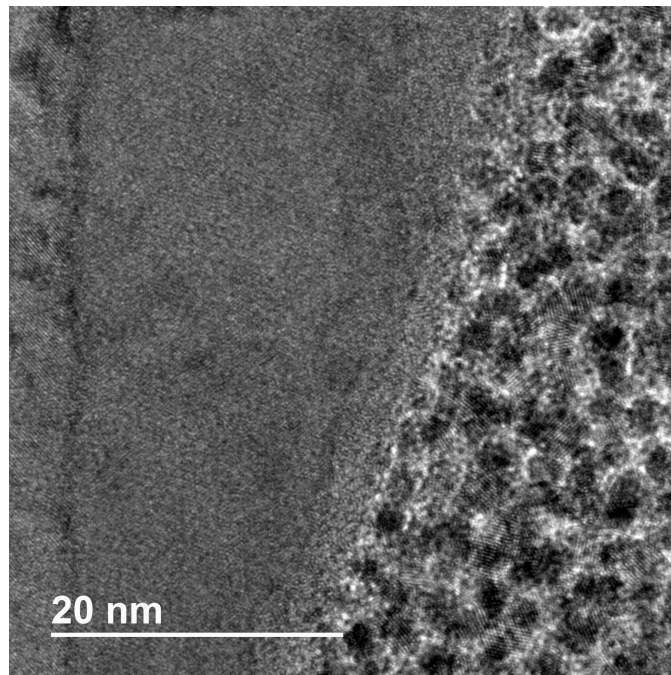
B

Figure 7-7. The HR-XTEM images from the ASTM A416 steel immersed in simulated pore solution after 24 hours of elapsed time: A)100000X magnification B) and 250000X magnification.

specimen based on the strength of the interaction. If the trajectory changes by less than a degree or so, an electron is said to be transmitted and low-angle. Electrons scattered through low angles are said to be elastic in the particle description and coherent in the wave description. The high-angle (2.5 to 6 ^{o}) electrons are inelastic because energy is lost in collisions with atoms in the columns; they are also incoherent since a loss of energy equals an increase in wavelength. An image may be formed in the scanning transmission electron microscope using either the transmitted or scattered electrons. In bright field, the regions of the specimen which transmit electrons appear bright while those that scatter appear dark. In dark field, this contrast scheme is reversed; if a dark field image is formed using selected low-angle electrons, it reveals how groups of atoms are stacked and oriented in the specimen. An image formed using high angle electrons in dark field does not show diffraction contrast, since the inelastic, incoherent electrons do not diffract. The intensity of the high angle scatter basically depends only on the type of column atom. The higher the atomic number of the column atom, the greater the loss of energy as an electron bounces off it. Columns of high atomic number atoms will appear bright since they scatter more strongly, while low atomic number atoms scatter weakly and so appear dark. By using a STEM and a high-angle annular detector, it is possible to obtain atomic resolution images where the contrast is directly related to the atomic number (Z^2). (79; 80; 81)

The images for ASTM A416 steel immersed in simulated pore solution after 24 hours of elapsed time from HAADF-STEM are shown in Figure 7-8 and 7-9. Figure 7-9 suggests that the oxide film thickness for No.2 ASTM A416 steel at open-circuit potential in simulated pore solution after 24 hours of elapsed time is about 4 nm. This value can be used as a calibration of equation (8–4) to adjust ρ_δ for more precise oxide film thickness estimation. However, Figure 7-8 A suggests that the oxide film thickness on No.1 ASTM A416 steel is not uniform. In Figure 7-8 A, the maximum oxide film thickness is about 5±2nm but in Figure 7-8 B no visible oxide film can be observed. The oxide film in Figure 7-9 A and B covered the entire steel surface very well compared to the oxide film in Figure

Steel

Oxide film

3 nm

5 nm

7 nm

Au-Pd

Pt

70nm

A

Steel

Au-Pd

Pt

70nm
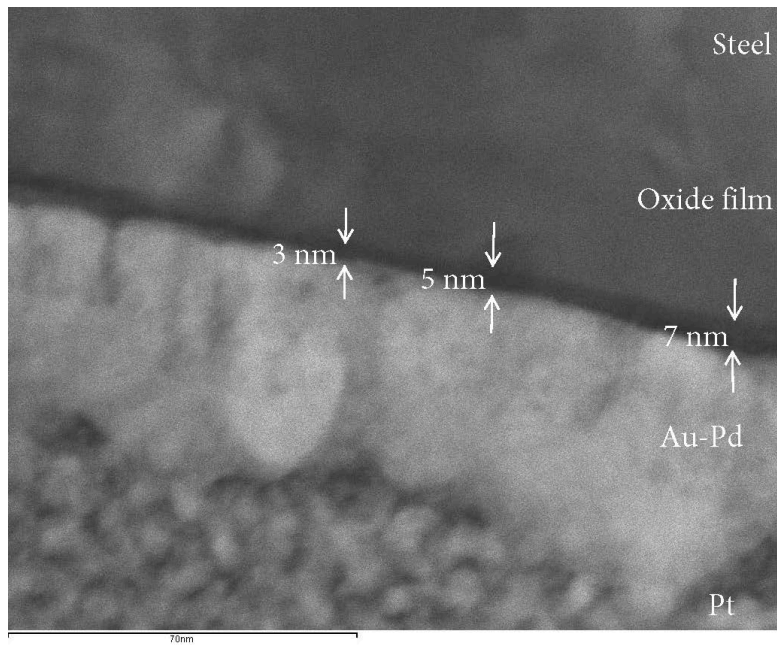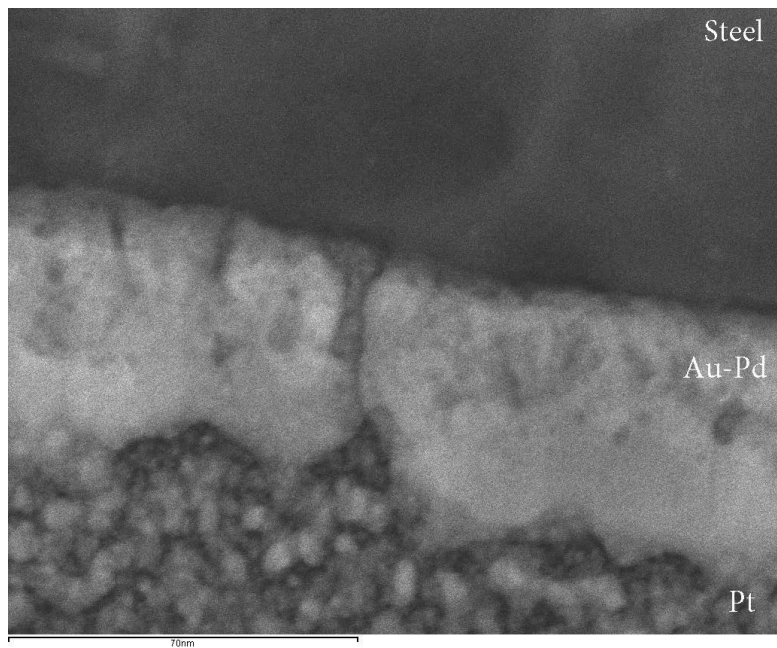
B

Figure 7-8. The 100000X magnification of HAADF-STEM images from the No.1 ASTM A416 steel(label 1 in Figure 4-5 and 4-14) immersed in simulated pore solution after 24 hours of elapsed time.

A

B
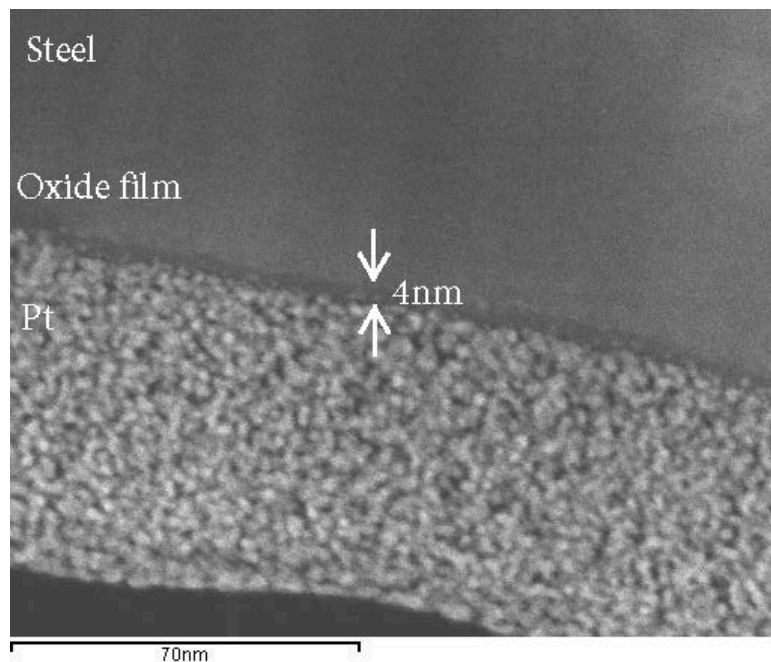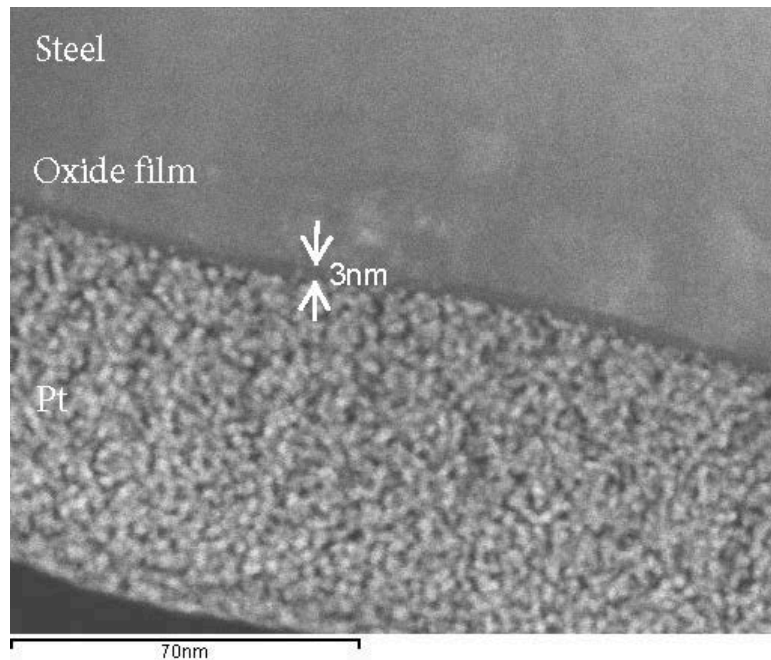
Figure 7-9. The 100000X magnification of HAADF-STEM images from the No.2 ASTM A416 steel(label 2 in Figure 4-5 and 4-14) immersed in simulated pore solution after 24 hours of elapsed time.

7-8 A and B suggesting that oxide film formed on No.2 ASTM A416 steel can provide a better protection to prevent corrosion.

CHAPTER 8
DISCUSSION

Two different process models are required to express two different impedance responses. The porous electrode model presented as equation (5–38) can be expressed in terms of nine independent parameters: R_e, Q, α, $R_{t,a}$, $(R_0 R_{t,c}/2\pi r)^{0.5}$, $C_{c,dl} R_{t,c}$, $R_d/R_{t,c}$, $L(2R_0/R_{t,c})^{0.5}$, and δ_r^2/D_r . While the number of parameters is large, this is the smallest number needed to describe the essential features of the system. The model for the reaction at bottom of pores in dielectric layer is presented as equation (5–40) to comprise an oxide layer with complete coverage. The curve fitting results for different cases, shown as lines in the Nyquist and Bode plots in Figures 4-13 to 4-19, suggest that the models fits the experimental data very closely. The anodic charge–transfer resistance, $R_{t,a}$, may be used to provide an estimate for the corrosion rate. The values for Q and α associated with the constant–phase element may be used to estimate oxide film thickness by use of the power-law model developed by Hirschorn et al. (28; 29)

8.1   Open-Circuit Potential

Parameters extracted from the fitting procedure based on the porous electrode model and the model for reactions at bottom of pores in dielectric layer for the results presented in Figures 4-13 and 4-14 are presented in Tables 8-1 and 8-2.

The anodic charge–transfer resistance, $R_{t,a}$, could only be extracted from impedance data after an elapsed time of 7.2 ks (2 h). The observation that a statistically–significant value for the anodic charge–transfer resistance could not be extracted from the fitting procedure after steady state was reached (300ks) suggests that the steady–state corrosion rate was too small to be measured at the open–circuit potential.

8.2   Influence of Applied Potential

Parameters extracted from the fitting procedure for the results presented in Figures 4-17 and 4-19 are presented in Table 8-3.   An anodic charge–transfer resistance could be be extracted only for steel polarized at +0.22 V(Hg/HgO).

Table 8-1. Values of the regressed parameters obtained from impedance data by porous electrode model collected at the corrosion potential after elapsed times of 7.2 ks (2 h) and 300 ks (85 h).

	Time, ks	7.2	300
R_{e}	Ωcm^2	1.9±0.11	1.3±0.24
$A_1 = (R_0 R_{\text{t,c}}/2\pi n^2 r)^{0.5}$	$\text{k}\Omega/\text{cm}^{1/2}$	0.77±0.02	0.58±0.02
$A_2 = L(2r R_0/R_{\text{t,c}})^{0.5}$	dimensionless	1.4±0.03	0.83±0.05
$A_3 = R_{\text{D}}/R_{\text{t,c}}$	dimensionless	16.2±1.1	31.3±2.03
$A_4 = \delta_r^2/D_r$	s	–	60.4±3.3
$A_5 = C_{\text{dl,c}} R_{\text{t,c}}$	ms	1.2±0.05	7.7±0.44
Q	$\mu\text{s}^\alpha/\Omega cm^2$	16.9±0.04	0.41±0.03
$R_{\text{t,a}}$	$\text{k}\Omega\text{cm}^2$	4.7±0.02	–
α	dimensionless	0.69±0.01	0.70±0.01

Table 8-2. Values of the regressed parameters obtained from impedance data by model for reaction at bottom of pores in dielectric layer collected at the corrosion potential after elapsed times of 300 ks (85 h).

	Time, ks	300
R_{e}	Ωcm^2	2.1±0.0
Q_1	$\mu\text{s}^\alpha/\Omega cm^2$	46±1.9
α_1	dimensionless	0.91±0.00
R_{sp}	$\text{k}\Omega\text{cm}^2$	0.12±0.00
Q_2	$\mu\text{s}^\alpha/\Omega cm^2$	420±2.9
α_2	dimensionless	0.63±0.03
R_{t}	$\text{k}\Omega\text{cm}^2$	–

Table 8-3. Values of the regressed parameters obtained for impedance data measured for No.1 ASTM A416 at different applied potentials after a steady-state current was reached.

	Potential V(Hg/HgO)	-0.38	- 0.28	-0.18	-0.13	-0.03	+0.02	+0.12	+0.22
R_{e}	(Ωcm^2)	1.1±0.05	0.90±0.13	1.3±0.24	1.2±0.04	1.2±0.04	0.69±0.23	1.20±0.21	0.51±0.22
$A_1 = \sqrt{\frac{R_0 R_{\text{t,c}}}{2\pi n^2 r}}$	$(\text{k}\Omega/\text{cm}^{0.5})$	0.59±0.11	0.67±0.01	0.58±0.02	0.70±0.01	0.70±0.01	0.34±0.06	0.29±0.03	0.26±0.07
$A_2 = L\sqrt{\frac{2r R_0}{R_{\text{t,c}}}}$	dimensionless	0.73±0.03	0.77±0.04	0.83±0.05	0.82±0.01	0.82±0.01	0.95±0.12	1.07±0.05	0.99±0.12
$A_3 = R_{\text{D}}/R_{\text{t,c}}$	dimensionless	19±6.3	17±0.44	31±2.0	25±0.8	25±0.8	36±11	83±11	15±3.7
$A_4 = \delta_r^2/D_r$	(s)	203±13	82±3.4	60±3.3	71±3.8	71±3.8	24±2.4	63±16	–
$A_5 = C_{\text{dl,c}} R_{\text{t,c}}$	(ms)	5.8±0.25	7.3±0.46	7.7±0.44	7.8±0.12	8.2 ±0.20	3.4±0.42	2.6±0.15	1.7±0.36
Q	$(\text{ms}^\alpha/\Omega cm^2)$	0.77±0.01	0.66± 0.01	0.41±0.03	0.53±0.01	0.53±0.01	0.44±0.16	0.28± 0.05	0.32±0.10
$R_{\text{t,a}}$	$(\text{k}\Omega\text{cm}^2)$	–	–	–	–	–	–	–	5.90±0.52
α	dimensionless	0.67±0.03	0.66±0.01	0.70±0.01	0.68±0.03	0.68±0.03	0.70±0.05	0.72±0.03	0.69±0.05

Table 8-4. Values of the regressed parameters obtained for impedance data for No.2 ASTM A416 measured at different applied potentials after a steady-state current was reached.

	Potential V(Hg/HgO)	-0.38	-0.28	0.02	0.12	0.22
R_e	Ωcm^2	1.6±0.01	1.5±0.01	2.1±0.02	2.2±0.01	2.4±0.01
Q_1	$\mu s^\alpha/\Omega cm^2$	99±2.7	100±3.1	41±1.3	38±1.5	33±2.1
α_1	dimensionless	0.89±0.003	0.88±0.005	0.92±0.01	0.91±0.003	0.91±0.005
R_{sp}	Ωcm^2	30±1.3	60±3.3	100±3.1	92±3.0	60±3.5
Q_2	$ms^\alpha/\Omega cm^2$	0.9±0.01	0.6±0.02	0.02±0.06	0.4±0.05	0.3±0.07
α_2	dimensionless	0.52±0.001	0.57±0.003	0.63±0.002	0.63±0.003	0.63±0.004
R_t	$k\Omega cm^2$	–	–	–	–	–

8.3   Which Reaction is Visible?

The process of model development requires the understanding of the physical meaning of electrochemical systems. Although at open-circuit potential the cathodic reaction current and the anodic reaction current are balanced, one of these reactions may be more visible in the impedance response than the other due to the difference in reaction impedance. Once which reaction is visible can be determined, the correct process model can be built to interpret the electrochemical systems.

Determination of the visible reaction can be investigated by applying positive and negative potential with respect to open–circuit potential. If a positive potential is applied, and $Z_c \gg Z_a$, only Z_a plays a role in the impedance response. If a negative potential is applied, and $Z_a \gg Z_c$, then only Z_c plays a role in the impedance response. Based on these concepts, for No.1 ASTM A416 steel, both the magnitude of impedance data are decreased with both positive and negative applied potential, suggesting that both reactions are visible. For No.2 ASTM A416 steel, the magnitude of impedance data decreased with negative applied potential but increased with positive applied potential, suggesting that cathodic reaction is visible. Therefore, only the cathodic charge transfer resistance needed to be considered in the process model for No.2 ASTM A416 steel.

8.4   Ohmic Resistance

The ohmic resistance generally decreased with elapsed time due to water evaporation, resulting in an increased ion concentration. For example, the ohmic resistance was

$1.9 \ \Omega\text{cm}^2$ after 7.2ks and decreased to $1.3 \ \Omega\text{cm}^2$ after 300ks. The ohmic resistance decreased further to $0.9 \ \Omega\text{cm}^2$ when the impedance measurement was conducted at -0.28 V(Hg/HgO). At this point, the total elapsed time was about 500ks. The larger ohmic resistance of $1.1 \ \Omega\text{cm}^2$ obtained for the impedance measurement at -0.38 V(Hg/HgO) can be attributed to the addition of simulated pore solution to compensate for the loss of electrolyte volume by evaporation.

8.5 Pore Depth

When presented in a Nyquist format, the angle of low–frequency data with respect to the abscissa depends on the ratio L/λ. When L/λ becomes large, the macropores behave as though they were semi-infinitely deep. In this case, $\coth(L/\lambda)$ tends to unity and $Z_c = (R_0 Z_0)^{1/2}$, which gives an angle of about 22.5 degrees. When the ratio of L/λ is small, the macropores respond like a flat electrode and the cathodic impedance tends to Z_0/L. In this case, the angle made by the diffusion impedance approaches 45 degrees.

In the low–frequency range, the ratio L/λ can be expressed as

$$\left(\frac{L}{\lambda}\right)_{\omega \to 0} \propto \frac{L\sqrt{\dfrac{2\pi R_0}{R_{t,c}}}}{\sqrt{\dfrac{R_D}{R_{t,c}}}} \tag{8-1}$$

For the present results, L/λ had values between 0.12 and 0.2. For these cases, the limiting conditions discussed above were not applicable. Therefore, the term $\coth(L/\lambda)$ was used for all fitting procedures.

8.6 Corrosion Rate

The corrosion rate may be obtained from the definition of charge–transfer resistance[54]

$$R_{t,a} = \frac{\beta_a}{2.303 \times 10^3 \bar{i}_{corr}} \tag{8-2}$$

where β_a is the Tafel slope for the anodic reaction. The steady–state polarization curve is influenced by coupled phenomena and could not be used to estimate a value for the anodic

Tafel slope. Thus, the corrosion rate C_r was estimated from equation (8–2) in which β_a was assigned a value of 60 mV/decade. Application of Faraday's law leads to the steel corrosion rate, C_r (in μm/y), expressed as

$$C_r = \frac{\tau M_{\mathrm{Fe}} i_{\mathrm{corr}}}{1000 n \mathrm{F} \rho_{Fe}} \qquad (8\text{–}3)$$

where τ is the number of seconds per year (3.15×10^7 s/y), M is the molar mass of iron (55.85 g/mol), n is number of electrons transferred in the anodic reaction, F is Faraday's constant (96,487 C/equiv.), ρ_{Fe} is the density of iron (7,860 kg/m^3), and i_{corr} is the corrosion current density (μA/cm^2) obtained from equation (8–2).

The annual corrosion rate for steel exposed for 7.2 ks (2 h) at open circuit, as obtained from the value of $R_{t,a}$ presented in Table 8-1, was 64μm/ year. A corrosion rate could not be estimated after the steady–state condition was reached. The corrosion rate for steel polarized at +0.22 V(Hg/HgO) was 51 μm/ year. The observation that the corrosion rates were too small to be detected for potentials more negative than +0.22 V(Hg/HgO) suggests that the steel is protected by oxide films formed on steel in an alkaline environment.

The inability to detect a steady–state open–circuit corrosion rate in the present work can be attributed to the presence of a porous electrode layer caused by the cathodic pretreatment. In principle, a corrosion rate could be estimated at open–circuit from the cathodic charge–transfer resistance, but this term could not be extracted independently from the impedance model due to the lumped nature of the porous–electrode parameters (see equations (5–33), (5–34), (5–35), and (5–37)). A number of researchers have extracted open–circuit corrosion rates from impedance data for systems that did not undergo the cathodic pretreatment. Sánchez-Moreno et al.(22) reported a corrosion rate of 0.19 μA/cm^2 for steel rebar in a 0.2 M KOH saturated Ca(OH)$_2$ solution after four hours of exposure. Pech-Canul and Castro(33) reported that the corrosion current for A-615 steel rebar in ordinary Portland cement exposed to a marine atmosphere is in the

Table 8-5. Oxide film thickness estimated from equation (8–4) for impedance data
obtained at the corrosion potential with immersion time as a parameter. The
error bars were estimated from confidence intervals for the regressed values of Q
and α by use of a linear propagation of error analysis.

Immersion time, ks	Film thickness, nm
7.2 (2 h)	1.1±0.8
300 (85 h) (No.1 steel)	5.1±0.5
300 (85 h) (No.2 steel)	2.7±0.4

range of 1×10^{-3} μA/cm^2 to 10 μA/cm^2. The corresponding corrosion currents for the
present paper are 5.5 μA/cm^2 and 4.4 μA/cm^2 for steel exposed for 2 hours at open circuit
and for steel polarized at +0.22 V(Hg/HgO), respectively.

8.7 Oxide Film Thickness

The oxide film thickness, δ, was estimated from CPE parameters by use of the model
developed by Hirschorn et al. (28; 29) in which the oxide resistivity was assumed to
have a modified power–law dependence on position. The oxide film thickness, δ, can be
estimated by

$$\delta = \frac{(\varepsilon\varepsilon_0)^\alpha}{gQ\rho_\delta^{1-\alpha}} \tag{8–4}$$

Equation (8–4) requires values for the dielectric constant and the resistivity at position
$y = \delta$. Values for oxide thickness were obtained under the assumption that the dielectric
constant of the oxide could be taken as having a value $\epsilon = 12$ (see page 12:49 of
reference (82)). The parameter ρ_δ, used in the power–law model, was assigned a value
of 10000 Ωcm^2, based on the film thickness, 4 nm, from HAADF-STEM images in Figure
7-9.

The oxide film thicknesses estimated from the regression results shown in Table 8-3
are presented in Table 8-5. The confidence interval for the film thickness was calculated
from the standard deviations of the regression results by use of a linear propagation of
error analysis. The film thickness increased from a value of 1.1 nm after 7.2 ks (2 h)
immersion to 5.1 nm as the system approached the steady–state open–circuit potential.

Table 8-6. Oxide film thickness estimated from equation (8–4) for impedance data obtained under steady-state conditions with applied potential as a parameter. The error bars were estimated from confidence intervals for the regressed values of Q qne α by use of a linear propagation of error analysis.

Potential, V(Hg/HgO)	Film thickness, nm (No.1 steel)	Film thickness, nm (No.2 steel)
-0.38	5.4±0.3	2.0±0.1
-0.28	6.0±0.3	2.8±0.2
-0.18	6.2±0.4	(-)
-0.13	5.8±0.7	(-)
-0.03	6.3±0.8	(-)
+0.02	5.6±0.8	2.7±0.3
+0.12	5.6±1.3	3.0±0.5
+0.22	8.8±1.7	3.6±0.9

The substantial change in film thickness may explain the long time required to reach steady values of open–circuit potential.

The oxide film thicknesses estimated from the regression results shown in Table 8-3 are presented in Table 8-6. The film thickness values shown in Table 8-6 are typically larger than the value of 5 nm reported in Table 8-5 for an elapsed time of 300 ks. The increase in film thickness may be attributed to the growth of the oxide film as samples subjected to the protocol required to generate Table 8-6 were exposed to the electrolytic environment for both the 300 ks required to reach steady state at open circuit and the time time required to reach steady state at the applied potential. For steel polarized at negative potential, the thickness of the oxide film at -0.18 V(Hg/HgO) was larger than at the steady–state corrosion potential (-0.08 V(Hg/HgO)), suggesting that the oxide film could still be formed at slightly negative potentials. The decrease of oxide film thickness at more negative potentials is in agreement with the use of cathodic pre-treatment to remove air-formed oxide films.

The oxide film thickness is presented in Figure 8-1 as a function of total elapsed time, comprising the time required to reach a steady open–circuit potential and the time required to reach a steady current density at an applied potential. The results shown in Figure 8-1 suggest that the elapsed time is a more important factor than the applied
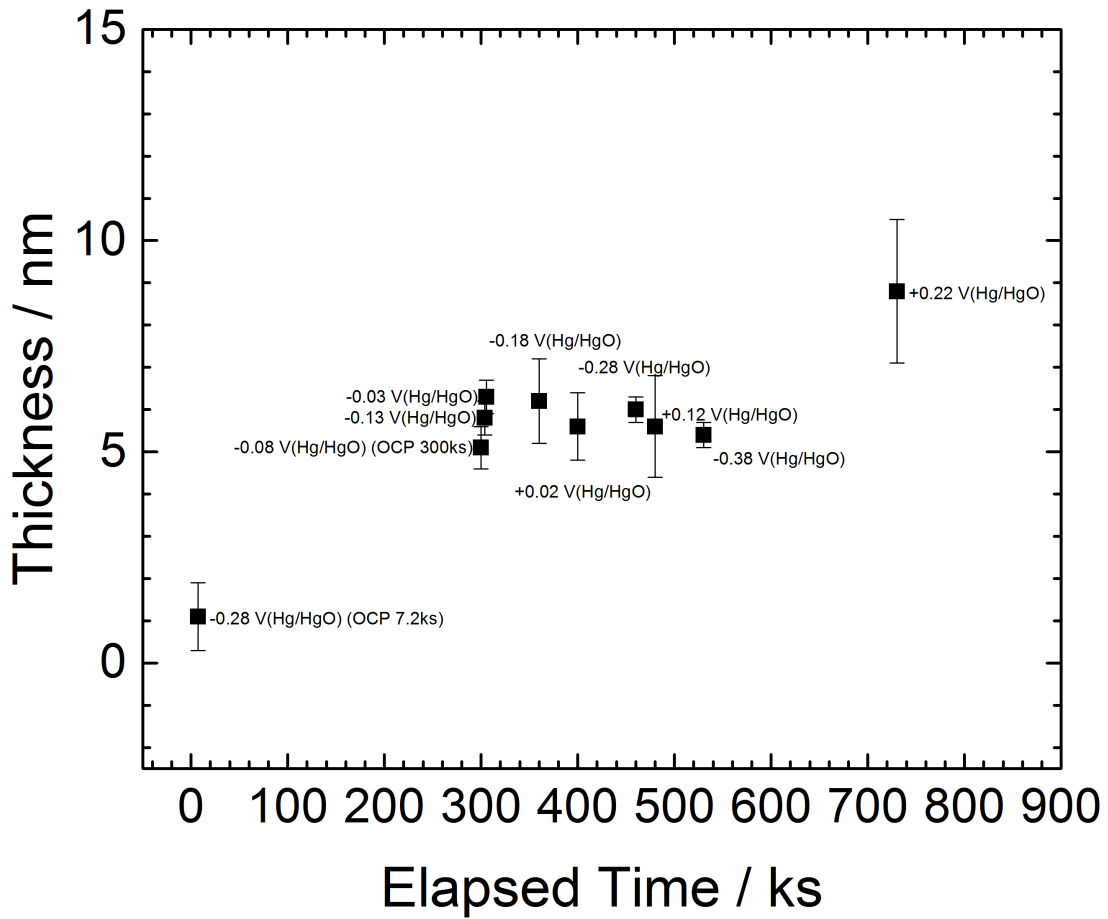
Figure 8-1. Film thickness estimated from equation (8–4) as a function of elapsed time with applied potential as a parameter. The error bars were estimated from confidence intervals for the regressed values of Q qne α by use of a linear propagation of error analysis.

potential for determining the oxide film thickness. The thickness of the oxide film at similar elapsed times has similar values, independent of the applied potential.

CHAPTER 9
CONCLUSION

Preliminary experiments were conducted to investigate the influence of chloride ions and dissolved oxygen on the corrosion of steel in simulated pore solution. The chloride threshold level (CTL) for an ASTM A416 steel is about 1. However, the impedance measurements at open-circuit potential did not show a significant difference between ASTM A416 steel immersed in a 40g/L NaCl added solution and in a chloride-free solution. This suggests that the corrosion initiated as pitting can happen when both chloride threshold level and pitting potential are reached; the pitting potential from cyclic voltammetry is about 0.4 V(SCE) and the repassivation potential is about -0.6 V(SCE). The anaerobic corrosion behavior of ASTM A416 steel has been investigated by sparging BIP grade nitrogen gas (Airgas) to deaerate the system. The impedance results from ASTM A416 steel in aerobic and anaerobic simulated pore solution still did not show significant difference. The reasons causing the corrosion of ASTM A416 steel in concrete shall be attributed to other factors.

The open–circuit potential measurements suggest that a steady state was reached after 300 ks. At other potentials, the steady–state current was generally obtained after 50ks. At +0.22 V(Hg/HgO), an elapsed time of 250 ks was required to reach the steady-state. Two different cyclic voltammetry results can be observed from ASTM A416 steel; for No.1 ASTM A416 steel, the possible corrosion products were FeO, $Fe(OH)_2$, and Fe_3O_4, while the possible corrosion products on No.2 ASTM A416 steel were Fe_3O_4, γ-Fe_2O_3, α-FeOOH, FeO and $Fe(OH)_2$, based on the similarity of results with published in-situ Raman spectroscopy measurements for a similar steel. The steady-state polarization curve also suggested that an oxide film was formed on the steel surface.

The preliminary application of the measurement model to impedance results allowed for the assessment of experimental noise and the removal of non-stationary data. The

estimate of the stochastic error was then introduced to weigh regression of the physical model.

Before steady-state was reached, the impedance of ASTM A416 steels in simulated pore solution showed porous electrode behavior. After steady-state was reached, the No.1 ASTM A416 steel still showed porous electrode behavior, whereas the impedance response of the No.2 ASTM A416 steel showed the behavior of a reaction at the bottom of pores in a dielectric layer. For porous electrode behavior, the impedance model had three main elements: an ohmic resistance and a parallel combination of an anodic reaction impedance, a cathodic reaction impedance, and a constant–phase element associated with the charging current. The cathodic reaction impedance was based on the porous electrode theory developed by de Levie.(40) The porous electrode behavior observed resulted from the cathodic pre-treatment used to remove the air-formed oxide film, and from the α-FeOOH presented in oxide film.(83) For models with a reaction at the bottom of pores in a dielectric layer, the parallel combination of Q_2 and R_2 are associated to a redox process in the passive layer between magnetite and iron(III) oxides.(65) The impedance of the film was modeled as a constant-phase element with parameters Q_1 and α_1, under the assumption that the film has a distribution of resistivity normal to the electrode surface, and the ohmic resistance inside the film can be described by R_1.

Regression strategies for this dissertation include the Downhill Simplex method and Levenberg-Marquardt method. The Downhill Simplex method is a commonly applied numerical method used to find the minimum or maximum of an objective function in a multidimensional space. It does not require the evaluation of the derivatives or the inversion of a matrix that may have zero determinants. This algorithm is based on a simplex; the simplest volume in the N-dimensional parameter area, which is stretched from N+1 points. The Levenberg-Marquardt method is a compromise between the Gauss-Newton and the Steepest Descent methods. Its critical concepts are the selection of

a scaling factor for the method of steepest descent, and an approach for making a smooth transition from one method to the other.

The corrosion behavior of ASTM A416 steel was further examined by several different surface analyses. The low magnification SEM images for corroded and passive ASTM A416 steel in Sika Grout 300PT suggest that corroded ASTM A416 steel has a rougher surface than passive steel and the size of the corrosion products is varied, but generally within 1 to $20\mu m$. The XPS spectra for No.2 ASTM A416 steel after 8 cycles of cyclic voltammetry scan suggested that calcium plays a role in oxide film composition, which may be attributed to the deposition of $Ca(OH)_2$ from the cathodic reaction. HR-XTEM and HAADF-STEM were applied to measure the oxide film thickness of ASTM A416 steel in simulated pore solution; the images from HR-XTEM cannot provide clear oxide film thickness. From HAADF-STEM, the oxide film thickness on No.1 ASTM A416 steel is varied; 3-7 nm may be measured on one spot but at another spot the oxide film can barely been detected. The oxide film thickness on No.2 ASTM A416 steel is relatively uniform; about 4 nm for all available images.

The oxide film thickness can also be estimated from the constant phase element parameters extracted from the fitting procedure. From HAADF-STEM, the essential parameter to estimate oxide film thickness, ρ_δ, is about 10000 Ωcm. The oxide film thickness estimated from power-law model suggested that it was increased with time. The variation of film thickness with applied potential could be attributed to the greater immersion time required to perform steady state measurements at the applied potential. The anodic charge transfer resistance could only be extracted from impedance data measured after 7.2 ks (2 h) of immersion. For this short time of exposure, the corrosion rate was $64\mu m$/ year, and the corrosion rate could not be determined after steady–state was achieved. For No.1 steel polarized at +0.22V (Hg/HgO), the steady-state corrosion rate was $50\mu m$/ year. Steady–state corrosion rates could not be detected for any other potential tested for both No.1 and No.2 ASTM A416 steel.

CHAPTER 10
SUGGESTIONS FOR FUTURE WORK

The corrosion behavior of ASTM A416 steel was analyzed by electrochemical approaches and surface analyses. The results of cyclic voltammetry, EIS, and XPS suggested that the chemical composition of ASTM A416 steel was inconsistent. The quality control of ASTM A416 steel may need to be improved to reduce galvanic coupling issues, which may cause localized corrosion on the ASTM A416 steels.

Cyclic voltammetry also suggested that the oxide film for No.1 steel were FeO, $Fe(OH)_2$, and Fe_3O_4, while the possible corrosion products on No.2 ASTM A416 steel were Fe_3O_4, γ-Fe_2O_3, α-$FeOOH$, FeO and $Fe(OH)_2$. The chemical composition of the oxide films can be verified by conducting EELS measurement. Since the oxide film of carbon steel in simulated concrete pore solutions may contain three indistinct layers, conducting EELS measurement may help to understand the distribution of the chemical composition of the oxide films.

The corrosion behavior of ASTM A416 steel may be significantly influenced by pH. The experiments can be conducted at different pH values, for example, in a weak basic solution or in a weak acid solution. The Pourbaix diagram of iron suggests that a protective film cannot be formed at the open-circuit potential in a solution with pH below 9. Therefore, the impedance measurement of ASTM A416 steel in a weak basic solution may be substantially different than the impedance measured in a simulated pore solution.

REFERENCES

[1] L. Li, A. A. Sagüés, Effect of chloride concentration on the pitting and repassivation potentials of reinforcing steel in alkaline solutions, in: Proceedings of Corrosion/1999, no. 567, NACE International, Houston, Texas, 1999, pp. 1–11.

[2] J. C. Griess, D. J. Naus, Corrosion of steel tendons used in prestressed concrete pressure vessels, in: D. Tonini, J. Gaidis (Eds.), Corrosion of Reinforcing Steel in Concrete, STP 713, ASTM International, Philadelphia, PA, 1980, pp. 32–50.

[3] M. E. Orazem, B. Tribollet, Electrochemical impedance spectroscopy, Vol. 48, John Wiley & Sons, 2011.

[4] M. Pourbaix, Atlas of Electrochemical Equilibria in Aqueous Solutions, NACE International: The Corrosion Society, Houston, Texas, USA, 1974.

[5] J. Corven, A. Moreton, Post-tensioning tendon installation and grouting manual, Final Report FHWA-NHI-13-026, U.S. Department of Transportation, Washington, D.C. (2013).

[6] J. Feld, K. L. Carper, Construction Failure, Vol. 78 of Practical Construction Guides, John Wiley & Sons, Hoboken, NJ, 1997.

[7] R. Powers, A. Sagüés, Y. Virmani, Corrosion of post-tensioned tendons in Florida bridges, Research Report FL/DOT/SMO/04-475, Florida Department of Transportation, Tallahassee, FL (2001).

[8] J. Corven, Mid-bay bridge post-tensioning evaluation, Final report, Florida Department of Transportation, Tallahasse, FL (2001).

[9] A. Sagüés, R. Powers, H. Wang, Mechanism of corrosion of steel strands in post tensioned grouted assemblies, in: Proceedings of Corrosion/2003, no. 312, National Association of Corrosion Engineers, Houston, TX, 2003, pp. 1–15.

[10] J. Rafols, K. Lau, I. Lasa, M. Paredes, A. ElSafty, Approach to determine corrosion propensity in post-tensioned tendons with deficient grout, Open Journal of Civil Engineering 3 (2013) 182–187.

[11] L. Bertolini, M. Carsana, High pH corrosion of prestressing steel in segregated grout, in: C. Andrade, G. Mancini (Eds.), Modelling of corroding concrete structures, Springer, Berlin, Germany, 2011, pp. 147–158.

[12] T. Hamilton, J. West, J. Wouters, Corrosion of prestressing steels, Committee Report ACI 222.2R-01, American Concrete Institute, Farmington Hills, MI (Februrary 2001).

[13] G. Glass, B. Reddy, N. Buenfeld, The participation of bound chloride in passive film breakdown on steel in concrete, Corrosion Science 42 (11) (2000) 2013–2021.

[14] G. Glass, B. Reddy, N. Buenfeld, Corrosion inhibition in concrete arising from its acid neutralisation capacity, Corrosion Science 42 (9) (2000) 1587–1598.

[15] M. Moreno, W. Morris, M. Alvarez, G. Duffó, Corrosion of reinforcing steel in simulated concrete pore solutions: effect of carbonation and chloride content, Corrosion Science 46 (11) (2004) 2681–2699.

[16] C. Page, Ø. Vennesland, Pore solution composition and chloride binding capacity of silica-fume cement pastes, Matériaux et Construction 16 (1) (1983) 19–25.

[17] C. L. Page, K. W. J. Treadaway, Aspects of the electrochemistry of steel in concrete, Nature 297 (1982) 109–115.

[18] V. Gouda, Corrosion and corrosion inhibition of reinforcing steel: I. immersed in alkaline solutions, British Corrosion Journal 5 (5) (1970) 198–203.

[19] T. Zakroczymski, C.-J. Fan, Z. Szklarska-Smialowska, Kinetics and mechanism of passive film formation on iron in 0.05 m naoh, Journal of the Electrochemical Society 132 (12) (1985) 2862–2867.

[20] P. Ghods, O. B. Isgor, F. Bensebaa, D. Kingston, Angle-resolved XPS study of carbon steel passivity and chloride-induced depassivation in simulated concrete pore solution, Corrosion Science 58 (2012) 159–167.

[21] P. Ghods, O. Isgor, G. McRae, G. Gu, Electrochemical investigation of chloride-induced depassivation of black steel rebar under simulated service conditions, Corrosion Science 52 (5) (2010) 1649–1659.

[22] M. Sánchez-Moreno, H. Takenouti, J. García-Jareño, F. Vicente, C. Alonso, A theoretical approach of impedance spectroscopy during the passivation of steel in alkaline media, Electrochimica Acta 54 (28) (2009) 7222–7226.

[23] D. Geana, A. El Miligy, W. Lorenz, Electrochemical behaviour of iron in alkaline sulphate solutions, Journal of Applied Electrochemistry 4 (4) (1974) 337–345.

[24] S. Joiret, M. Keddam, X. Nóvoa, M. Pérez, C. Rangel, H. Takenouti, Use of EIS, ring-disk electrode, EQCM and Raman spectroscopy to study the film of oxides formed on iron in 1 m naoh, Cement and Concrete Composites 24 (1) (2002) 7–15.

[25] M. Montemor, A. Simoes, M. Ferreira, Analytical characterization of the passive film formed on steel in solutions simulating the concrete interstitial electrolyte, Corrosion 54 (5) (1998) 347–353.

[26] P. Ghods, O. Isgor, J. Brown, F. Bensebaa, D. Kingston, XPS depth profiling study on the passive oxide film of carbon steel in saturated calcium hydroxide solution and the effect of chloride on the film properties, Applied Surface Science 257 (10) (2011) 4669–4677.

[27] H. B. Gunay, P. Ghods, O. B. Isgor, G. J. Carpenter, X. Wu, Characterization of atomic structure of oxide films on carbon steel in simulated concrete pore solutions using EELS, Applied Surface Science 274 (2013) 195–202.

[28] B. Hirschorn, M. E. Orazem, B. Tribollet, V. Vivier, I. Frateur, M. Musiani, Constant-phase-element behavior caused by resistivity distributions in films: 1. Theory, Journal of The Electrochemical Society 157 (12) (2010) C452–C457.

[29] B. Hirschorn, M. E. Orazem, B. Tribollet, V. Vivier, I. Frateur, M. Musiani, Constant-phase-element behavior caused by resistivity distributions in films: 2. Applications, Journal of The Electrochemical Society 157 (12) (2010) C458–C463.

[30] M. Sánche, J. Gregori, C. Alonso, J. Garca-Jaren, H. Takenouti, F. Vicente, Electrochemical impedance spectroscopy for studying passive layers on steel rebars immersed in alkaline solutions simulating concrete pores, Electrochemical Acta 52 (2007) 7634–7641.

[31] J. Flis, H. W. Pickering, K. Osseo-Asare, Interpretation of impedance data for reinforcing steel in alkaline solution containing chlorides and acetates, Electrochemical Acta 43 (1998) 1921–1929.

[32] L. Dhouibi, E. Triki, A. Raharinaivo, The application of electrochemical impedance spectroscopy to determine the long-term effectiveness of corrosion inhibitors for steel in concrete, Cement and Concrete Composites 24 (1) (2002) 35–43.

[33] M. Pech-Canul, P. Castro, Corrosion measurements of steel reinforcement in concrete exposed to a tropical marine atmosphere, Cement and Concrete Research 32 (3) (2002) 491–498.

[34] M. Pour-Ghaz, O. B. Isgor, P. Ghods, The effect of temperature on the corrosion of steel in concrete. part 1: Simulated polarization resistance tests and model development, Corrosion Science 51 (2) (2009) 415–425.

[35] M. Pour-Ghaz, O. B. Isgor, P. Ghods, The effect of temperature on the corrosion of steel in concrete. part 2: Model verification and parametric study, Corrosion science 51 (2) (2009) 426–433.

[36] N. Smart, D. Blackwood, L. Werme, The anaerobic corrosion of carbon steel and cast iron in artificial groundwaters, Tech. rep., Swedish Nuclear Fuel and Waste Management Co. (2001).

[37] R. Asma, P. Yuli, C. Mokhtar, Study on the effect of surface finish on corrosion of carbon steel in co2 environment, Journal of Applied Sciences 11 (11) (2011) 2053–2057.

[38] F. R. Foulkes, P. McGrath, A rapid cyclic voltammetric method for studying cement factors affecting the corrosion of reinforced concrete, Cement and Concrete Research 29 (6) (1999) 873–883.

[39] L. Freire, X. Nóvoa, G. Pena, V. Vivier, On the corrosion mechanism of AISI 204Cu stainless steel in chlorinated alkaline media, Corrosion Science 50 (11) (2008) 3205–3212.

[40] R. de Levie, Electrochemical responses of porous and rough electrodes, in: P. Delahay (Ed.), Advances in Electrochemistry and Electrochemical Engineering, Vol. 6, Interscience, New York, NY, 1967, pp. 329–397.

[41] C. L. Alexander, B. Tribollet, M. E. Orazem, Contribution of surface distributions to constant-phase-element (CPE) behavior: 1. influence of roughness, Electrochimica Acta 173 (10) (2015) 416–424.

[42] M. E. Orazem, N. Pébère, B. Tribollet, Enhanced graphical representation of electrochemical impedance data, Journal of the Electrochemical Society 153 (2006) B129–B136.

[43] K. Bouzek, I. Roušar, Current efficiency during anodic dissolution of iron to ferrate (VI) in concentrated alkali hydroxide solutions, Journal of Applied Electrochemistry 23 (12) (1993) 1317–1322.

[44] M. Büchler, H. Schöneich, Investigation of alternating current corrosion of cathodically protected pipelines: Development of a detection method, mitigation measures, and a model for the mechanism, Corrosion 65 (9) (2009) 578–586.

[45] P. Agarwal, M. E. Orazem, L. H. García-Rubio, Measurement models for electrochemical impedance spectroscopy: 1. Demonstration of applicability, Journal of the Electrochemical Society 139 (7) (1992) 1917–1927.

[46] P. Agarwal, O. D. Crisalle, M. E. Orazem, L. H. García-Rubio, Measurement models for electrochemical impedance spectroscopy: 2. Determination of the stochastic contribution to the error structure, Journal of the Electrochemical Society 142 (1995) 4149–4158.

[47] P. Agarwal, M. E. Orazem, L. H. García-Rubio, Measurement models for electrochemical impedance spectroscopy: 3. Evaluation of consistency with the kramers-kronig relations, Journal of the Electrochemical Society 142 (1995) 4159–4168.

[48] V. M.-W. Huang, V. Vivier, M. E. Orazem, N. Pébère, B. Tribollet, The apparent CPE behavior of an ideally polarized disk electrode: A global and local impedance analysis, Journal of the Electrochemical Society 154 (2007) C81–C88.

[49] A. M. Legendre, Nouvelles Méthodes pour la Détermination des Orbites des Comètes: Appendice sur la Méthode des Moindres Carrés, Courcier, Paris, 1806.

[50] C. F. Gauss, Supplementum theoriae combinationis observationum erroribus minimis obnoxiae, Werke Bd. 4 (1826) 104–108.

[51] C. F. Gauss, Theoria combinationis observationum erroribus minimis obnoxiae, Werke Bd. 4 (1821) 3–26.

[52] H. A. Kramers, Die dispersion und absorption von röntgenstrahlen, Phys. Zs. 30 (1929) 522–523.

[53] R. de L. Kronig, On the theory of dispersion of x-rays, Journal of the Optical Society of America and Review of Scientific Instruments 12 (6) (1926) 547–557.

[54] M. E. Orazem, B. Tribollet, Electrochemical Impedance Spectroscopy, John Wiley & Sons, Hoboken, NJ, 2008.

[55] W. H. Press, S. A. Teukolsky, W. T. Vetterling, B. P. Flannery, Numerical Recipes in C, 2nd Edition, Cambridge University Press, Cambridge, 1992.

[56] J. A. Nelder, R. Mead, A simplex method for function minimization, The computer journal 7 (4) (1965) 308–313.

[57] J. J. Moré, The levenberg-marquardt algorithm: implementation and theory, in: Numerical analysis, Springer, 1978, pp. 105–116.

[58] Y.-M. Chen, M. E. Orazem, Impedance analysis of ASTM A416 tendon steel corrosion in alkaline simulated pore solutions, Corrosion Science.

[59] J.-B. Jorcin, M. E. Orazem, N. Pébère, B. Tribollet, CPE analysis by local electrochemical impedance spectroscopy, Electrochimica Acta 51 (2006) 1473–1479.

[60] B. Hirschorn, M. E. Orazem, B. Tribollet, V. Vivier, I. Frateur, M. Musiani, Determination of effective capacitance and film thickness from constant-phase-element parameters, Electrochimica Acta 55 (21) (2010) 6218–6227.

[61] M. E. Orazem, N. Pébère, B. Tribollet, Enhanced graphical representation of electrochemical impedance data, Journal of The Electrochemical Society 153 (4) (2006) B129–B136.

[62] P. Drossbach, J. Schulz, Elektrochemische untersuchungen an kohleelektrodeni: Die überspannung des wasserstoffs, Electrochimica Acta 9 (11) (1964) 1391–1404.

[63] O. J. Murphy, J. O. Bockris, T. E. Pou, D. L. Cocke, G. Sparrow, Sims evidence concerning water in passive layers, Journal of the Electrochemical Society 129 (9) (1982) 2149–2151.

[64] J. Eldridge, R. Hoffman, A mössbauer spectroscopy study of the potential dependence of passivated iron films, Journal of The Electrochemical Society 136 (4) (1989) 955–961.

[65] L. Freire, X. Nóvoa, M. Montemor, M. Carmezim, Study of passive films formed on mild steel in alkaline media by the application of anodic potentials, Materials Chemistry and Physics 114 (2) (2009) 962–972.

[66] M. E. Orazem, A systematic approach toward error structure identification for impedance spectroscopy, Journal of Electroanalytical Chemistry 572 (2004) 317–327.

[67] L. Young, Anodic oxide films 4: The interpretation of impedance measurements on oxide coated electrodes on niobium, Trans. Farad. Soc. 51 (1955) 1250–1260.

[68] L. Young, Anodic Oxide Films, Academic Press, New York, 1961.

[69] A. S. Nguyen, M. Musiani, M. E. Orazem, N. Pébère, B. Tribollet, V. Vivier, Impedance analysis of the distributed resistivity of coatings in dry and wet conditions, Electrochimica Acta 179 (2015) 452–459.

[70] A. S. Nguyen, M. Musiani, M. E. Orazem, N. Pébère, B. Tribollet, V. Vivier, Impedance study of the influence of chromates on the properties of waterborne coatings deposited on 2024 aluminium alloy, Corrosion Science.

[71] J. Goldstein, D. E. Newbury, P. Echlin, D. C. Joy, A. D. Romig Jr, C. E. Lyman, C. Fiori, E. Lifshin, Scanning electron microscopy and X-ray microanalysis: a text for biologists, materials scientists, and geologists, Springer Science & Business Media, 2012.

[72] J. F. Watts, J. Wolstenholme, An introduction to surface analysis by xps and aes, An Introduction to Surface Analysis by XPS and AES, by John F. Watts, John Wolstenholme, pp. 224. ISBN 0-470-84713-1. Wiley-VCH, May 2003. (2003) 224.

[73] D. C. Harris, Quantitative chemical analysis, Macmillan, 2010.

[74] C. Page, Mechanism of corrosion protection in reinforced concrete marine structures, Nature 258 (1975) 514–515.

[75] A. Suryavanshi, J. Scantlebury, S. Lyon, Corrosion of reinforcement steel embedded in high water-cement ratio concrete contaminated with chloride, Cement and Concrete Composites 20 (4) (1998) 263–281.

[76] G. Glass, R. Yang, T. Dickhaus, N. Buenfeld, Backscattered electron imaging of the steel–concrete interface, Corrosion Science 43 (4) (2001) 605–610.

[77] M. Jublot, M. Texier, Sample preparation by focused ion beam micromachining for transmission electron microscopy imaging in front-view, Micron 56 (2014) 63–67.

[78] S. J. Pennycook, P. D. Nellist, Scanning transmission electron microscopy: imaging and analysis, Springer Science & Business Media, 2011.

[79] D. B. Williams, C. B. Carter, The transmission electron microscope, Springer, 1996.

[80] A. V. Crewe, J. Wall, J. Langmore, Visibility of single atoms, Science 168 (3937) (1970) 1338–1340.

[81] S. Pennycook, L. Boatner, Chemically sensitive structure-imaging with a scanning transmission electron microscope, Nature 336 (6199) (1988) 565–567.

[82] W. M. Haynes (Ed.), CRC Handbook of Chemistry and Physics, 93rd Edition, Taylor and Francis Group, LLC, New York, New York, 2012.

[83] P. Schmuki, M. Büchler, S. Virtanen, H. Isaacs, M. Ryan, H. Böhni, Passivity of iron in alkaline solutions studied by in situ xanes and a laser reflection technique, Journal of the Electrochemical Society 146 (6) (1999) 2097–2102.

BIOGRAPHICAL SKETCH

Yu-Min Chen received his Bachelor of Science degree in chemical engineering from National Taiwan University in June, 2009. He came to the U.S. in August 2010, and started his master's program in the fall 2010. He has been in the electrochemical engineering research group under the direction of Prof. Mark E. Orazem. He received his Master of Science degree in December 2011 and received his Doctor of Philosophy degree in the August 2016 after spending six years being educated in electrochemical engineering.